PhD thesis in joint supervision between:

University of Calabria
Scuola di Dottorato in scienze e tecnologie fisiche, chimiche e dei materiali, Ciclo XXXI

Sorbonne University, Pierre and Marie Curie Campus
École Doctorale Physique en Île-de-France

Ion energization in the terrestrial magnetosphere

SSD: FIS/06, Fisica per il sistema Terra ed il mezzo circumnterrestre

Filomena Catapano

Supervisors:
Prof. Gaetano Zimbardo
Prof. Dominique Delcourt
Dr. Alessandro Retinò

A Sonse, per il suo Amore!

Ad Ester, per la sua grinta!

Summary

Understanding the conversion of magnetic energy into plasma heating accelerated charged particles is a long-standing problem in astrophysics. Spacecraft observations show that energetic ions are found in the terrestrial magnetosphere, with energies ranging from tens of keV to a few hundreds of keV. In this thesis we investigate different ion acceleration mechanisms by using both numerical simulations and spacecraft observations.

Modelling the interaction of electromagnetic perturbations with different ion species in the terrestrial magnetotail, we find that a stochastic acceleration mechanism differently affects the different ion species. In particular, the energy gain increases linearly with the ion charge, while it has a weak dependence on the ion mass.

Using the high-resolution Magnetospheric Multiscale (MMS) observations, we study the ion acceleration at two consecutive plasma jet fronts propagating in the Earth's magnetotail. The front interaction leads to the formation of a magnetic bottle between the jets. Thermal ions are initially trapped in the bottle and as it contracts, due to the different jet front propagation speeds, the second being faster, the ions are accelerated along the parallel direction until they fall in the loss cone. This acceleration mechanism is similar to the model of solar magnetic trap, and we report the first in situ evidence of this mechanism for ions. Also, we investigate the process that produces energetic ions ahead of the first jet front. We observe that the ions are accelerated in this region via a resonant acceleration mechanism which favours the energization of protons and heavy multiply-charged ions. Both of these acceleration mechanisms can have applications to other astrophysical environments where magnetic reconnection is the leading energization mechanism.

Finally, we discuss the ion heating driven by turbulence due to Kelvin-Helmholtz instability observed by MMS at the Earth's magnetopause boundary layer. Using a proxy for the local energy transfer evaluated near the transition scale between fluid and ion kinetic scales, we identify the regions where the ion velocity distribution has more pronounced non-Maxwellian features.

These results can help for the the interpretation of the observations, and can be useful for future missions as a possible trigger for plasma distributions burst mode.

Riassunto

Riuscire a comprendere come l'energia magnetica venga convertita in plasma riscaldato e particelle accelerate è un problema ancora aperto in astrofisica. Le osservazioni spaziali mostrano la presenza di ioni energetici nella magnetosfera terrestre, con energie che vanno dalle decine a qualche centinaia di keV. In questa tesi, mediante l'utilizzo di simulazioni numeriche ed osservazioni in situ, sono studiati diversi meccanismi di accelerazione degli ioni.

Simulando l'interazione di perturbazioni elettromagnetiche con diverse specie ioniche nella coda magnetica terrestre, scopriamo che questo tipo di accelerazione alla Fermi agisce in maniera diversa sulle specie ioniche. In particolare, il guadagno di energia cresce linearmente con lo stato di carica dello ione, mentre ha una dipendenza debole dalla massa.

Utilizzando le osservazioni ad alta risoluzione temporale della missione Magnetospheric Multiscale (MMS), studiamo come gli ioni sono accelerati durante il passaggio di due getti di plasma consecutivi nella coda magnetica terrestre. L'interazione tra i getti genera la formazione di una bottiglia magnetica nella regione tra i due. Gli ioni termici sono inizialmente intrappolati nella bottiglia e come questa si contrae, a causa della diversa velocità di propagazione dei getti, essendo il secondo più veloce, gli ioni sono accelerati lungo la direzione parallela finchè non cadono nel cono di perdita. Questo meccanismo di accelerazione è simile a quello del modello teorico delle trappole magnetiche solari, e qui ne riportiamo la prima evidenza sperimentale per gli ioni. Inoltre, studiamo il meccanismo che energizza gli ioni nella regione di fronte al getto. Gli ioni sono accelerati in questa regione tramite un meccanismo risonante che energizza preferenzialmente i protoni e gli ioni pesanti con stato di carica multiplo. Entrambi i meccanismi di accelerazione possono essere comuni ad altri ambienti astrofisici, dove la riconnessione magnetica è il meccanismo di accelerazione dominante.

Infine, discutiamo il riscaldamento degli ioni dovuto alla turbolenza nella instabilità Kelvin-Helmholtz osservata da MMS nello strato limite della magnetopausa terrestre. Utilizzando un proxy per il trasferimento locale del flusso di energia, valutato vicino la scala di transizione tra quella fluida e

quella cinetica degli ioni, identifichiamo regioni dove le distribuzioni delle velocità degli ioni hanno caratteristiche non-Maxwelliane. Questi risultati sono utili per l'interpretazione delle osservazioni spaziali, e per le missioni future per iniziare lo studio delle funzioni di distribuzione ad alta risoluzione.

Résumé

La compréhension des mechanisms de conversion d'énergie magnétique en energie des particules chargées accélérées est un problème de longue date en astrophysique. Les observations satellites montrent que des ions énergétiques se trouvent dans la magnétosphère terrestre, avec des énergies allant de quelques dizaines de keV à quelques centaines de keV. Dans cette thèse, nous étudions différents mécanismes d'accélération des ions en utilisant à la fois des simulations numériques et des observations satellite.

En modélisant l'interaction entre perturbations électromagnétiques et différentes espèces d'ions dans la queue de la magnétosphère terrestre , nous montrons qu'un mécanisme d'accélération stochastique affecte différemment les différentes espèces d'ions. En particulier, le gain en énergie augmente de manière linéaire avec la charge des ions, alors qu'il dépend peu de la masse.

En utilisant les observations à haute résolution de la mission Magnestospheric Multiscale (MMS), nous étudions l'accélération des ions entre deux fronts de jet de plasma consécutifs se propageant dans la queue de la magnétosphère terrestre. L'interaction entre les jets conduit à la formation d'une bouteille magnétique entre les jets. Les ions thermiques sont initialement piégés dans la bouteille. Lors de la contraction de la bouteille, qui se produit en raison des différentes vitesses de propagation du front du jet (le deuxième jet étant plus rapide), les ions sont accélérés dans la direction parallèle jusqu'à des énergies qui correspondent au cône de perte, a lesquelles les ions sortent de la bouteille. Ce mécanisme d'accélération est similaire au modèle d'accélération dans des piège magnétiques dans la couronne solaire, et nous rapportons la première démonstration de ce mécanisme pour les ions à partir des données satellites in situ. Nous étudions également le processus qui produit des ions énergétiques en amont du premier front de jet. Nous observons que les ions sont accélérés dans cette région a travers d'un mécanisme d'accélération résonant qui favorise l'accélération des protons et des ions lourds avec charges multiples. Ces deux mécanismes d'accélération peuvent avoir des applications dans d'autres environnements astrophysiques où la reconnexion magnétique est le principal mécanisme d'accélération des particules.

Enfin, nous discutons le chauffage des ions provoqué par la turbulence due à l'instabilité de Kelvin-Helmholtz observée par MMS dans la couche limite de la magnétopause terrestre. En utilisant un indicateur pour le transfert d'énergie local calculé aux échelles de transition entre les échelles fluides et les échelles ioniques, nous identifions les régions où la distribution de vitesse des ions montre des caractéristiques non-maxwelliennes le plus marquées. Ces résultats peuvent aider l'interprétation des observations satellite actuelles et peuvent être utiles pour des missions satellite futures en tant que déclencheurs possibles du mode rafale des mesures de fonctions de distribution du plasma.

Contents

Chapter 1

Introduction

This thesis deals with the study of ion heating and ion acceleration mechanisms in the terrestrial magnetotail, by both developing numerical models and analysing in situ spacecraft observations. Particle acceleration occurs throughout the universe, spanning from high-energy particles propagating in the interstellar medium to energetic populations observed in interplanetary space and in the planetary magnetospheres. What these acceleration mechanisms are and where the acceleration takes place are key questions that are being actively investigated.

For example, cosmic rays in the interstellar medium up to about 10^{15} eV, are believed to be accelerated by shock waves at supernova remnants by a Fermi process called diffusive shock acceleration [2].

Also, it is generally assumed that the turbulence in the intra cluster medium of galaxy clusters, accelerates the background electrons up to suprathermal high energies leading to the bremsstrahlung radiation as a source of the observed hard X-ray emission [1].

Concerning the energetic particles of solar origin, it is currently accepted that their occurrence is directly related to either solar flares or to coronal mass ejections [3]. Solar energetic particles have been observed in a wide range of energies between tens of keV and a few GeV; the ultimate energy source of those particles is the magnetic energy of the Sun.

Furthermore, energetic particles are found in planetary magnetospheres in their radiation belts where they are trapped in a strong, basically dipolar magnetic field, bouncing back and forth between the northern and southern hemispheres. Correlated with the high energy and high intensities are radio emissions up to synchrotron radiation when relativistic MeV electrons are present. Energetic particles are also present in the magnetotail regions of planetary magnetospheres, where they bounce and drift around the planet. Reconnection in the magnetotail, wave-particle interactions, and betatron

effects due to radial inward diffusions are prime candidates as processes to accelerate those particles from keV to MeV energies [4].

Planetary magnetospheres are excellent laboratories of space plasma physics, since they are filled with a myriad of plasma physical phenomena which control the momentum and energy transfer in these systems. In the past decades numerous missions have been devoted to the exploration of the terrestrial magnetotail, giving the chance to study the plasma dynamics by in situ measurements and to test the developed theoretical models.

In this thesis a few of the possible ion acceleration and ion heating mechanisms in the terrestrial magnetosphere are studied.

The Chapter 2 is devoted to a general description of the Earth's magnetosphere and to an introduction to the main plasma properties. Also, a brief introduction to the mechanisms of particle acceleration, and observations of energetic protons and heavier ions are reported.

The numerical model, developed for the study of the ion acceleration due to the particle interaction with time-dependent electromagnetic perturbations in the Earth's magnetotail, is described in Chapter 3. The model aims to simulate a Fermi-like acceleration mechanism, which is common to plenty of astrophysical environments and magnetospheres. In Chapter 4 the numerical results are reported showing the dependence of the model on the different free parameters, the single-particle ion dynamics and the statistical behaviour. In particular, we study the acceleration of protons and heavy ions with different charge state in order to understand how the acceleration mechanism effects the different ion species. We find that the ion mass and charge play a fundamental role on the ion acceleration. More in detail, we observe that the ion energy gain has a linear dependence on the ion charge, while it is weakly influence by the ion mass. Therefore, in agreement with recent spacecraft observations, we observe that multiply-charged heavy ions reach higher energies.

The Chapter 5 is dedicated to the description of the recent Magnetospheric Multiscale (MMS) mission. This mission is composed by four spacecraft exploring the terrestrial megnetosphere in a tetrahedral configuration. Due to the very high-resolution plasma measurements, the MMS mission gives the chance to study for the first time the plasma dynamics and acceleration with very high temporal cadence. This Chapter also contains a phenomenological description of the magnetic reconnection process, which is ubiquitous in many astrophysical environments and is the main source of particle acceleration in the terrestrial magnetosphere.

In Chapter 6 are reported the MMS observations of two consecutive plasma jet fronts propagating in the terrestrial megnetotail. These observations suggest the formation of a magnetic bottle between the jets. Since

the second jet is faster, the bottle contracts, and energetic ions are observed in correspondence with the region between the jets. This is the first direct evidence of an acceleration mechanism theoretically described, for example, by the model of the solar magnetic trap. Also, energetic ions are observed in the region ahead of the first jet. Accordingly with theoretical models, we suggest that these ions are trapped in the region ahead of the jet front and are accelerated by a resonant mechanism. Also, by using ion measurements which discriminate the ion composition, we observe how the mechanism accelerate heavier ions as helium and oxygen. Again, this is the first experimental evidence of protons and heavier ions being accelerated by this kind of resonant mechanism in the region ahead of a plasma jet front.

An introduction to Kelvin-Helmholtz instability, and the description of the main properties of the turbulence, are reported in the Chapter 7.

The cross-scale coupling between fluid turbulence and kinetic processes by using high- resolution plasma measurements recorded by the MMS spacecraft during an extended observation period of Kelvin-Helmoltz vortices at the Earth magnetopause boundary layer, is studied in Chapter 8. In particular, the ion heating and the distortion of the ion velocity distribution functions is studied by using and heuristic proxy that represent the local energy transfer evaluated at a scale near the transition between the fluid and the ion kinetic scales. Such a proxy, despite the many approximations, is able to successfully localize regions of ion velocity distribution functions with more pronounced non-Maxwellian features, like beams. These results may be relevant for current and future space plasma missions, for the interpretation of the observations, and as a possible trigger for plasma measurements in burst mode and telemetry.

The main conclusions and discussions are given in the respective Chapters where results are presented. A summary of the main conclusions and finally remarks is reported in Chapter 9.

Chapter 2

General characteristics of magnetospheric plasma

2.1 Earth's magnetosphere and space plasmas

2.1.1 What is a plasma

The word "plasma" was used in physics for the first time by Irving Langmuir to indicate a completely ionized gas. Gas in the plasma state, also known as the fourth state of the matter, composes more then the 80% of the visible matter in the universe; for example the Sun and all the stars, the interstellar, interplanetary and intergalactic medium, and the planetary magnetopsheres are made of plasma. The science of plasma physics was developed to provide an understanding of these naturally occurring plasmas, but also for the quest of the controlled nuclear fusion. In a plasma, charge separation between ions and electrons gives rise to electric fields, and charged particle flows give rise to currents and magnetic fields. Plasma particles and the electromagnetic fields created by them interact in a non linear way, and therefore, plasma dynamics is rather complex; this dynamics can be described using sets of equations at different approximation levels. At the most detailed level, the evolution of the distribution functions of the different kind of particles are described using the Liouville equation. Using some assumption, the Vlasov equation can be derived and used to describe the dynamics, together with Maxwell's equations. This set of equations gives rise to the kinetic theory. However, it is also possible to look at the plasma as a non neutral fluid, when the scales are large enough to consider the dynamics of each particle as a whole. In this case the fluid theory is used. There are several parameters,

common to kinetic and fluid theory, used to characterized the plasma:

- The typical particle velocity can be represented by the *thermal speed*

$$v_{th,j} = \sqrt{\frac{k_B T_j}{m_j}}$$

  where k_B is the Boltzmann's constant of the gases, T_j and m_j are the particle temperature and mass, and j indicates the species, e for electrons and i for ions.

- The *electron plasma frequency* is the typical frequency of a plasma seen as an oscillator, and its reciprocal gives the typical separation time between charges

$$\omega_{p,e} = \sqrt{\frac{4\pi n_e q^2}{m_e}}$$

  here n_e is the electron density and q is the fundamental charge. The *ion plasma frequency* can also be defined using the ion density, mass, and charge.

- The *Debye length* is the typical shielding length of the charges.

$$\lambda_D = \frac{v_{th,e}}{\omega_{p,e}} = \sqrt{\frac{k_B T_e}{4\pi n_e q^2}}$$

  It represents the balance between thermal and electrostatic effects, so that, for scales larger than λ_D the plasma can be considered electrically neutral.

- The *cyclotron frequency*, for electrons and ions, is defined if an external magnetic field B is present. It represents the typical frequency at which particles turn around the magnetic field lines.

$$\Omega_j = \frac{qB}{cm_j}$$

  where c is the speed of light.

- The ratio between kinetic and magnetic pressure is the β parameter

$$\beta = \frac{nk_B T}{B^2/8\pi}$$

  which is useful to describe the state of magnetization of the plasma.

All these quantities can be used to characterize the plasma, to understand in which region of the parameter space plasma is found, and to make approximations in order to simplify the equations in different regimes.

2.1.2 The Vlasov-Maxwell equation system

The kinetic theory is one of the main tools to study a plasma, therefore, in this section the equation system that describe the plasma in this approximation will be discussed. The kinetic framework can be considered as a statistical theory of plasma based on the mean motions of particles. The distribution function f_j for the j species is defined as the probability density of particles in phase space:

$$f_j(\boldsymbol{r}, \boldsymbol{v}, t) = \frac{dN_j}{d^3r d^3v} \ , \tag{2.1}$$

were $\mathbf{r}$ and $\mathbf{v}$ are the particle position and speed at the time t. The normalization of f_j is the following: $\int d^3r d^3v \ f_j = N_j$, where N_j is the total number of particles of the j species. The distribution function represents a probability density that the particle has the position $\boldsymbol{r}$ and the velocity $\boldsymbol{v}$ at the time t. In absence of collision between particles, the general evolution for f_j is the Vlasov equation:

$$\left\{ \frac{\partial}{\partial t} + \boldsymbol{v} \cdot \frac{\partial}{\partial \boldsymbol{r}} + \frac{q_j}{m_j} \left[\boldsymbol{E}\left(\boldsymbol{r}, t\right) + \frac{\boldsymbol{v}}{c} \times \boldsymbol{B}\left(\boldsymbol{r}, t\right) \right] \cdot \frac{\partial}{\partial \boldsymbol{v}} \right\} f_j(\boldsymbol{r}, \boldsymbol{v}, t) = 0 \ , \tag{2.2}$$

where the electric $\mathbf{E}$ and magnetic $\mathbf{B}$ fields include in general external and internal self-consistent fields. The Vlasov equation is a differential equation describing time evolution of the distribution function of plasma consisting of charged particles with long-range interaction, e.g. Coulomb, and it is based on the Boltzmann equation. To complete the description of the plasma dynamic it is necessary to consider Maxwell's equations:

$$\begin{aligned} \boldsymbol{\nabla} \cdot \boldsymbol{E}(\boldsymbol{r}, t) &= 4\pi \rho_c(\boldsymbol{r}, t) \\ \boldsymbol{\nabla} \cdot \boldsymbol{B}(\boldsymbol{r}, t) &= 0 \\ \boldsymbol{\nabla} \times \boldsymbol{E}(\boldsymbol{r}, t) &= -\frac{1}{c} \frac{\partial \boldsymbol{B}}{\partial t}(\boldsymbol{r}, t) \\ \boldsymbol{\nabla} \times \boldsymbol{B}(\boldsymbol{r}, t) &= \frac{1}{c} \frac{\partial \boldsymbol{E}}{\partial t}(\boldsymbol{r}, t) - \frac{4\pi}{c} \boldsymbol{J}(\boldsymbol{r}, t) \ , \end{aligned} \tag{2.3}$$

being ρ_c the charge density and $\boldsymbol{J}$ the current density; these quantities are related to the properties of the medium. The equation 2.2 and the equation system 2.3 represent the Vlasov-Maxwell set of equations that describe the dynamic of the collisionless plasma in presence of electric and magnetic fields.

2.1.3 The Earth's magnetosphere

One of the most used laboratory for the study of natural plasmas is the magnetosphere around our planet. Qualitatively, a planetary magnetosphere is

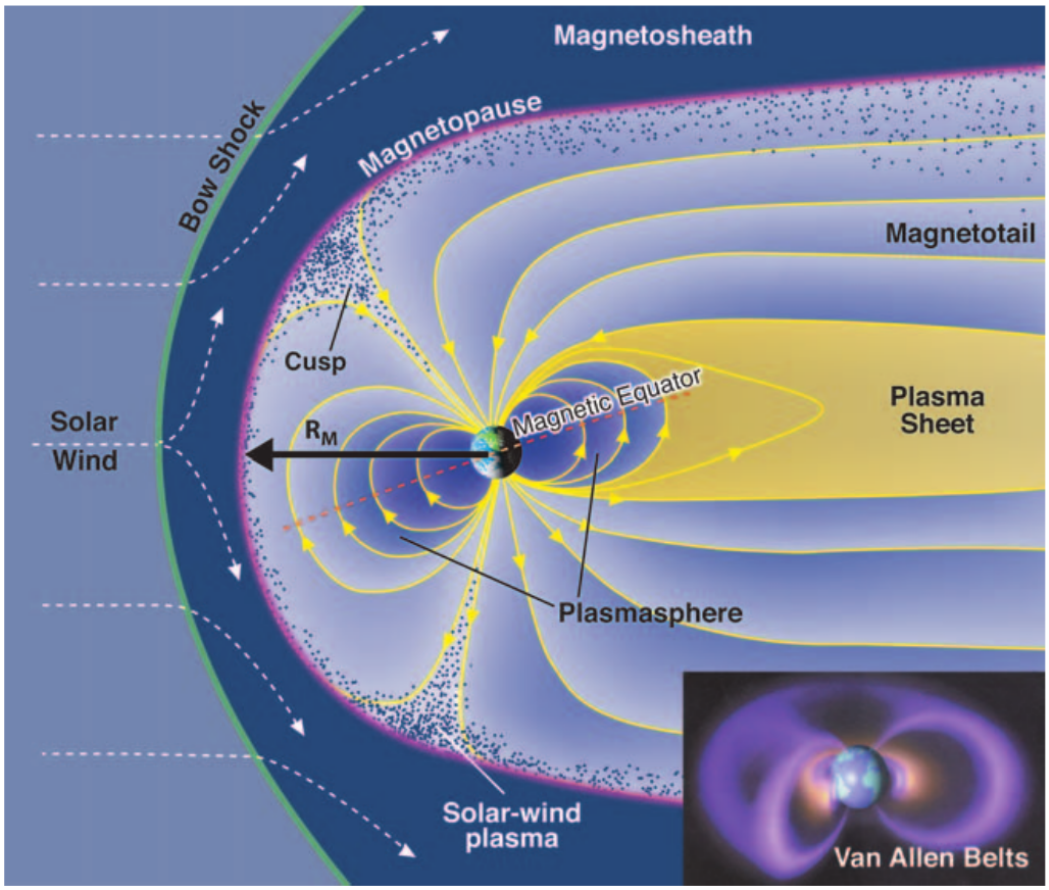

Figure 2.1: Schematic view of the Earth's magnetosphere. See text for a description. *Credit: Steve Bartlett; Inset: Don Davis.*

the volume of space where the planetary magnetic field is separated from the solar wind magnetic field. The solar wind is the plasma that propagates from the surface of the Sun, and within it, the interplanetary magnetic field is embedded. The solar wind propagates with different speed and density depending on the solar activity. Its interaction with the space around the planet can modify the structure of the magnetosphere also thanks to a complex system of induced currents. A schematic view of the terrestrial magnetosphere is given in Figure 2.1. The Earth's magnetic field lines (yellow lines) are shown as modified by the interaction with the solar wind (white lines) arriving from the left. The pressure exerted by the Earth's magnetic field stops the solar wind. The boundary of the magnetospheric cavity is called the magnetopause. Sunward (upstream) of the magnetopause, a standing bow shock slows the incident flow, and the perturbed solar wind plasma between

the bow shock and the magnetopause is called the magnetosheath. Antisunward (downstream) of the Earth, the magnetic field lines stretch out to form the magnetotail. In the northern portion of the magnetotail, field lines point generally sunward, while in the southern portion, the orientation reverses. These regions are referred to as the northern and southern lobes, and they are separated by a sheet of current flowing generally dawn to dusk across the near-equatorial magnetotail in the plasmasheet. Low-energy plasma diffusing up from the ionosphere is found close to Earth in a region called the plasmasphere whose boundary is the plasmapause. The dots show the entry of magnetosheath plasma that originated in the solar wind into the magnetosphere, particularly in the polar cusp regions. The inset is a diagram showing the 3-dimensional structure of the Van Allen belts of energetic particles that are trapped in the magnetic field and drift around the Earth [5]. The Earth's magnetosphere expands for several Earth Radii ($R_E \simeq 6371$ km) behind the Earth. The distance between the nose (the most sunward point) of the magnetopause and the planet is of about $1R_M \simeq 10R_E$, while in the direction of the flanks the distance is of about $20R_E$. Magnetospheres contain considerable amounts of plasma, electrically charged particles in equal proportions of positive charge on ions and negative charge on electrons, from various sources as the solar wind or the ionosphere. Plasmas of different origins can have very different characteristic temperatures. Significant populations of particles at keV–MeV energies, well above the energy of the thermal population, are found in all magnetospheres. How these particles are accelerated is one of the standing problem in plasma physics.

2.2 Mechanisms of particle acceleration

Particle acceleration and transport are fundamental astrophysical processes that occur throughout the universe. A detailed understanding of these phenomena bears on issues ranging from astronaut safety and satellite systems to insights into the most energetic phenomena in our universe. There are many possible mechanisms for particle acceleration in space plasmas. Most of these are common to ions and electrons but the dynamics is different among the two species. Basically, charged particles gain energy when subject to an electric field in their rest frame. Such an electric field $\mathbf{E}$ may be a large-scale externally-imposed field, or a $\mathbf{v} \times \mathbf{B}$ field associated with particles crossing magnetic field lines, or a collective field associated with the environment in which the particle finds itself (e.g., a collisional Coulomb field or a field associated with a level of plasma wave energy). The richness of these various means of creating local electric fields is reflected in the richness of particle

acceleration models in magnetized plasmas.

Here we consider only a few of the acceleration models; for our purposes, it is possible to consider three main physical mechanisms that accelerate the particles : electrostatic acceleration, stochastic processes, and shock acceleration.

2.2.1 Electrostatic acceleration

Electrostatic structures have been observed in many regions of space plasmas, including the solar wind, the magnetosphere, the auroral acceleration region, and in association with shocks, turbulence, and magnetic reconnection. Due to the potentially large amplitude of electric fields within these structures, their effects on particle heating, scattering, and acceleration can be important. One possible theoretical description of some of these structures is the concept of Bernstein-Greene-Kruskal (BGK) modes [6], which are exact nonlinear solutions of the Vlasov-Poisson system of equations in collisionless kinetic theory. These modes generate when a sinusoidal electrostatic wave propagates in a plasma with a phase velocity v_ϕ. This generate a wave potential well that can trap and resonantly accelerate the particles with a velocity close to v_ϕ. Another example, is the bulk ion acceleration by the perpendicular Hall field during the magnetic reconnection. In this case, upstream ions are accelerated at separatrices by the Hall field reaching velocities close to the Alfvén speed and eventually forming the reconnection jets in the downstream outflow region. The Hall electric field is electrostatic and mostly perpendicular to the local magnetic field. Also, it is strongest near the separatrices. Mechanisms of electrostatic acceleration and heating are very common in the universe, and have been extensively studied both numerically and experimentally.

2.2.2 Stochastic acceleration

If the electric fields has characteristic small scale variations, waves, or turbulence, stochastic acceleration may occur [9]. Charged particles moving under the influence of randomly time-varying electromagnetic fields may be expected to experience a net acceleration. In this case, the particles are scattered by the electromagnetic perturbations and diffuse in the inhomogeneous medium. At each interaction with the perturbation the particles can experience loss or gain of energy, but generally, the result is a net acceleration. A general model that describes the stochastic acceleration is the one proposed by Fermi in order to explain the acceleration of cosmic rays [7, 8]. This model is also known as second-order Fermi acceleration model. Then, the

Fermi's model, have been largely used to described different phenomena in astrophysics. The Fermi acceleration mechanism will be described more in detail in the next chapter.

2.2.3 Shock acceleration

The shock acceleration is a kind of stochastic acceleration but restricted to the presence of a shock wave. When a wave moves faster than, for example, the local speed of sound in a fluid, it forms a shock wave. Like an ordinary wave, a shock wave carries energy and can propagate through a medium. However, it is characterized by an abrupt, nearly discontinuous change in pressure, temperature and density of the medium. When a shock wave passes through matter, the energy is conserved but the entropy increases, so that it is a strongly irreversible process. Ambient particles interact with such discontinuity and can be efficiently accelerated. An example of quasi-stationary shock wave is the Earth's bow shock, shown in Figure 2.1. It forms because of the supersonic solar wind encounter the flow of the Earth's magnetic field. In astrophysics the shock waves are really common, and in these regions energetic ions and electrons are always observed. There are different theories to support the observations. One of the most accepted by the scientific community is the Diffusive Shock Acceleration (DSA), introduced by [10, 11]. The DSA is also known as first-order Fermi acceleration. However this theory leavs open questions on how particles gain the lowest energy to undergo the DSA, this is the so called "injection problem". The second theory is the one on the acceleration due to the turbulence formed upstream of the shock front. The acceleration at shock is very efficient for both ions and electrons. However these theories not always can describe well the observations. Recently, the idea of a diffusion of the particles in a superdiffusive regime [12], have made theory closer to some of the observations. However, acceleration at shocks remains one of the most fascinating and promising mechanisms in astrophysics.

2.3 Ion acceleration in the Earth's magnetosphere

Energetic electrons have been largely investigated using both numerical simulations and in-situ observations, e.g., [13, 14, 15]. The study of the ion dynamics and acceleration is more complicated because of their larger mass and different composition. Indeed, when we consider ions in the magnetosphere, we should take into account not only protons, but also heavier ions

in singly and multiply charge states. Therefore, instruments for in-situ observations should be able to discriminate the ion species, while in numerical simulations we should use very high resolutions to resolve the spatial and temporal scales that involve the ion dynamics.

2.3.1 Experimental evidences

Ions with energies from tens to hundreds of keV are often observed in the Earth's magnetotail. Using data from past missions, as for example the multi-satellite Cluster mission [16], or the Time History of Events and Macroscale Interactions (THEMIS) mission [17], it is possible to statistically study the change of the ion spectra and temperature during different periods of the geomagnetic activity and in different regions of the magnetosphere.

The THEMIS measurements from March 23, 2007 to August 31, 2011 are studied and reported in [18] to determine how the ion and electron temperatures and their ratio (T_i/T_e) change spatially in the magnetosheath and plasma sheet and to identify the processes responsible for the variations. Results are shown in Figure 2.2. It was found that in the solar wind (black points) T_i/T_e varies from $\sim$ 0.1 to 2, while in the magnetosheath (green points) it varies from $\sim$ 4 to 12 with higher ratios observed during larger solar wind speed and at locations closer to the magnetopause. T_i/T_e remains almost unchanged as particles flow downstream and cool adiabatically. Across the flank magnetopause from the magnetosheath to a plasma sheet that is cool with abundant cold plasma, temperature and specific entropy for ions and electrons increase significantly while T_i/T_e remains similar, indicating that the magnetosheath ions and electrons are non-adiabatically energized with similar proportion while entering the magnetosphere. Within the tail plasma sheet (blue points), T_i/T_e varies from $\sim$ 6 to $\sim$ 10 when plasma is relatively cool to $\sim$ 2 to $\sim$ 5 when relatively warm. With this correlation, T_i/T_e is higher closer to the flanks and during northward interplanetary magnetic field, while lower T_i/T_e is more often seen during disturbed period around midnight. The distinguishably lower T_i/T_e for warmer plasma in the near-Earth plasma sheet (red points) is likely due to additional non-adiabatic heating of electrons more than ions as particles move earthward and are adiabatically energized. As particles move into the near-Earth magnetosphere, strengthening magnetic drift brings more hotter ions toward dusk and more hotter electrons toward dawn, resulting in a strong T_i/T_e dawn-dusk asymmetry with very high T_i/T_e (from 15 to 100) near dusk and very low T_i/T_e near dawn. These results suggest that many processes can produce such a temperature variations, depending on the magnetosphere regions and local sources.

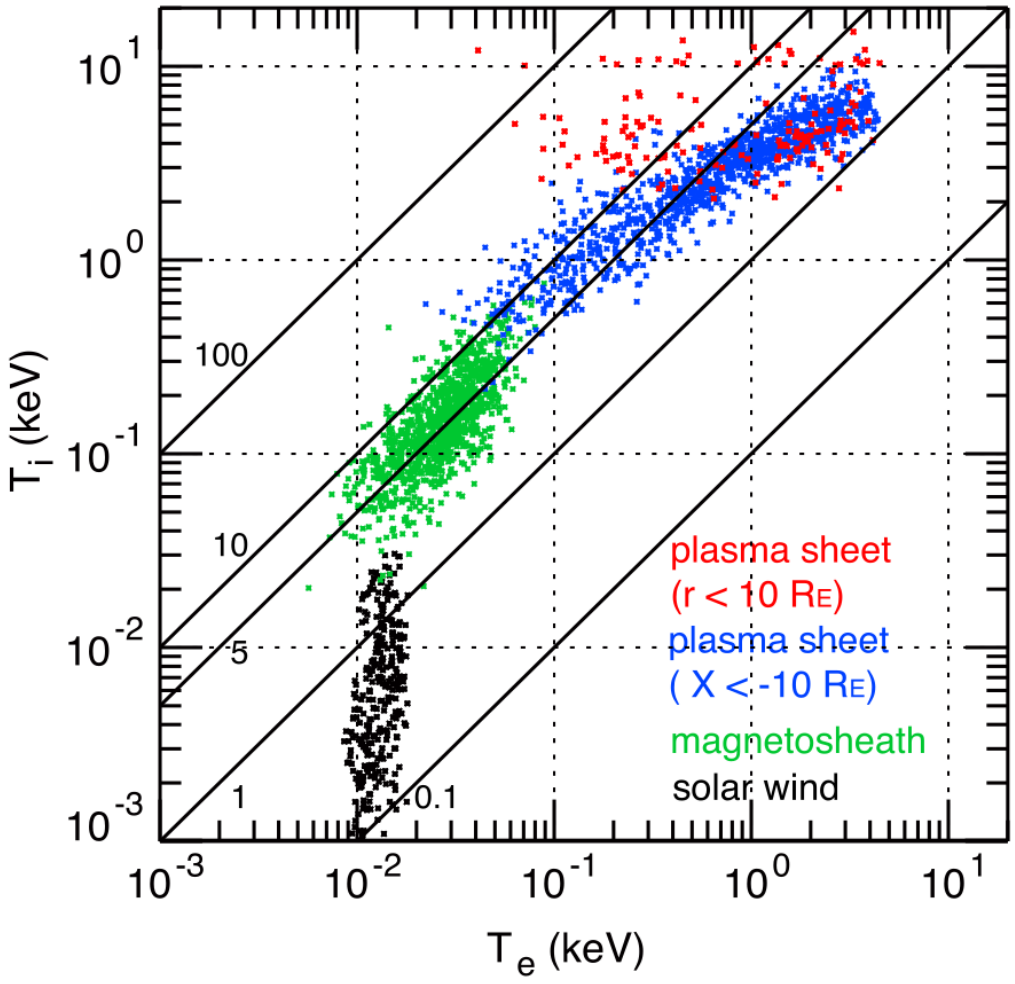

Figure 2.2: Scatter diagram of ion temperature (T_i) versus electron temperature (T_e) in the solar wind, magnetosheath, and plasma sheet. $T_i/T_e = 0.1$, 1, 5, 10, and 100 are indicated by the solid oblique lines. Credit: [18].

Furthermore, in Figure 2.3 it is shown an example of the ion energy spectra during three phases of a geomagnetic storm, reported in [19]. In panel (a) it is shown the Disturbance storm time (Dst) values during 15 July–5 August 2004, when the Cluster spacecraft were exploring the Earth's magnetotail. The Dst index measures the magnetic activity derived from a network of near-equatorial ground-based geomagnetic observatories [20]. The highlighted time intervals in panel (a) indicate periods of observation of the characteristic spectra reported in panel (b), chronologically before, during and after the geomagnetic storm. Spectra in panel (b) are the 15 min average ion flux for each energy channel measured by the CIS (red dots) and RAPID (blue dots) instruments on board on Cluster. The CIS instrument measures ions up to 40 keV, while RAPID cover the energy spectra from 20 to 450 keV. Both the instruments measure the three dimensional (3D) ion distributions with a resolution of 4 s. The solid grey line in panel (b) represents the energy spectra obtained from the theoretical model of the *Kappa distribution* (see [21] for more details), using the index $\kappa = 5$ and E_0 =3 keV, but it is used only to compare the three observed spectra. From the observations it is clear that during period of strong geomagnetic activity (central panel in (b)), the flux of ions with larger energies strongly increases. Therefore, ions are efficiently accelerated during period of geomagnetic disturbances, with a substantial change in their energetic spectra.

During period of strong geomagnetic activity, numerous acceleration mechanism are triggered by instabilities. The most commons are for example the reconfiguration of the magnetic dipole, the increment of the level of electromagnetic fluctuations, and the magnetic reconnection. However, relevant levels of energetic electrons and ions are also observed during periods of low geomagnetic activity [22], leaving open the search for the acceleration mechanism.

2.3.2 The role of heavier ions

The ion composition depends on the geomagnetic activity. Basically, heavy ions with low charge state have ionospheric origin, while heavy ions with high charge state originate from solar wind. However, it is very often observed the injection, energization, and transport of solar wind material in the magnetosphere, especially during period of strong instabilities due to the intensive solar activity. Therefore, it is important to consider the ions in the Earth's magnetosphere not only as protons, but as a mix of light and heavy ions in different charge state.

Recently, using data from the Magnetospheric MultiScale (MMS) mission [23], in particular from the Energetic Ion Spectrometer (EIS) [24] instrument,

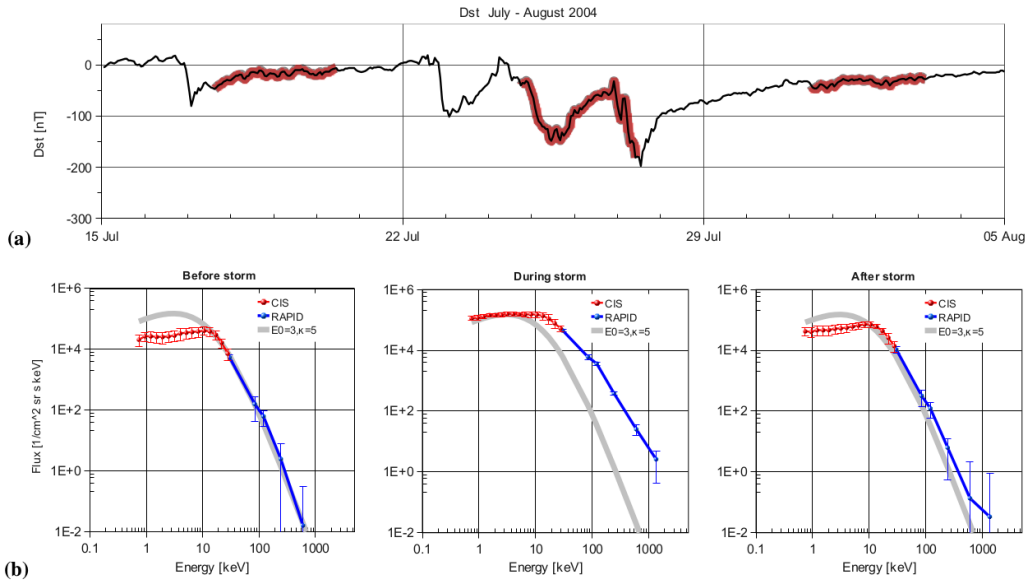

Figure 2.3: Ion energy spectra during three phases of a geomagnetic storm. Panel (a) Dst values during 15 July–5 August 2004. Highlighted time intervals indicate periods used to generate the characteristic spectra in the lower part of the figure. Panel (b) Energy spectra before, during and after the geomagnetic storms on 22–28 July. The dots represent the average proton flux (vertical axes) for each energy channel (horizontal axes) of the RAPID (plotted with blue color) and CIS (red) instrument. To facilitate comparison between the different spectra, is added a model of the κ distribution with κ=5 and E_0 =3 keV (gray, solid line) to all spectra in this row. Credit: [19].

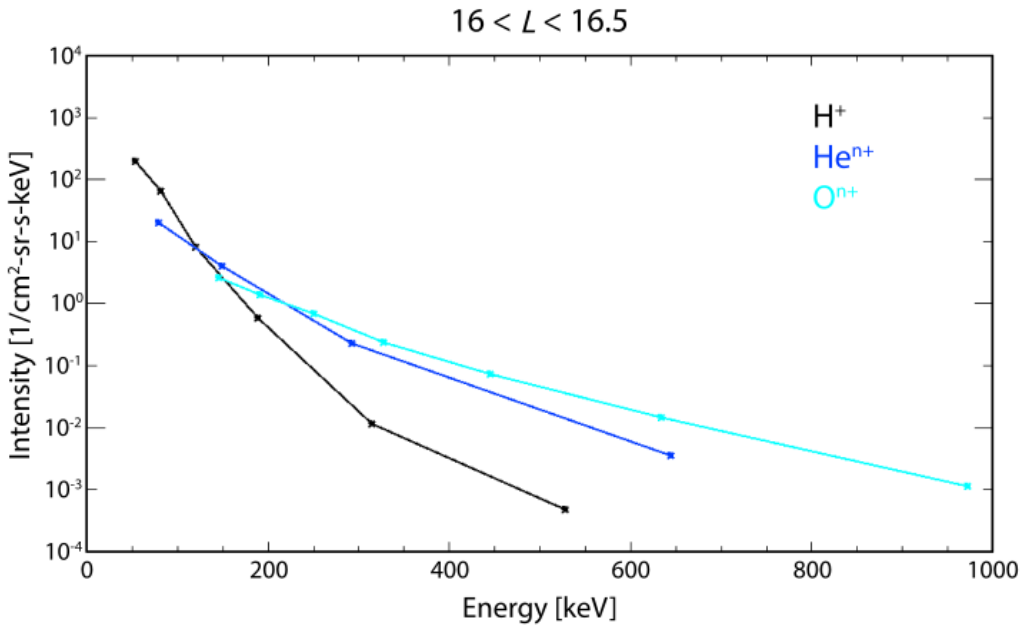

Figure 2.4: Average ion flux as a function of the energy for protons (black line), helium (blue line) and oxygen ions (cyan line) measured by EIS during March-September 2016 in the nightside region, for $16 < L < 16.5$. Credit: [25].

that measures energetic ions from 45 keV up to 1 MeV, it was found a dependence of the ion composition on the energy. Figure 2.4 shows the average ion flux as a function of the energy for protons (black line), helium (blue line) and oxygen ions (cyan line) measured by EIS during March-September 2016 in the nightside region, for $16 < L < 16.5$ where L indicates the L-shell (i.e., the set of magnetic field lines which cross the Earth's magnetic equator at a number of Earth-radii equal to the L-value). It is possible to observe that for lower energies protons dominate, but for energies larger than ~ 200 keV there is a change in the spectra, showing the dominance of heavier ions as the oxygen. This result have been largely discussed in [25] and have been obtained also for the dayside regions, here we report only an example for brevity. Even if the EIS data give not information on the charge state, the result is very important. It suggests that energetic ions, especially for energies larger than 150 keV, are mainly composed by heavy ions and this can reveal the properties of the ion acceleration and dynamics.

In addition, analyzing data from past missions such as Polar or AMPTE (Active Magnetospheric Particle Tracer Explorers), it is possible to study the sources and the ion composition in the magnetosphere through instru-

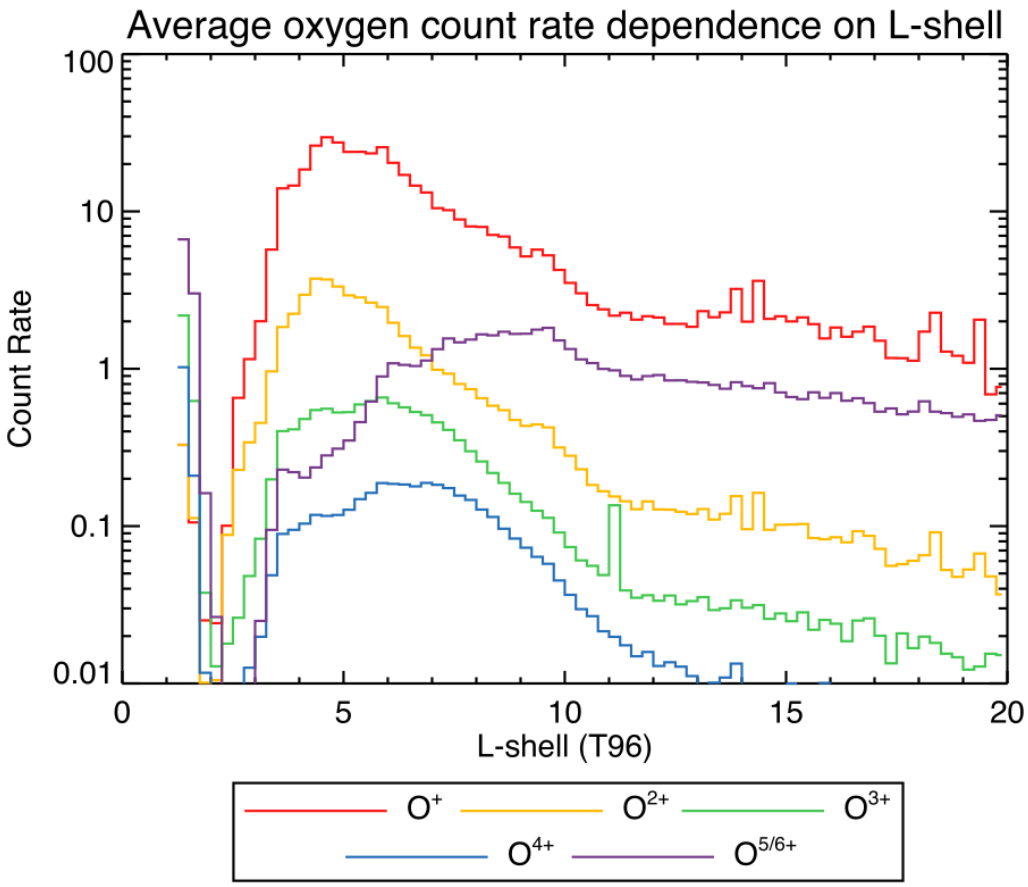

Figure 2.5: Average distributions of oxygen charge states measured by Polar/CAMMICE/MICS from 13 September 1996 to 17 March 2000 and from 12 March 2001 to 26 June 2002, shown as a function of equatorial L shell. Credit: [26].

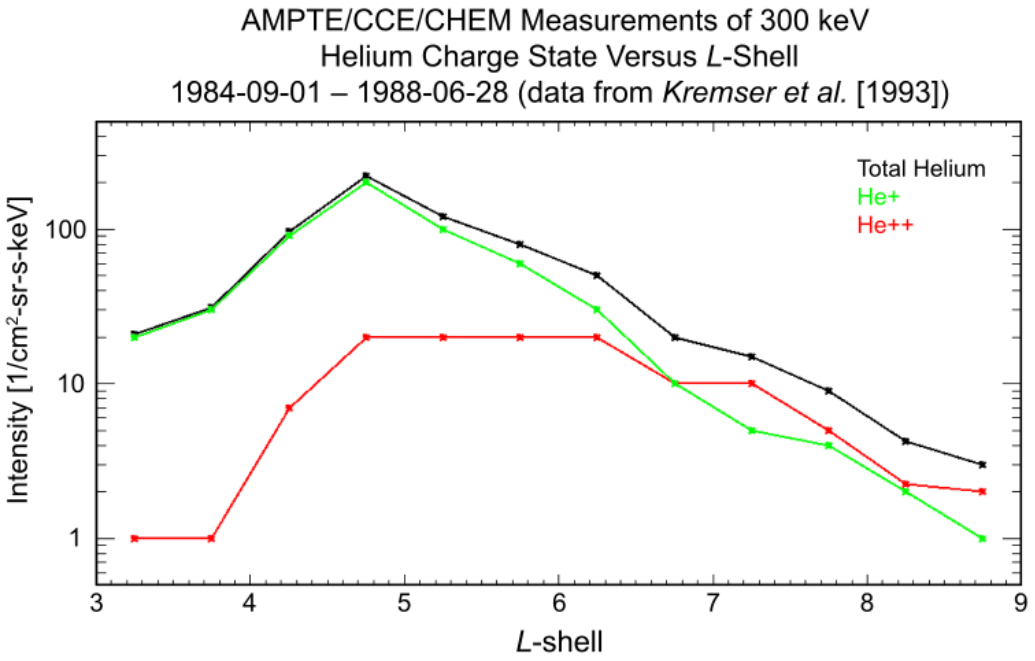

Figure 2.6: AMPTE/CCE/CHEM observations of singly and doubly charged 300 keV helium ion intensities (green and red, respectively) observed from 1 September 1984 to 28 June 1988 are plotted versus L shell, showing that alphas are the primary helium constituent at $L \geq 6.5$. Credit: [25].

ments which measure both ion charge and mass. In Figure 2.5, for example, the distribution of oxygen in different charge state is shown as a function of the L-shell. Data are 15 min averaged from the dataset that goes from 13 September 1996 to 17 March 2000 and 12 March 2001 to 26 June 2002. Measurements are taken from the Magnetospheric Ion Composition Spectrometer (MICS), part of the Charge and Mass Magnetospheric Ion Composition Experiment (CAMMICE), on board on Polar. The measures are in an energy per charge range of 1 to 200 keV/e. From the Figure 2.5 it is possible to notice that for low L-shell singly-charged oxygen ions (red line) dominate, while the count rates of multiply-charged ions are well below. The scenario changes considering L$\geq$ 7. In this regions O^+ is still dominating, but the count rate of $O^{5/6+}$ increases and become only three times lower then O^+, as shown in [26] and [27]. Furthermore, as shown in [25], if we compare the count rate of He^+ and He^{++} we find a similar behaviour. In Fig 2.6, is reported the intensity of He^+ (green line), He^{++} (red line), and the total Helium (black line) as a function of L-shell. These data are measured by the Charge-Energy-Mass (CHEM) spectrometer, part of the Charge Compo-

sition Explorer (CCE) instrument on board on the AMPTE mission, in the range from 1 to 300 keV/q. Again, it is possible to notice that there is a prevalence of doubly-charged helium ions for larger L shells.

In conclusion, the ion composition varies depending on the energy and distance from the Earth. Therefore, it is important to consider all the ion species studying the ion acceleration in the Earth's magnetosphere. Several questions on the acceleration mechanism of protons and heavier ions are still open and deserve more attention, while observations in the terrestrial magnetosphere of such ion species are very scarce.

Chapter 3

Numerical Model

Int this chapter are discussed results from test particle simulations of protons and heavy ions interacting with time-dependent three-dimensional (3D) electromagnetic perturbations in the Earth's magnetotail. The particles are injected in a configuration of fields obtained by [28] as solutions of a generalized Harris model. The particles interact with the perturbations being scattered many times, at each interaction they can gain or lose energy undergoing a second-order Fermi-like acceleration mechanism. Before giving the details of the numerical set-up and results, we describe the acceleration mechanism that we propose to simulate.

3.1 The second-order Fermi acceleration

It is quite frequent to find an inverse power law for the energy spectrum of the protons in space plasma or other ions. The question on how this spectra is generated have been largely discussed, in particular concerning the spectra of cosmic rays. The Fermi mechanism was first proposed in 1949 as a stochastic means by which particles colliding with clouds in the interstellar medium could be accelerated to high energies. In Fermi's original picture, charged particles are reflected from "magnetic mirrors" associated with irregularities in the Galactic magnetic field. The mirrors are assumed to move randomly with typical velocity V and Fermi showed that the particles gain energy stochastically in these reflections. If the particles remain within the acceleration region for some characteristic time τ_{esc}, a power-law distribution of particle energies is obtained. Following [32], we carry out a relativistic analysis of the change in energy of the particle in a single collision. The mirror is taken to be infinitely massive and so its velocity is unchanged in the collision. The centre of momentum frame of reference is therefore that

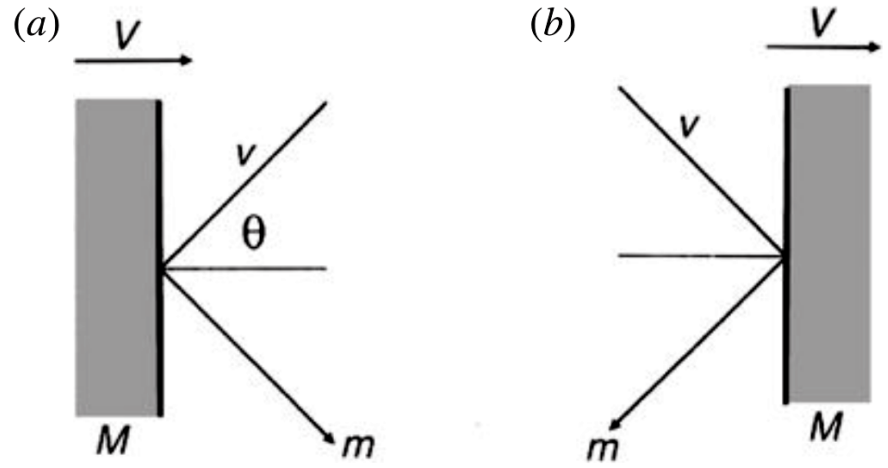

Figure 3.1: Illustrating the collision between a particle of mass m and a cloud of mass M: (a) a head-on collision; (b) an overtaking collision.

of the cloud moving at velocity V. The energy of the particle in this frame is

$$E' = \gamma \left(E + Vp\cos(\theta) \right), \tag{3.1}$$

where γ is the Lorentz factor, E is the particle energy in the observer's frame, p is the particle momentum, and θ is the angle between the initial direction of the particle and the normal to the surface of the mirror. The x-component of the relativistic three-momentum in the centre of momentum frame is

$$p'_x = p'\cos(\theta') = \gamma \left(p\cos(\theta) + \frac{VE}{c^2} \right) \tag{3.2}$$

where c is the speed of light. In the collision, the particle's energy in the cloud frame is conserved, $E'_{before} = E'_{after}$, and its momentum in the x-direction is reversed, $p'_x \rightarrow -p'_x$. Therefore, transforming back to the observer's frame,

$$E'' = \gamma \left(E' + Vp'_x \right). \tag{3.3}$$

Substituting E' and p'_x using the equations 3.1 and 3.2 respectively, and expanding the equation 3.3 to second order in V/c, we find

$$\Delta E = E'' - E = E \left[\frac{2Vv\cos(\theta)}{c^2} + \frac{3}{2}\left(\frac{V}{c}\right)^2 \right]. \tag{3.4}$$

where v is the particle speed.

Particles can basically perform two type of collisions depending on the relative velocities of approach of the particle and the cloud. As shown in

Figure 3.1, if the particle and the cloud propagate in opposite direction they perform an head-on collision (see panel (a)) and particles can gain energy. While, if clouds and particles move in the same direction, they perform an overtaking collision (see panel (b)) where particles can lose energy. The probabilities of head-on and overtaking collisions are proportional to $v + V\cos(\theta)$ and $v - V\cos(\theta)$ respectively, and with $0 < \theta < \pi$. The probability of the angle lying in the angular range θ to $\theta + d\theta$ is proportional to $\sin(\theta)d\theta$, and averaging over all angles in the range $[0; \pi]$, it is possible to obtain the average energy gain per collision

$$\left\langle \frac{\Delta E}{E} \right\rangle = \frac{8}{3}\left(\frac{V}{c}\right)^2. \tag{3.5}$$

This illustrates the famous result derived by Fermi that the average increase in energy is only second-order in V/c. This result leads to an exponential increase in the energy of the particle since the same fractional increase occurs per collision. If the mean free path between clouds along a field line is L, the time between collisions is $L/(c\cos(\phi))$ where ϕ is the pitch angle of the particle with respect to the magnetic field direction. Averaging $\cos(\phi)$ over the pitch angle ϕ, the average time between collisions is $2L/c$. Therefore, the average rate of energy increase is

$$\frac{dE}{dt} = \left(\frac{4}{3}\frac{V^2}{cL}\right)E = \alpha E. \tag{3.6}$$

The particle is assumed to remain within the accelerating region for a time τ_{esc}. The standard one-dimensional equation for the particle distribution function is [33]

$$\frac{dN}{dt} = D\nabla^2 N + \frac{\partial}{\partial E}\left[b(E)N(E)\right] - \frac{N}{\tau_{esc}} + Q(E) \tag{3.7}$$

where $N(E)$ is the number of particle with energy E, D is the diffusion coefficient, $b(E)$ is the energy loss term, and $Q(E)$ is the term representing the sources. We are interested in the steady-state solution in the absence of diffusion and so $dN/dt = 0$, and $v = 0$. It is also assumed that there are no sources, $Q(E) = 0$. The energy loss term $b(E) = -dE/dt$ now becomes an energy gain term, $b(E) = -\alpha E$. Therefore, we reduce to

$$-\frac{d}{dE}[\alpha E N(E)] - \frac{N(E)}{\tau_{esc}} = 0. \tag{3.8}$$

Differentiating and rearranging this equation we obtain

$$N(E) = constant \times E^{-x} \;\; ; \;\; where \;\; x = 1 + \frac{1}{\alpha\tau_{esc}}. \tag{3.9}$$

The last equation shows that the Fermi acceleration mechanism results in a power-law energy spectrum.

3.2 Numerical set-up

We propose to reproduce the acceleration of ions in the Earth's magnetotail current sheet. This environment is well described by the Harris model [29], which is an exact solution of the Vlasov equation in stationary conditions. For our analysis we will use a class of solutions obtained by [28] from a generalized Harris model that better describes the observations. In order to represent the level of fluctuations frequently observed in the magnetotail, we overimpose to the current sheet configuration the time dependent electromagnetic fluctuations obtained by [34]. In the following the numerical model will be described more in detail.

3.2.1 Current sheet model

The model developed by [28] allows to regulate the level of plasma temperature and density inhomogeneities across the sheet. This model generalizes the classical Harris model via including two-temperature current-carrying plasma populations and one background plasma population not contributing to the current density. We use the notation $f_j\left(v_j, T_j\right)$ to describe a Maxwellian distribution function with the corresponding drift velocity v_j and temperature T_j, j indicates the species ($j = i$ for ions and $j = e$ for electrons). Any linear combination of f_j is solution of the stationary Vlasov equation. In the velocity plane the Maxwellian distribution function can be presented as a peak of phase space density with contour lines represented by concentric circles, centered in the origin. The shifted Maxwellian has the same shape in the velocity plane, but the center is shifted from the coordinate origin to a distance equal to the drift velocity. The spacecraft observations show that the phase space density of the particles velocity distribution in thin current sheets is often represented by a ring distribution (see [35]). Figure 3.2 shows observations from different missions in the magnetosphere of ion distribution functions. In particular examples of (a) Maxwellian distribution, (b) shifted Maxwellian distribution, and (c) ring type distribution.

In our model we focus on the ring type distribution function. The simplest way to construct such distribution consists in using a combination of two Maxwellian distribution with different temperatures. Therefore, to develop our model, we use the following distribution function:

$$F_j = f_{ring} + \delta f_j(0, T_{0j}) \tag{3.10}$$

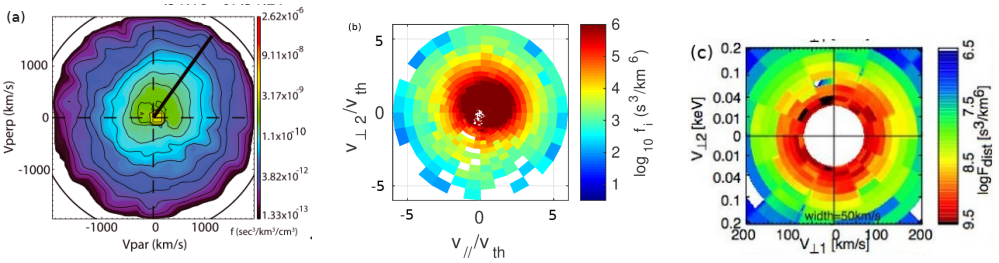

Figure 3.2: Example of ion distribution funcions observed by different missions in the Earth's magnetosphere: (a) Maxwellian distribution, (b) shiffted Maxwellian distribution, (c) ring type distribution. Credit: (a) [31], (b) [30], (c) from the same event discussed in Chapter 8.

where the parameter f_{ring} represents the ring distribution, so that F_j represents a linear combination of ring distributions and background plasma. The ring distribution is obtained by the combination of two shifted Maxwellian with different temperatures, $f_{ring} = f_j(v_{1j}, T_{1j}) - \gamma f_j(v_{2j}, T_{2j})$ where the parameter γ describes the relative density of the second current-carrier population. $f_j(0, T_{0j})$ represents the background plasma with zero bulk velocity. The parameter δ represents the relative density of the background population and its value is chosen to have a positive phase space density everywhere in the phase space. For $\gamma = 0$ we obtain the distribution function presented in [36]. We consider the coordinate system with the x-axis directed along Sun-Earth direction, the z-axis is oriented across the CS (i.e., along the direction of the CS inhomogeneity), and the y-axis is directed along the electric current flow. Thus, in this model the magnetic field has one component $B_x(z)$ corresponding to the vector potential $A_y(z)$, while the electric field has only the component $E_z(z)$ corresponding to the scalar potential $\phi(z)$. The Maxwell equations reduce to equations for the scalar potential ϕ and vector potential A_y as in the classic Harris equilibrium. Using the quasi neutrality condition (e.g., $\partial^2\phi/\partial z^2 \cong 0$) we obtain the following equation for the dimensionless vector potential ($a = A_y q_i v_{1i}/cT_{1i}$, where q_i is the ion charge and c is the speed of light and where the Boltzmann constant is set to 1 for semplicity)

$$\frac{\partial^2 a}{\partial z^2} = -e^{a-\Phi} + \gamma t_i e^{a-\Phi/t_i} - \alpha t_e e^{a\alpha+\Phi/t_e}(1-\gamma) \tag{3.11}$$

and the dimensionless scalar potential ($\Phi = \phi q_i/T_{1i}$)

$$\frac{\partial \Phi}{\partial z} = -\frac{\partial a}{\partial z}\frac{\partial G/\partial a}{\partial G/\partial \Phi} \tag{3.12}$$

where the function G, obtained from the quasi neutrality condition, is [28]

$$G(a,\Phi) = e^{a-\Phi} + \gamma e^{a-\Phi/t_i} + \delta e^{-\Phi/t_b} - e^{\alpha a+\Phi/t_e}(1-\gamma) - \delta e^{\Phi/t_b} = 0. \quad (3.13)$$

Above, t_e, t_i, t_b are the normalized temperatures with respect to T_{1i}, of electrons and ions of first, second and background populations. The most important parameter is $\alpha = -v_{1e}T_{1i}/v_{1i}T_{1e}$ where we assume that $T_{1e} = T_{2e} = T_e$, $T_{0e} = T_{0i}$, $v_{1e} = v_{2e}$, $v_{1i}/T_{1i} = v_{2i}/T_{2i}$. We notice that most frequently in the magnetotail $T_i \sim 5T_e$ (e.g., [37, 38]), and this condition has an influence on the current carrying populations. Here, the condition $T_{0e} = T_{0i}$ can be used because the background populations do not contribute to the current density. Usually, electrons are colder than ions and we use this condition for the first and second populations that are carrying the current. For $\alpha = 1$ we obtain the class of solution proposed by Harris with the null scalar potential. We have investigated different classes of solutions varying the parameters δ, γ, α and t_b to describe the temperature inhomogeneity in the CS. At variance with Harris solutions, an analytical solution for the vector potential is not possible in general, so that we need to carry out a simple numerical integration along z of the equations (3.11)–(3.13) to obtain the various quantities [28]. Several populations of ions and distribution of scalar potential $\phi(z)$ result in realistic distribution of plasma parameters across the magnetotail. To illustrate the usefulness of the our CS model, we show the comparison of modelled and observed distributions of ion temperature. We picked up from the Cluster database four crossings with distinguished variations of the ion temperature across the sheet (see Figure 5 in [39]). In Figure 3.3 (adapted from [28]) we report the comparison of $T_{i,eff}$ as function of B_x spacecraft observations showing the model capability of describing different configurations. The ratio of pressure and density gives the effective ion temperature $T_{i,eff}$. Indeed, one of the basic features of Harris solution is that the temperature is constant across the CS thickness. Changing the parameters we obtain different profiles of the magnetic field $B_x(z)$ and electric field $E_z(z)$.

In the following we use the two self-consistent solutions that better describe observations, as it is shown in Figure 3.3. In particular, we focus on profiles (c) and (d) of Figure 3.3, and the corresponding magnetic and electric field profiles are shown in Figure 3.4. These two solutions are those which have the lowest and the highest slope, respectively, in the magnetic field profile among solutions in Figure 3.3. In Figure 3.4 the black line represents the Harris solution with the null electric field, the red line represents the magnetic field profile that has the lowest slope, or slower variation of the magnetic field across the CS, and the blue line represents the profile with the

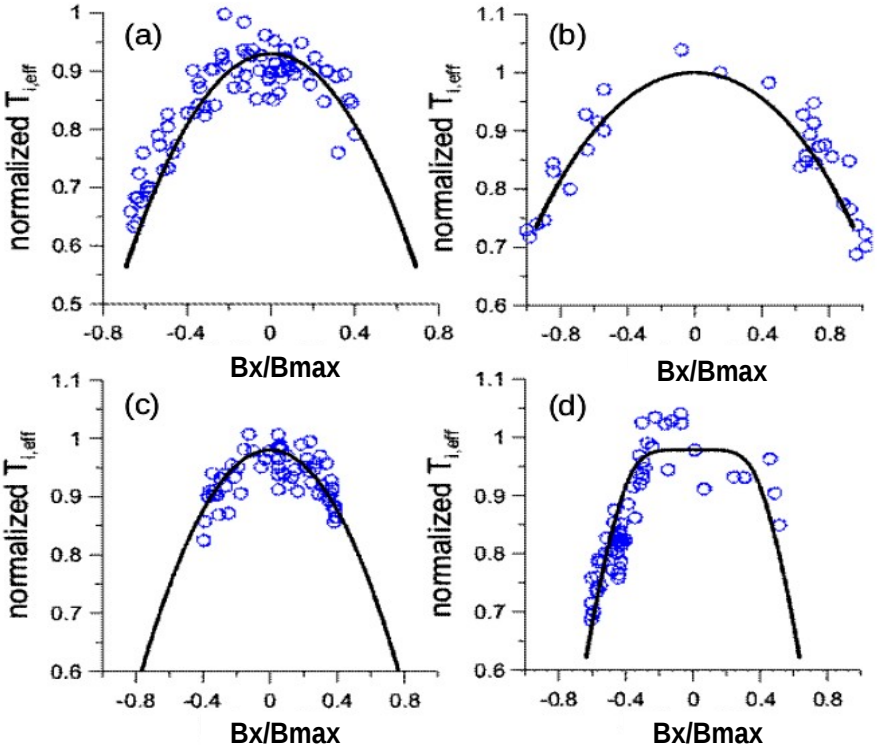

Figure 3.3: Comparison of four profiles of ion temperature measured in the magnetotail CSs (shown by blue circles) with model profiles (shown by black curves). See [28] for details.

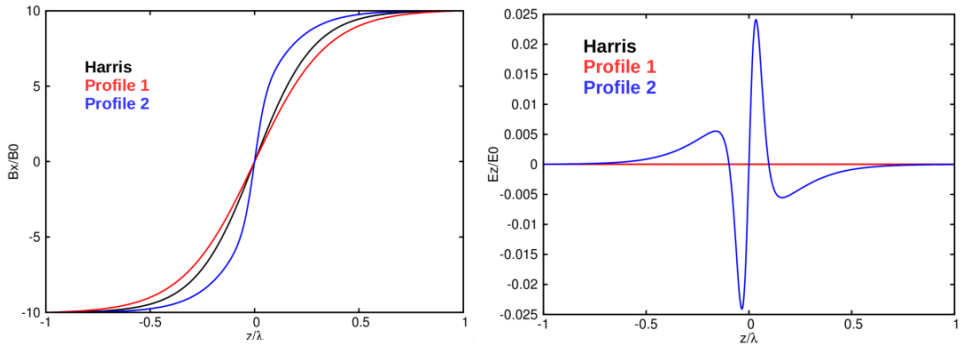

Figure 3.4: Model profiles of $B_x(z)$ and $E_z(z)$, the black line represents the Harris solution, while the red line represents the solution with lower slope in B_x, and the blue line the profile with higher slope.

solutions	δ	γ	α	t_b
Harris	3	1	1	1/3
profile 1	1	1	0	1/3
profile 2	3	0.4	10	1/7

Table 3.1: Parameters used to obtain the profiles in Figure 3.4

highest slope. The parameters used to obtain the profiles in Figure 3.4 are shown in Table 3.1.

3.2.2 Electromagnetic perturbations

In the test particle numerical simulation, we overimpose time dependent electromagnetic fluctuations [34], which represent fluctuations frequently observed in the magnetotail even in quiet periods [41], to the self-consistent solutions shown in Figure 3.4. We use a three-dimensional simulation box with $L_x = L_y = 10^5$ km and a size along the z direction that ranges from $-L_z$ to L_z, where $L_z = 2.5 \times 10^4$ km. This has to be considered as a local simulation box, indeed its size of about $15R_E$ is only a fraction of the actual magnetotail extension, so that large scale variations in the magnetotail are neglected. The characteristic thickness of the CS is set to $\lambda = L_z/5 = 5 \times 10^3$ km. We use the coordinate system as in [28]. A number N_f of time dependent electromagnetic fluctuations are located in the (x, y) plane; such perturbations perform an oscillating motion in the plane. Thus, the total magnetic field is given by

$$\mathbf{B}(\mathbf{r}, t) = B_x(z)\mathbf{e}_x + B_n\mathbf{e}_z + \delta\mathbf{B}(\mathbf{r}, t) \tag{3.14}$$

where the first term is the magnetic field from self-consistent numerical solutions of equation (3.11) (shown in Figure 3.4), the second term is the out of plane magnetic field, B_n, which simulates a remaining part of the Earth dipole magnetic field. The third term represents the time dependent fluctuations, $\delta\mathbf{B}(\mathbf{r},t) = \nabla\times\mathbf{A}(\mathbf{r},t)$. The vector potential perturbations are modeled as [34]

$$\begin{aligned} A_x(\mathbf{r},t) &= A_0\Sigma_i \exp[-|\mathbf{r}-\mathbf{r}_i(t)|/\ell] \\ A_y(\mathbf{r},t) &= A_0\Sigma_i(-1)^i \exp[-|\mathbf{r}-\mathbf{r}_i(t)|/\ell] \\ A_z(\mathbf{r},t) &= 0 \end{aligned} \tag{3.15}$$

where $\mathbf{r}$ is the position of a particle, $\mathbf{r}_i(t)$ is the position of the fluctuation center at time t, and the sum is made on the number of fluctuations i. The parameter ℓ represents the decreasing scale of the vector potential, that we can imagine as the size of a magnetic cloud interacting with the particle (see [40]). The positions $\mathbf{r}_i$ are fixed randomly in the (x,y) plane and the perturbations oscillate with a velocity $V = 400$ km/s (namely, the typical value for the Alfvén speed in the magnetotail [42, 43, 44]) and with random phases. The electric field is obtained as $\mathbf{E} = -\bigtriangledown\phi - \partial\mathbf{A}(\mathbf{r},t)/\partial t$. Thus we have

$$\mathbf{E}(\mathbf{r},t) = E_{0y}\mathbf{e}_y + E_z(z)\mathbf{e}_z + \delta\mathbf{E}(\mathbf{r},t) \tag{3.16}$$

with E_{0y} the constant dawn-dusk electric field and where $E_z(z)$ is the electric field coming from the self-consistent solutions of equation (3.12) (see Figure 3.4), and $\delta\mathbf{E}(\mathbf{r},t) = \partial\mathbf{A}(\mathbf{r},t)/\partial t$ represents the time dependent fluctuating term of the electric field coming from equation (3.15). All the equations are normalized using the following normalization quantities : $L = 10^5$ km, $B_0 = 2$ nT and $E_0 = 40$ mV/m (see [34] for more details). The dawn dusk electric field is $E_{0y} = 0.2$ mV/m, the normal component of magnetic field is $B_n = 3$ nT, and the asymptotic value of the magnetic field in the lobes is $B_{max} = 20$ nT $= 10\ B_0$ [46]. The magnetic field $B_x(z)$ reaches its maximum (minimum) value for $z = L_z$ ($z = -L_z$), but most of the variation happens on scale λ. We inject simultaneously $N_p = 10^4$ particles in the simulation box at $t = 0$, at $z = 0$, and randomly distributed in the (x,y) plane; the starting coordinates x and y vary from 0 to L, where L is the size of the simulation box. Particles exiting the simulation box are substituted with freshly injected particles. The initial velocities for protons are extracted from a Maxwellian distribution with $v_{th} = 120$ km/s, corresponding to a temperature of $T_p = 0.1$ keV $\equiv E_{inj}$; heavier ions are injected with different thermal velocities in order to have the same initial temperature of protons. We numerically solve the

equations of motion

$$\frac{d\mathbf{r}}{dt} = \mathbf{v} \tag{3.17}$$

$$\frac{d\mathbf{v}}{dt} = \frac{q}{m}\left[\mathbf{E}(\mathbf{r},t) + \mathbf{v} \times \mathbf{B}(\mathbf{r},t)\right] \tag{3.18}$$

for each particle via a fourth-order Runge-Kutta scheme. The integration step is fixed to $\Delta t = 0.001\ \Omega_p^{-1}$, while $t_0 = \Omega_p^{-1} = 5$ s.

3.2.3 Meaning of model parameters

Before presenting the numerical results, we want to summarize the free parameters of the model and their physical meaning. Concerning the equilibrium electric and magnetic field profiles, we have:

- δ that is the background density, normalized with respect to the density of the first current-carrying population. The background population guarantees the positivity of the distribution function in the phase space;
- γ is the ratio between the density of the first and the second current-carrying populations;
- α is a very important parameter because it regulates the strength and the profile of the electric and magnetic fields. For examples, if $\alpha = 1$ the scalar potential is null, so that there is no electric field and the magnetic field has a typical profile $B_x(z) \sim 1/z$. Furthermore, if $\alpha = 0$ the scalar potential is negative and $B_x(z)$ has a local minimum, while if $\alpha = 10$ the scalar potential is positive and $B_x(z)$ has a local maximum. So that, for $\alpha \neq 1$ it is possible to obtain non-monotonous profile of the magnetic field which results in a more or less stretched current sheet configuration. We refere to [28] for more details.
- t_b is the ratio between background temperature and the ion temperature of the first population. Its value has an influence on the steepness of the magnetic field profile across the current sheet. In general for smaller values of t_b we obtain steeper profiles.

Concerning the configuration of the electromagnetic perturbation we have:

- A_0 is the amplitude of the perturbed vector potential.
- ℓ is the typical fluctuation size. This parameter is very important because it is connected to other quantities: the ratio A_0/ℓ which represent

the peak amplitude of the perturbed magnetic field, and $\sigma_{fl} = N_{fl}/\ell^2$ that is the surface density of the electromagnetic fluctuations. The parameter σ_{fl} is kept constant in all the simulations, so that if the fluctuations are larger then there are less fluctuations in the simulation box. In particular, we use $\sigma_{fl} \sim 39$ in arbitrary units.

- E_{inj} is the thermal energy of the Maxwellian distribution that describes the injected particles in the simulation box.
- $\mu = (m/m_p)/(q/q_p)$ is the ratio between the ion mass (m) and charge (q) normalized to the proton mass (m_p) and charge (q_p).

Chapter 4

Numerical Results

In the following section will be discussed the dependence of the numerical results on the parameter of the model, as for example the configuration of the current sheet, the amplitude of the perturbed magnetic field, and the size of the perturbations. Once chosen the best set of parameters, numerical results will be discussed for protons and heavy ion highlighting the role of the ion mass and charge state.

4.1 Parametric study

We set the initial condition of the numerical simulation using either $E_{inj} = 0.1$ keV or $E_{inj} = 1$ keV, and we collect the Probability Distribution Function (PDF) of the particle energy at the end of the simulation when $t = 500t_0$ (where $t_0 = \Omega_p^{-1} = 5$ s), in order to describe the particle statistical behaviour. The parameter A_0/ℓ and the profile of the current sheet configuration are changed among the different runs in order to study the dependence of the results on these. The other parameter are fixed; in particular we set $E_{0y} = 0.2$ mV/m, $B_{max} = 20$ nT, $B_n = 3$ nT, and we inject $N_p = 10^4$ particles in the simulation box at $t = 0$, at $z = 0$, and randomly distributed in the (x, y) plane. The starting coordinates x and y vary from 0 to L, where L is the size of the simulation box. Particles exiting the simulation box are substituted with freshly injected particles. We use different ions species, and heavier ions are injected with different thermal velocities in order to have the same injection energy E_{inj} of protons. Lets first consider H^+, He^{++} and O^+ and study the dependence of the PDF on the particular electric and magnetic field configuration and on the perturbed magnetic field amplitude A_0/ℓ, in particular, the spatial scale of magnetic perturbations is fixed as $\ell = 8000$ km, or equivalentely $R = \ell/L = 0.08$, consistently with the observations

(e.g., [43], [45], [34]), while A_0 is varied. We use two profile of the current sheet configuration which are the profile 1 and 2 shown in Figure 3.4, the first has a steeper variation of the magnetic field across the current sheet, and the second has a more gradual variation. Further, we use three levels of magnetic fluctuations namely $A_0/\ell = 10$ nT, $A_0/\ell = 3$ nT and $A_0/\ell = 1$ nT. The results for protons, helium and oxygen ions are summarized in Figure 4.1 (upper, middle, and bottom panel respectively). We can notice that the particular magnetic field profile $B_x(z)$ has very small influence, as shown by the PDFs being nearly overlapped in the cases of both profile 1 and profile 2. On the other hand, the particle energization increases with the perturbation strength, and protons and oxygen ions gain energies up to 100 keV, while helium ions reach energies up to 200 keV, in the case with large A_0. This means that the electromagnetic perturbations create an efficient accelerator for ions in the magnetotail (also shown in [47, 45]). Also, it is interesting to note that, for $A_0/\ell = 1$ nT, protons reach energies of 6.5 keV (see solid and dashed line in upper panel of Figure 4.1). Considering that, even during quiet geomagnetic times, the proton temperature in the magnetotail plasma sheet is observed to be of the order of 5 keV [41, 38, 39], and that a very small fluctuation level with $\delta B \sim 1$ nT is almost always present in the magnetotail [52], $A_0/\ell = 1$ nT is sufficient to heat the cold plasma coming from the solar wind to a temperature of $3 - 5$ keV [38].

Since the particular magnetic field profile of $B_x(z)$ has no influence on the results, in the following runs we choose to use the profile 1. Also, we fix $A_0/\ell = 10$ nT because this value is consistent with the spacecraft observations reported in [41]. Now we study the dependence on the initial energy setting $E_{inj} = 0.01$; 0.1; 1 keV and collecting the PDF for protons. Results are shown in Figure 4.2. We can observe that even if the initial energy changes, protons tend to reach the same final energy which is of about 100 keV. Therefore, we can conclude that the acceleration mechanism is not affected by the particular injection energy. Finally, we study the dependence on the typical size of the fluctuations $R = \ell/L$. In the case with profile 1, $A_0/\ell = 10$ nT, and $E_{inj} = 1$ keV, we ran simulations with $R = 0.02$; 0.04; 0.08 and 0.32. We remind that, the number of fluctuations N_{fl} decreases as R increases, in order to keep constant the fluctuation surface density $\sigma_{fl} = N_{fl}/\ell^2$. Varying R, the typical oscillation frequency of the fluctuations also changes. In particular it is proportional to V/ℓ, where V is the fluctuation propagation speed $V = 400$ km/s. We use four different values of R in order to check if there is some resonant acceleration that can favor the energization of a particular ion species which has the gyrofrequency closer to the fluctuation oscillation frequency. Results are summarized in Figure 4.3 for H^+, He^+, He^{++}, and O^+ ions (panels (a)-(d) respectively). It is possible to notice that

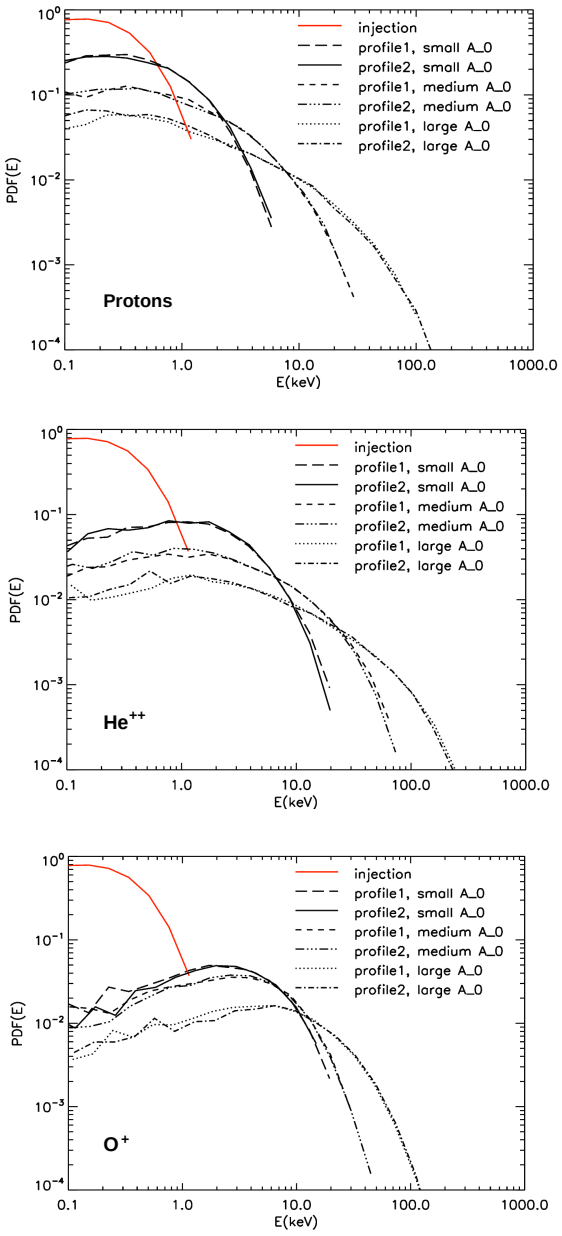

Figure 4.1: Comparison among the PDFs of energies of protons (upper panel), helium (middle panel), and oxygen (bottom panel) ions, in the presence of profile 1 and profile 2 (see Figure 3.4), by varying $A_0/\ell = 10$ nT (large A_0), $A_0/\ell = 3$ nT (medium A_0) and $A_0/\ell = 1$ (small A_0). The red lines display the distribution at the injection time with $E_{inj} = 0.1$ keV.

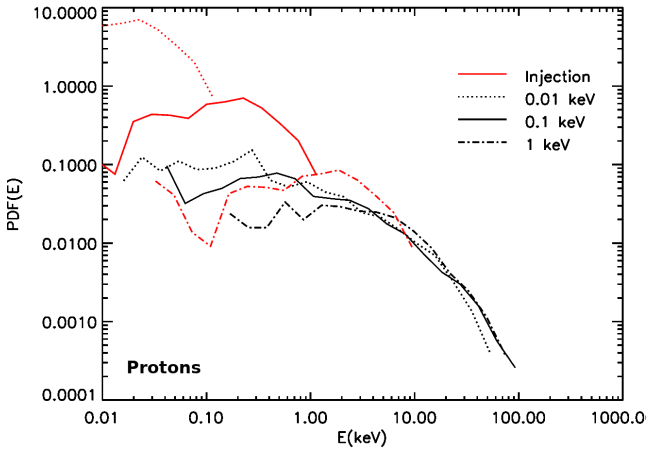

Figure 4.2: PDFs of the energy for protons in the case with $E_{inj} = 0.01$ keV (dotted line), $E_{inj} = 0.1$ keV (solid line), and $E_{inj} = 1$ keV (dash-dotted line); and with profile 1, $A_0/\ell = 10$ nT, and $R = 0.08$.

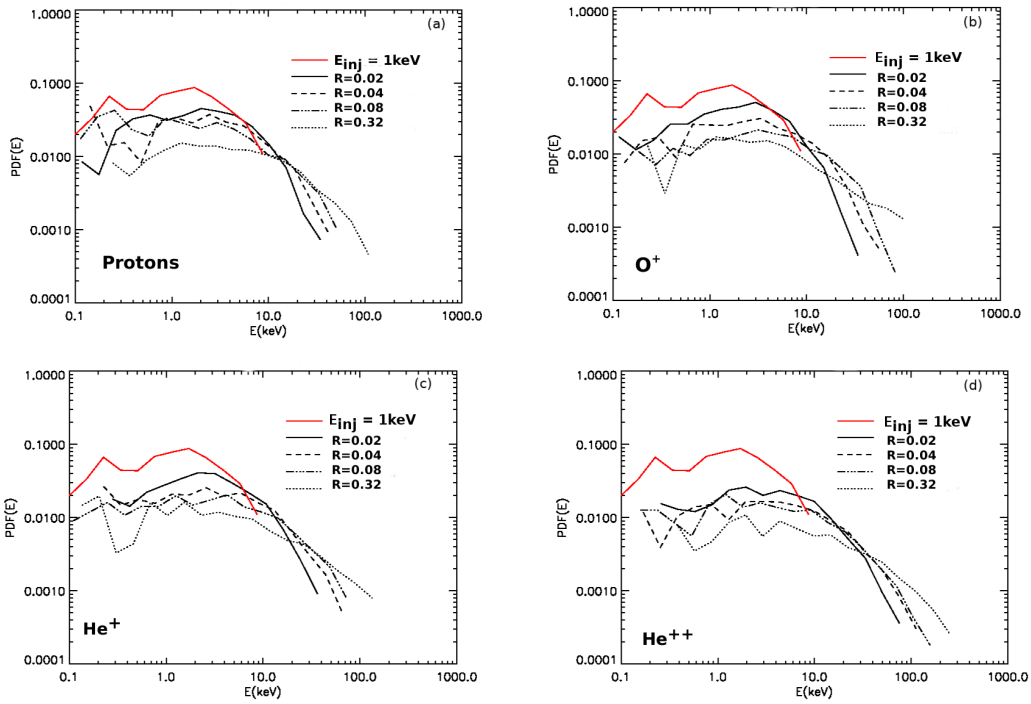

Figure 4.3: Comparison among the PDFs of energies of different ion species, in the presence of profile 1, with $A_0/\ell = 10$ nT, and different values of R (black lines). Red lines display the distribution at the injection time with $E_{inj} = 1$ keV.

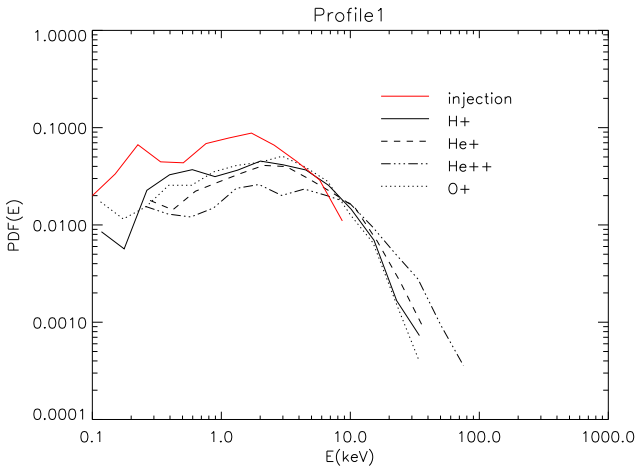

Figure 4.4: PDFs of the energy for H^+, He^+, He^{++}, and O^+ in the case with $E_{inj} = 1$ keV, $A_0/\ell = 10$ nT, R=0.08, and in the case with profile 1.

the final energy increases if the fluctuation size R is larger. This feature is observed for all the species in a similar way, so that we can conclude that the simulated acceleration mechanism has not resonant effects. This is in agreement with the fact that the perturbations represented by equations (3.15) mimic a stochastic Fermi model. Finally, setting R=0.08, $E_{inj} = 1$ keV, $A_0/\ell = 10$ nT, and in the case with profile 1 we investigate the acceleration of different ion species. We remember that in the stochastic Fermi acceleration, the energy gain of particles with the same initial energy should be the same, see equation (3.5). We can observe that H^+, He^+, and O^+ reach energy of about 100 keV, while only He^{++} ions reach larger energy. This suggest that the ion mass and especially the charge may play an important role in the acceleration mechanism. This also means that in the parabolic magnetic configuration of the magnetotail and because of the limited size of the simulation box (and of the actual magnetotail), stochastic acceleration yields results which also depend on the ion species. In addition, the original Fermi model assumes the specular reflection of the particles off the magnetic clouds; however, in the magnetotail particles like O^+ can pass through the magnetic perturbation with a finite size, with an interaction which is rather different from specular reflection. In the following section we will investigate in detail such idea comparing the results for a larger variety of ion species.

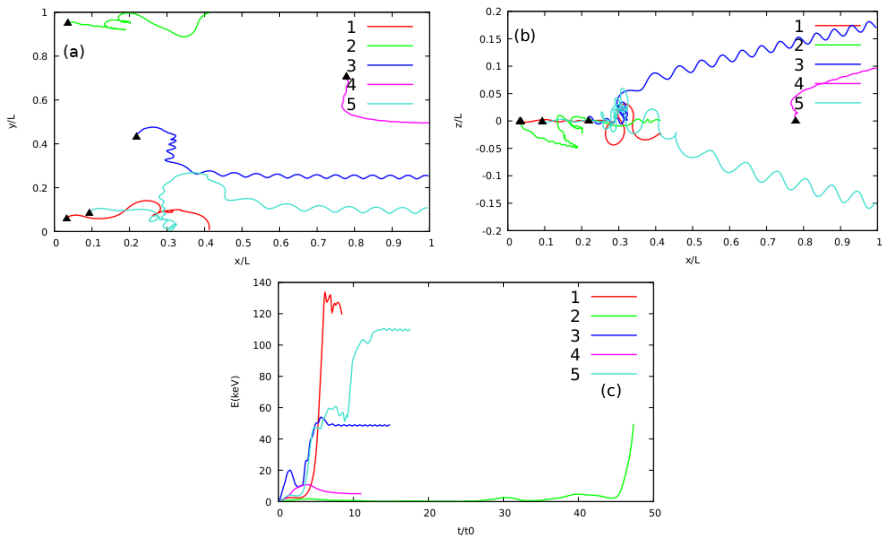

Figure 4.5: Trajectories and kinetic energies of protons in the presence of $B_x(z)$ as in profile 1. The fluctuation level is set to $A_0/\ell = 10$ nT, R=0.08, and $E_{inj} = 1$ keV. The coloured lines represent the particle orbits and their starting points are denoted by triangles.

4.2 Ion Dynamics

Before collecting and analysing the results for a large number of particles, it is worth trying to understand the behaviour of single particles in the simulation box.

4.2.1 Trajectories

To study the particle dynamics we have integrated the trajectories of a few particles using the profiles 1, and the parameters $E_{inj} = 1$ keV, R= 0.08, and $A_0/\ell = 10$ nT. In Figure 4.5 the projection of proton trajectories in the (x, y) and (x, z) plane (panel (a) and (b)), and energy as a function of the time (panel (c)) are shown for five particles. Black triangles represent the ion initial position which is at $z = 0$ and randomly in (x, y). We can notice that the parabolic structure of the large-scale magnetic field forces the particles to leave the box along the positive x direction (see panel (b) in Figure 4.5) and the ∇B drift along y determines the quasi-cycloid orbits. At $z \sim 0$, when the magnetic field $B_x(z)$ reaches the zero value, particles are less magnetized and the probability of being accelerated by the time-dependent fluctuations increases. Indeed, in this region particles experience frequent interactions with the electromagnetic fluctuations in the CS via a stochastic

Fermi process (see, for example, the blue trajectory in panel (b)). Particles can also be accelerated by the constant E_{0y} electric field. It is interesting to note that, as a result of the interaction with magnetic fluctuations, particles show a chaotic behaviour and exhibit a meandering motion (see red lines in panel (b)). Particles undergoing Fermi acceleration reach energies of up to 120 keV (red line in panel (c)).

This study is now performed by integrating heavier ions' trajectories within the above simulation model. The equations and the numerical integration are the same as the ones we used for protons, except that we change the ratio q/m in Equation (3.18). Figure 4.6 reports trajectories for those ions, and energies vs. time for profile 1. The black lines represent the He^{++} ions and red lines represent the O^{+} ions. We use the solid lines for particle 1, dashed lines for particle 2, and dashed-dotted lines for particle 3. Again, the triangles denote the starting point of the ions. At injection, the He^{++} ions have a Larmor radius $\rho_L^{He^{++}} = \rho_L^p \sim 600$ km, which is 0.078 times the size of fluctuations ℓ. Because of the equal Larmor radius, He^{++} ions interact with the fluctuations as protons do, but they can reach larger energy because of their double charge. This effect is discussed extensively in the next Section. The Larmor radius of O^{+} is $\rho_L^{O^+} = 4\rho_L^p \sim 2400$ km, which is ~ 0.3 times ℓ. Because of the larger Larmor radius, the electromagnetic fluctuations have a different effect on O^{+} ions. For example, we can compare the trajectories represented by the solid black line (for He^{++}) and red dashed line (for O^{+}) in Figure 4.6 (a). The two particles of different species have similar trajectories, broadly speaking. However, if we observe the energies vs. time (panel (b) and (c)), we notice that the He^{++} ions have been energized up to 300 keV, while O^{+} ions reach an energy of around 75 keV in a few interactions.

4.2.2 Scatter-plots

We may consider that the energy gain in a single interaction between ions and electromagnetic perturbations could be estimated as $dE = q\delta B V \Delta s$, where δB is the amplitude of the magnetic fluctuations, V is the oscillation speed of the perturbations, and Δs is the particle displacement within the perturbation fields. If Δs would be just proportional to the Larmor radius $\rho_L = mv_\perp/qB$, a strong mass dependence and no charge dependence should result. If $\rho_L > \lambda$ (with λ the current sheet thickness), $\Delta s \propto \lambda$ and the energy gain is only charge proportional; if $\rho_L < \lambda$, $\Delta s \propto \sqrt{\rho_L}$ [48], and the energy gain depends on the square root of both charge and mass. Since the model is time dependent, an intermediate scenario occurs. To gain further insights, we compute the local energy gain from the particle integration, and we made a scatter-plot of the average local energy gain $\langle dE \rangle$ as a function

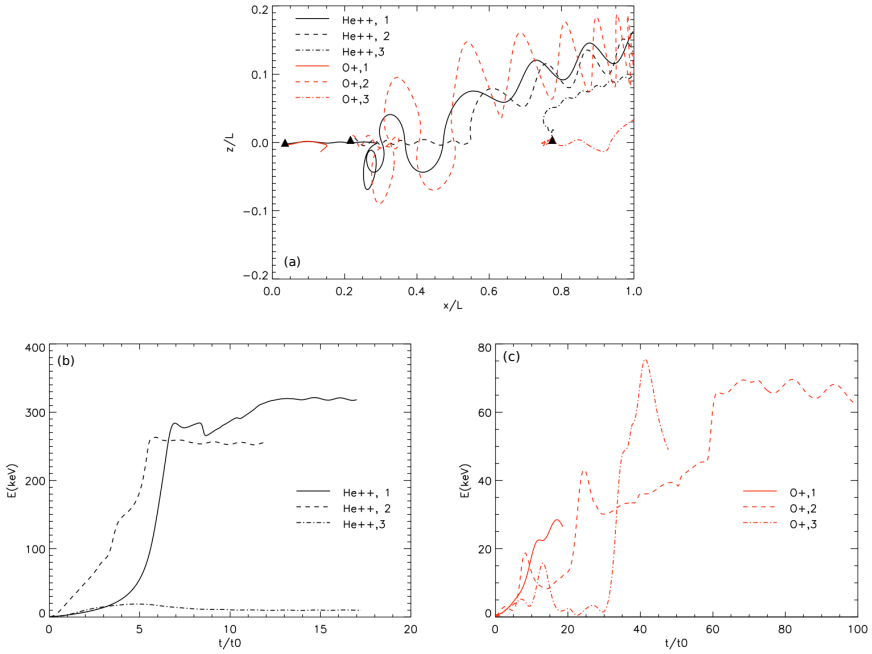

Figure 4.6: Trajectories and energies of He^{++} (black lines) and O^{+} (red lines) ions. Solid line represent particle 1, dashed line particle 2, and dashed-dotted line particle 3. The triangles denote the starting points.

of the local Larmor radius ρ_L normalized to the fluctuations size ℓ, for $N_p = 500$ particles. The average is made along the particle trajectories, computing dE for each time interval equal to the half gyroperiod of the species but considering only the cases when the particles are in the CS, that is, $|z| < \lambda$, where most acceleration is expected to occur. The results are shown in Figure 4.7, where the gray circles denote the H^+ ions, blue triangles the He^+, red squares the O^+, green crosses O^{++}, and black diamonds the O^{6+} ions. In all cases there is a growth of the energy gain with the Larmor radius, indicating that ions are more easily accelerated by the fluctuating fields when they are less magnetized, as expected. However, the energy gain increases proportionally to the ion charge. On average, O^{++} and O^{6+} ions have smaller Larmor radii than O^+, but their energy gains appear to be larger, suggesting the prevailing influence of the ion charge. From Figure 4.7(b) we can observe that oxygen ions on average have larger Larmor radii, but, compared to the other ion species with the same charge, the energy gain does not increase in proportion. This could be due to the fact that because of their large Larmor radius, the O^+ ions can exit the CS during their half gyroperiod, so that they are not accelerated for the whole time corresponding to a half gyroperiod.

It is also possible to study the energy gain considered along all the particle trajectories, and not only in the CS region, as $\Delta W = E_f - E_i$, that is the difference between final and initial particle energy. In Figure 4.8, we report the scatter plot of the energy gain ΔW, evaluated along all the ion trajectories, as a function of the averaged Larmor radius $\langle \rho_L \rangle / R$, normalized over the fluctuation size R. We used $N_p = 100$ trajectories for each ion species. The upper panel in Figure 4.8 shows the results for oxygen ions with different, colour coded, charge states. The bottom panel shows the result for singly charged ions with different mass, in particular O^+ (black dots), He^+ (blue dots), and H^+ (red dots). We notice that in the upper panel, ΔW clearly increases with the ion charge. Indeed, the magenta points, representing the O^{6+} ions, are observed in the left-upper side of the panel, having smaller ρ_L and higher final energies. These are followed by the O^{5+} ions (gray dots) and so on for smaller charge states. We also observe the O^+ ions (black dots) to the right-bottom region of the panel, corresponding to larger ρ_L and smaller energy gain ΔW. The bottom panel shows that the ion mass has a very weak influence on the energy gain, while it mostly affects the value of the Larmor radius.

Further, we can consider the acceleration rate as $\Delta W / \Delta t = q_i \delta B V v_i$. This quantity depends on the ion charge q_i and also on the particle velocity v_i. In analogy to the study for the energy gain, we report in Figure 4.9 the scatter plot of the acceleration rate $\Delta W / \Delta t$ as a function of the average of the normalized Larmor radius $\langle \rho_L \rangle / R$. In the upper panel are shown the

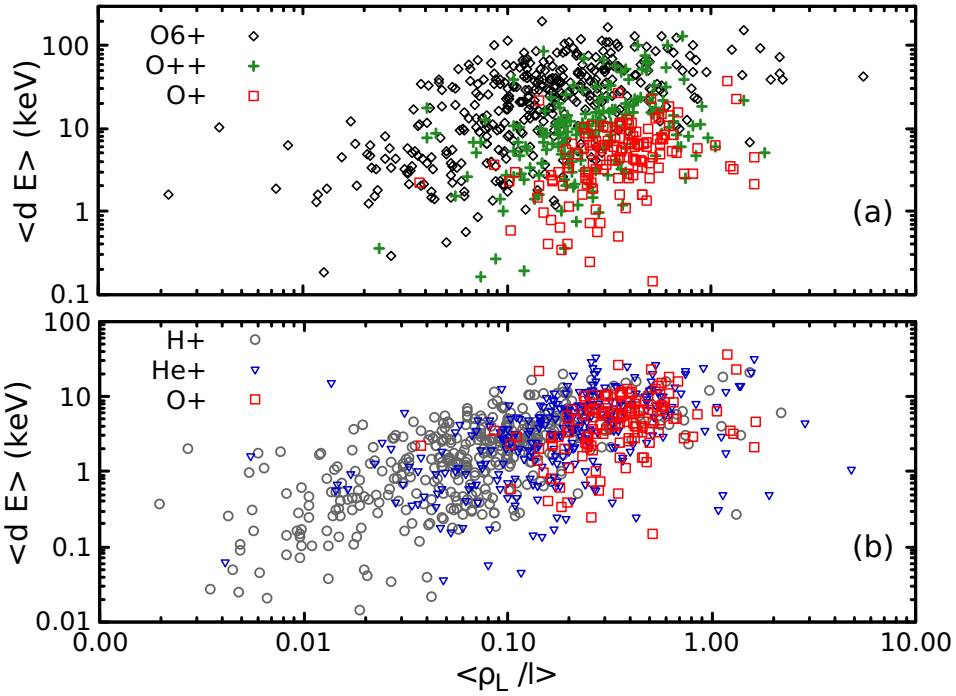

Figure 4.7: Scatterplot of the average energy gain $\langle dE \rangle$ as a function of Larmor radius ρ_L normalized to ℓ for (a) O^+ (red squares), O^{++} (green crosses), and O^{6+} (black diamonds); and (b) H^+ (gray circles), He^+ (blue triangles) and O^+ (red squares).

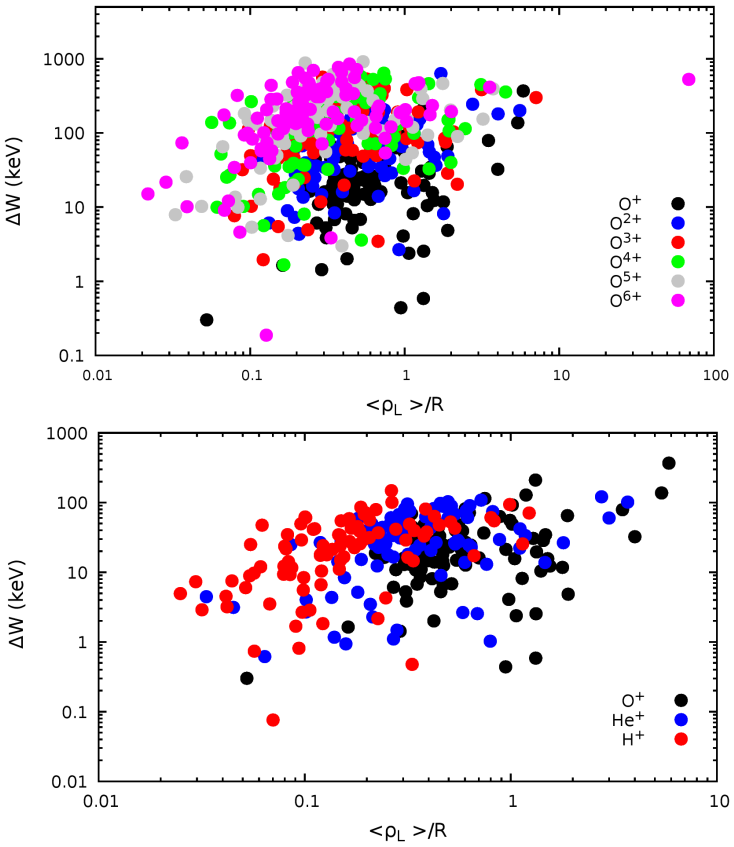

Figure 4.8: Energy gain ΔW as a function of the average of the normalized Larmor radius $\langle \rho_L \rangle / R$, for oxygen ions O^{n+} (upper panel) and singly-charged ions (bottom panel) O^+ (black), He^+ (blue), and H^+ (red).

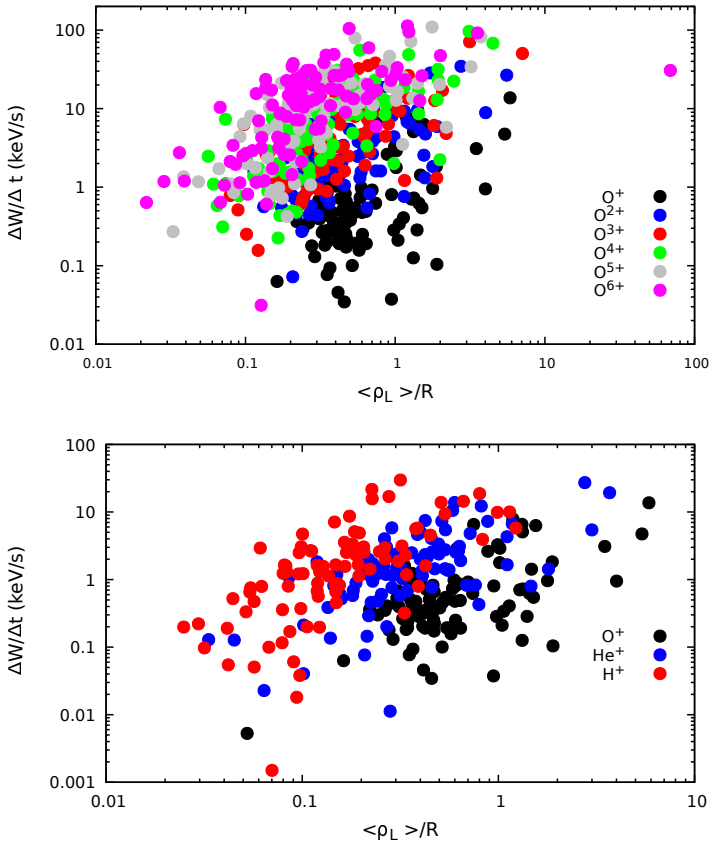

Figure 4.9: Acceleration efficiency $\Delta W/\Delta t$ as a function of the average of the normalized Larmor radius $\langle \rho_L \rangle / R$, for oxygen ions O^{n+} (upper panel) and singly-charged ions (bottom panel) O^+ (black), He^+ (blue), and H^+ (red).

results for the oxygen ions with different charge states, while the bottom panel shows the results for singly-charged ions with different masses. Again, looking at the upper panel, we can observe that the $\Delta W/\Delta t$ is well ordered with the ion charge, being larger for the ions with higher charge state. On the contrary, the ion mass influences only the value of ρ_L. However, in both the cases, the acceleration efficiency grows almost linearly with the Larmor radius.

Finally, we notice that for singly charged ions $\Delta W/\Delta t$ can reach values of $10 - 20$ keV/s, while for multiply charged oxygen ions $\Delta W/\Delta t \simeq 100$ keV/s can be reached; that is a rather remarkable acceleration rate.

4.3 Dynamics related to the κ parameter

One of most used parameter to study the motion of charged particles in the magnetotail is the κ parameter, presented for the first time in [55]. This parameter is defined as $\kappa^2 = R_{min}/\rho_{max}$, where R_{min} is the minimum curvature radius of the magnetic field, and ρ_{max} is the maximum Larmor radius of the particle in it, with a given energy. Therefore, this parameter is related to the magnetic moment and to adiabacity. The limit $\kappa \gg 1$ corresponds to the usual adiabatic case with the magnetic moment as first invariant of the motion. As κ decreases toward unity the magnetic moment can enhance or damp during the crossing of the current sheet, due to the overlapping of non-linear resonances between the bounce and the gyro-motion, and so the motion becomes stochastic and no more adiabatic [54, 55]. For $\kappa \simeq 1$ the motion is strongly chaotic and the first invariant of the motion may not be conserved. In the case of sharply curved field reversals, $\kappa < 1$, both a new kind of adiabaticity and a partially adiabatic but weakly chaotic type of motion appear. The motion for the case of $\kappa < 1$ is also known as *quasi-adiabatic*. In this regime particles can be trapped, quasi-trapped, or transient, as shown also in Figure 4.10. In [55] it is analytically shown that the particle dynamics is controlled by the adiabaticity parameter κ. Here we study the particle dynamics in our model considering the values of this parameter.

For our analysis the curvature radius is evaluated along a piece of trajectory of length ds, which corresponds to the particle position between to consecutive instant of time. Having the curvature radius, we evaluate the value of κ along the particle trajectories in different conditions by varying the values of the model parameters. In the following we show the results obtained with profile 1, setting R=0.08, $E_{inj} = 1$ keV, and $A_0/\ell = 10$ nT. The scope of this analysis is to understand if the particle energization occurs preferentially during regimes corresponding to particular values of κ. In Figure 4.11 we show a proton trajectory in the (x, z) plane. The value of κ is colour coded using green for $\kappa > 3$ corresponding to the adiabatic regime, cyan for $1 < \kappa < 3$ corresponding to the non-adiabatic regime, and yellow for $\kappa < 1$ which corresponds to the quasi-adiabatic regime. We observe that at the beginning the particle is near the equatorial region, where the electromagnetic perturbations are stronger. So that, the particle interacts with the fluctuations and makes a meandering motion. Here we observe the quasi-adiabatic regime, as also shown in the bottom panel of Figure 4.11 which is a zoom of the trajectory in x. Then we observe the non-adiabatic regime (cyan points) as the particle goes away from the equatorial region. Finally, when the particle is far away from the CS, we observe the adiabatic regime (green points) with the typical motion of strongly magnetized particles.

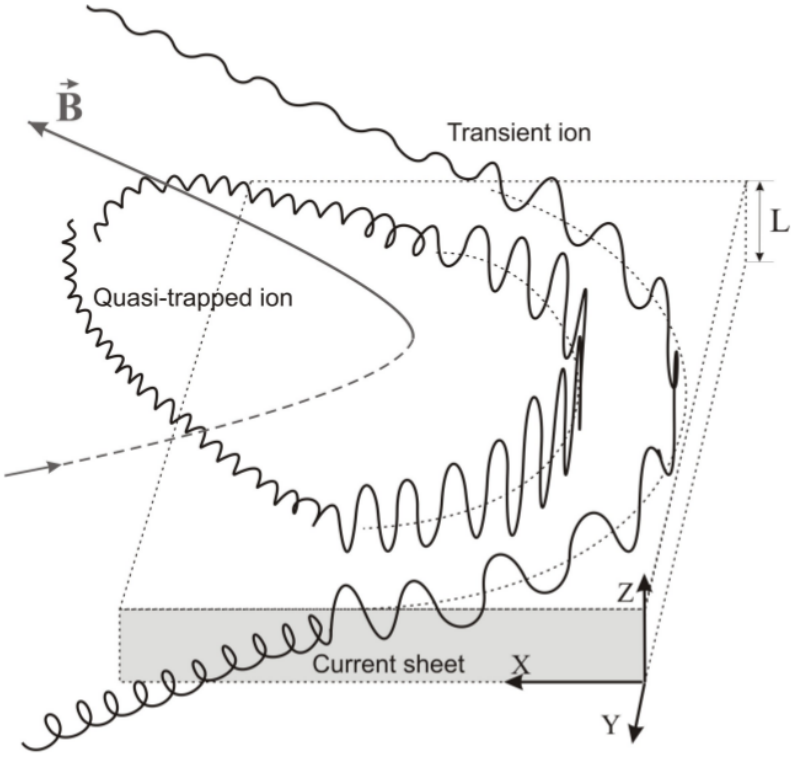

Figure 4.10: Scheme of quasi-trapped and transient ion dynamics in a model of a thin current sheet. Credit: [56].

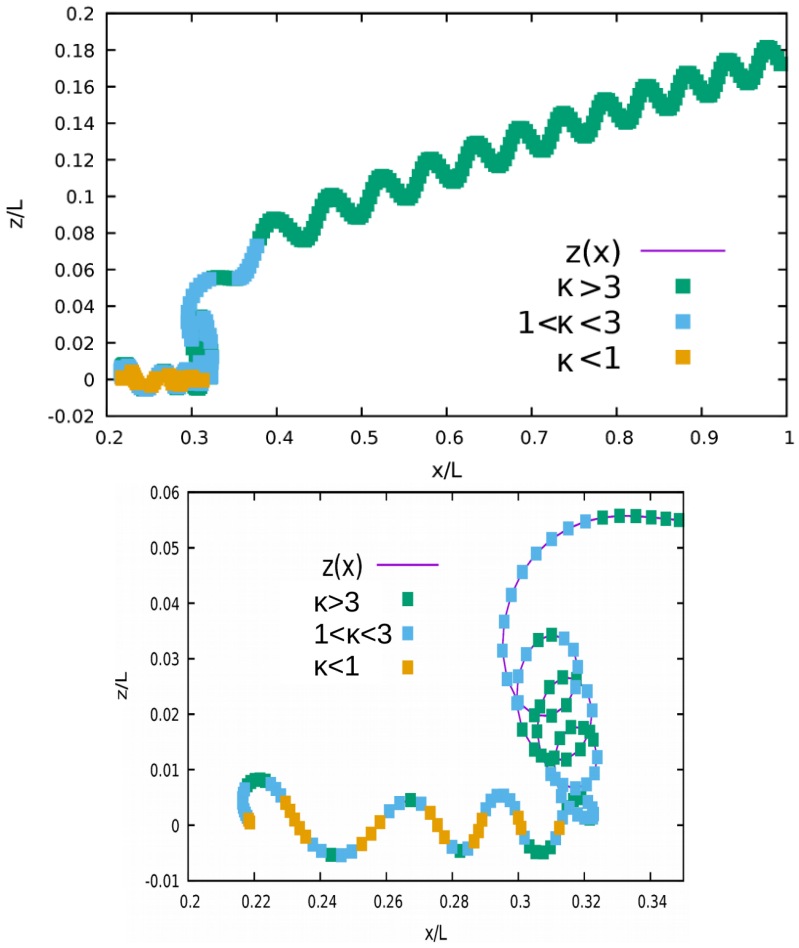

Figure 4.11: Proton trajectory in the (x, z) plane. The value of κ is colour coded using green for $\kappa > 3$, blue for $< 1\kappa < 3$, and yellow for $\kappa < 1$. Bottom panel is zoomed in x.

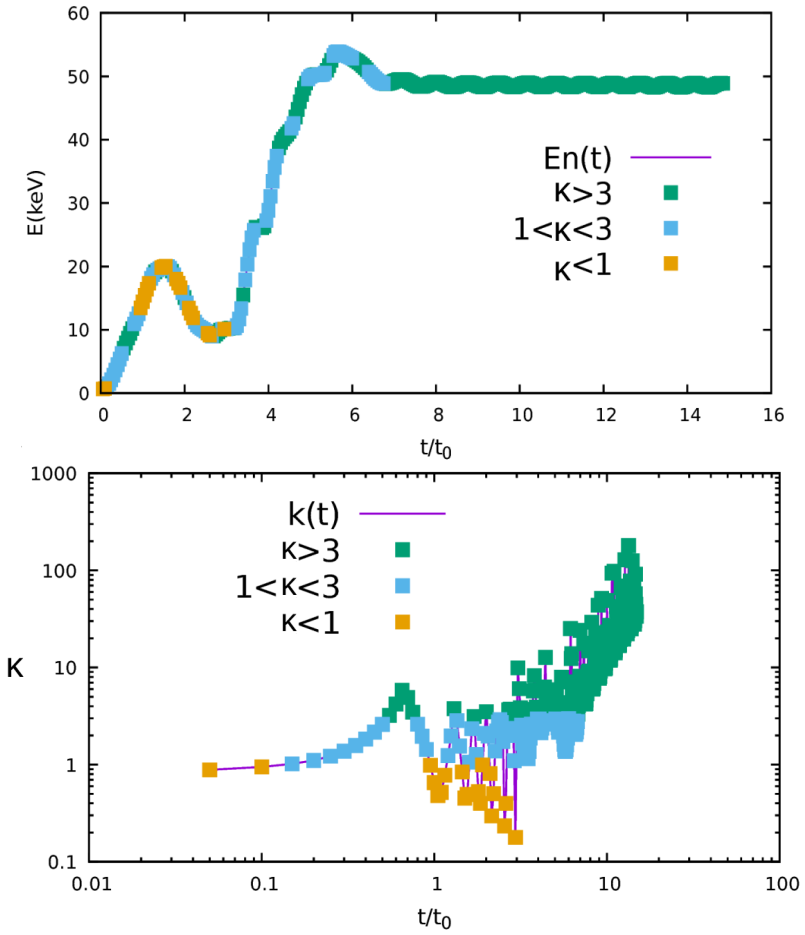

Figure 4.12: Proton energy (upper panel) and κ (bottom panel, logarithmic scale) as a function of time. The values of κ are colour coded.

By looking at Figure 4.12, we observe the proton energy and the values of κ as a function of time. When the particle is in the equatorial region performs a Fermi-like acceleration, gaining or loosing energy. This behaviour corresponds to the energy increase and decrease at around $t/t_0 \sim 2$, mainly in a quasi-adiabatic regime with $\kappa < 1$ (yellow points). Most of the energy is gained during the non-adiabatic regime with $\kappa \simeq 1$ (cyan points), while during the adiabatic regime with $\kappa \gg$ (green points) the energy is almost constant.

Finally, Figure 4.13 shows the magnetic (upper panel) and electric (middle panel) field components as observed by the particle, and the κ parameter and proton energy (bottom panel) as a function of time. We can see that the largest energy gain, between the vertical dashed lines, is in correspondence

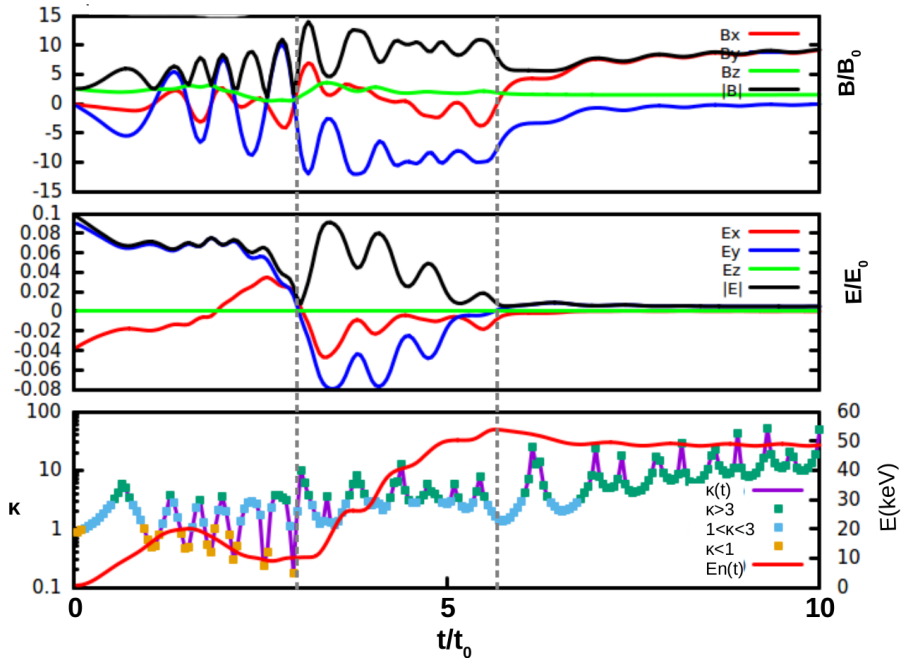

Figure 4.13: Magnetic (upper panel) and electric (middle panel) field components as observed by the particle as a function of time. κ parameter and proton energy as a function of time (bottom panel). Vertical dashed lines denote the region with largest energy gain.

with the strong electric fluctuations.

We repeat the same analysis changing the strength of the electromagnetic perturbations by using $A_0/\ell = 10$, 3, 1 nT and $N_p = 500$ particles. In order to summarize the results is these different conditions we evaluate the local energy gain as

$$\left(\frac{\Delta W}{\Delta t}\right)_i = \frac{W(t_{i+1}) - W(t_i)}{t_{i+1} - t_i}, \tag{4.1}$$

where W is the particle energy at a given instant of time t_i. Then we averaged the local energy gain obtained in a particular regime obtaining $(\Delta W/\Delta t)_n$. In Figure 4.14 the results are summarized.

First, we observe that when the strength of the fluctuations is larger the energy gain increases, in agreement with the prevailing influence of the electric field perturbations. Then we observe that most of the energy gain occurs for $\kappa < 1$ in the quasi-adiabatic regime and for $\kappa \simeq 1$ in the non-adiabatic regime. Both these regimes correspond to the situation in which particles are near the equatorial region interacting with the perturbations. So, we can say that the parameter κ is useful to describe the particle dynamics, indicating

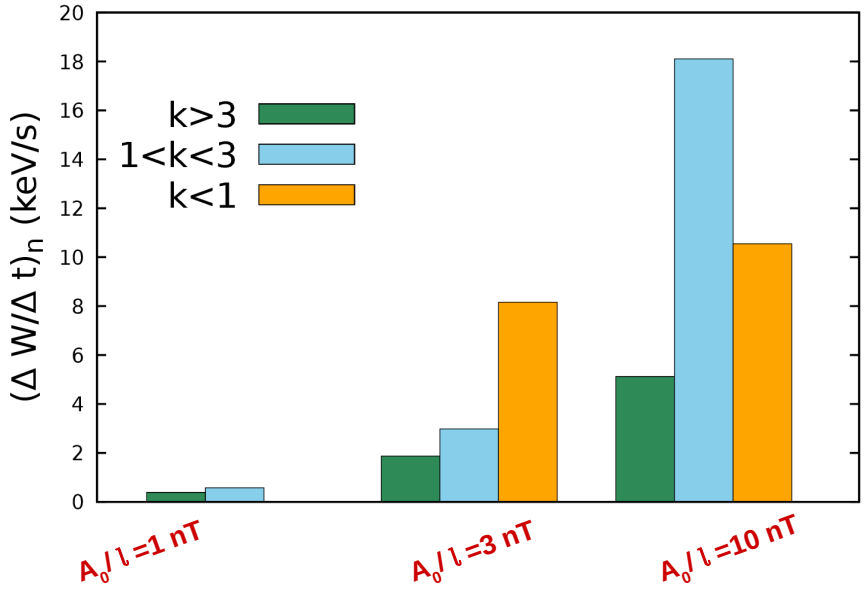

Figure 4.14: Averaged local energy gain $(\Delta W/\Delta t)_n$ obtained for $N_p = 500$ particles in the case of $A_0/\ell = 10$, 3, 1 nT. The values of κ corresponding to the different regimes are colour coded.

that regime the energization occurs mainly for $\kappa < 3$.

4.4 Statistical Results

In order to have a global description of particle energization, and also for the purpose of comparison with observations, we now compute the energy distribution function for a large number of particles. We set the parameters $E_{inj} = 1$ keV, $A_0/\ell = 10$ nT, and R=0.08. We collect the results at the end of the simulation for $N_p = 10^4$ particles. For each ion species we evaluate the PDF as a function of energy and, in order to get the final thermal energy $E_{th} \propto k_B T$, we fit the PDF with a Maxwellian distribution. The fit returns the value of E_{th}. Also, we describe the high-energy tails (i.e., the part of the PDF which is not approximated by the Maxwellian distribution) using a power-law $f(E_i) \propto E_i^{\gamma}$, where γ is the spectral index which describes the slope of the tail. Finally, we evaluate the residence time in the current sheet τ_{CS} in percentage with respect to the total time spent in the simulation box. The condition to individuate the CS region is for $|z| \leq \lambda$. We consider this region because, as shown above, it is where the ions gain most of the energy interacting with the fluctuations that are stronger around $z \simeq 0$. Results of

E_{th}(keV)	γ	τ %	species
1.4	-1.27	12	H^+
2.6	-0.94	3	He^+
3.6	-0.82	6	He^{++}
10	-	0.5	O^+
8	-1.41	1.2	O^{++}
8.4	-1.07	2	O^{3+}
8.5	-1.12	2.7	O^{4+}
8.7	-1.38	3.2	O^{5+}
9	-1.15	4.4	O^{6+}

Table 4.1: Spectral index γ and of residence time in the CS τ for each ion species.

the parameter E_{th}, γ and τ are reported in Table 4.1 for each ion species.

In Figure 4.15 we report the results for protons. We notice that these ions have a quite small thermal energy, but they develop an high-energy tail. We consider that this is due to the fact that they spend a long time in the CS, almost 12% of the total simulation time. Therefore, they have the chance to interact many times with the fluctuations undergoing a Fermi-like acceleration mechanism which lead to the formation of a power law energetic tail, as Shown in Chapter 3, even if it is not so steep (see Table 4.1). Finally, we note that protons reach energy up to 100 keV.

Figure 4.16 shows the results for He^+ and He^{++} ions. First, we note that both the helium ion species have larger E_{th} respect to protons. However, helium ions have less steep tails, in particular He^{++} has the flatter tail with $\gamma = -0.82$. Also, He^+ reaches energy up to 100 keV, while He^{++} up to 200 keV.

Results for oxygen ions are shown in Figure 4.17. It can be seen that the O^+ distribution function is very close to Maxwellian (panel (a)), whereas the other ions develop non-thermal power law tails. Also the final energy increases considering multiply-charged oxygen ions. In particular it goes from $\sim$ 100 keV for O^+, up to $\sim$ 500 for O^{6+}. Furthermore, the residence time τ_{CS} is larger for ions with higher charge state, in agreement with the fact that they have smaller gyroradius.

In Figure 4.18, we investigate the dependence of τ_{CS} on the mass-over-charge ratio $\mu = (m/m_p)/(q/q_p)$ normalized to the one for protons. We can see that τ_{CS} is well ordered with μ. Clearly, this is due to the fact that μ is proportional to the Larmor radius (see also the trajectories in Figure 15 of [49]

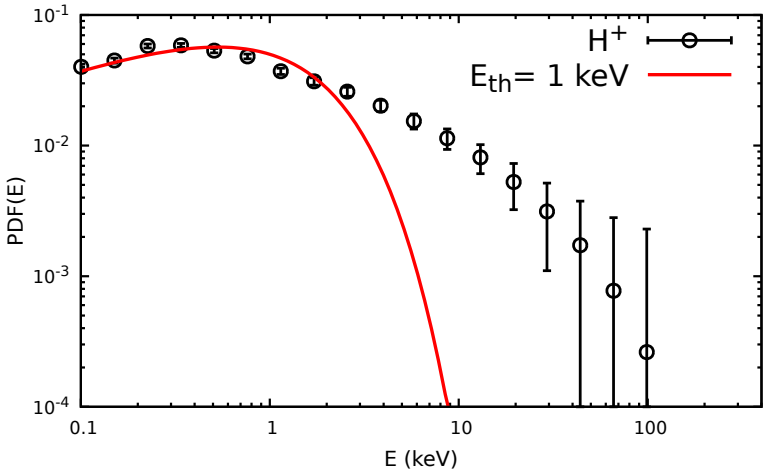

Figure 4.15: PDF as a function of energy for protons fitted by a Maxwellian distribution (red line).

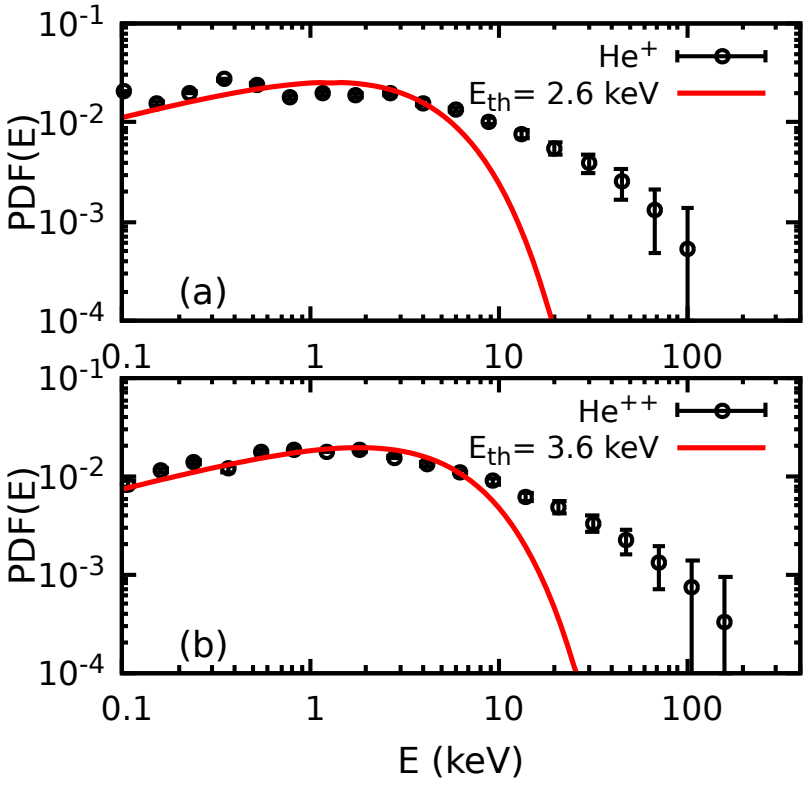

Figure 4.16: PDF as a function of energy for helium ions fitted by a Maxwellian distribution (red line).

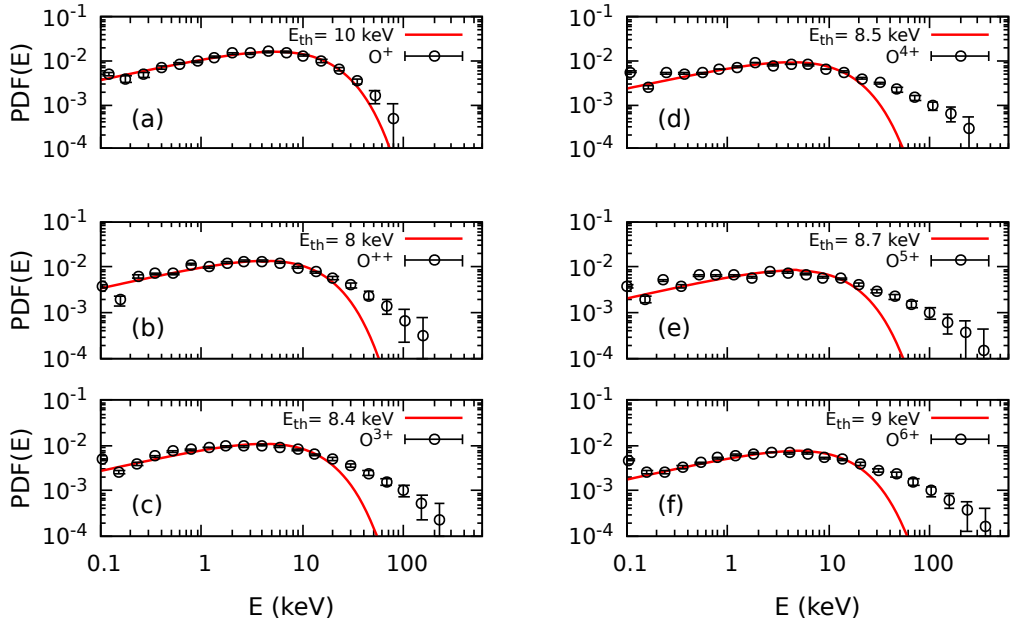

Figure 4.17: PDF as a function of energy for oxygen ions fitted by a Maxwellian distribution (red line).

and in Figure 5 of [50]). Therefore, ions that spend a longer time in the CS interact many times with the random fluctuations and undergo a Fermi-like process, thus developing the power law tail. Conversely, ions which spend a limited time in the CS, have a nearly Maxwellian PDF. The power law tails have been fitted, and the best fits give a slope γ that decreases (flatter tails) as τ_{CS} increases, in agreement with stochastic Fermi acceleration [7]. It should be noted that the slopes of the power law part of the ion PDF, reported in Table 4.1, are in the range $\gamma \cong$ 0.8-1.4, while in many spacecraft observations $\gamma \sim$ 4-5 (see for example [19]). This discrepancy suggests that other energization mechanisms, possibly more directly related to magnetic reconnection, are prevailing in the magnetotail.

From the insets in Figure 4.18 it is possible to note that τ_{CS} has not a unique trend with the ion mass or charge, separately (panels (a) and (b)). Following the red lines in Figure 4.18(a), we can see that the residence time decreases with the ion mass. In a similar way, following the green lines in Figure 4.18(b), we find that the residence time increases with the charge state. These results show that the residence time depends on the ion mass for a specific charge and on the charge for a specific mass. It is also worth noting that the maximum energy of the ions reported in Figures 4.15,4.16, and 4.17 does not increase with the residence time in the current sheet, as

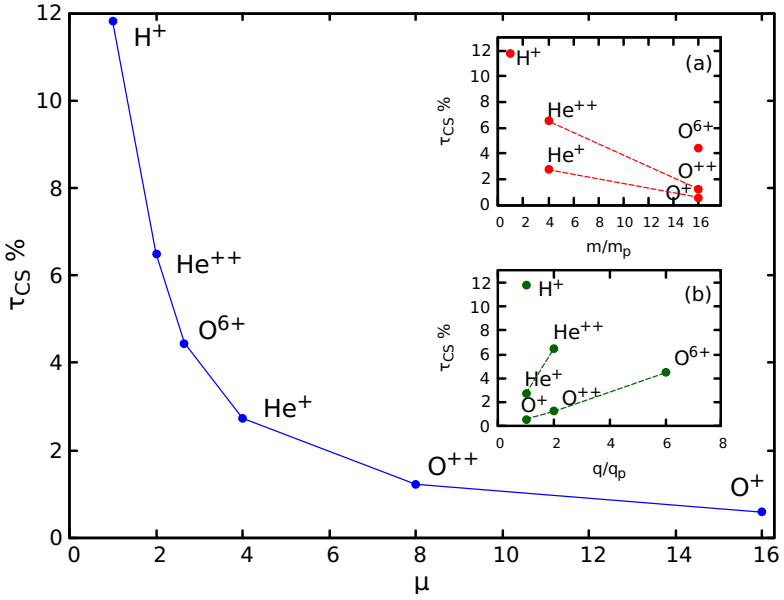

Figure 4.18: Residence time in the CS for different ion species as a function of the normalized mass-to-charge ratio μ. The insets show the residence time as a function of (a) mass and (b) charge state normalized to those of protons. The residence time is given in percentage with respect to the total residence time in the simulation box. The red lines in (a) connect the ions with equal charge state, while green lines in (b) connect ions with equal mass.

found by [35], too.

To quantify the acceleration dependence on the charge and mass, we consider the 10% of the test particle population that experience the largest energization $\Delta E = E_f - E_i$, where E_f is the final energy and E_i is the initial energy of each particle. Figure 4.19 shows the average energy gain $\langle \Delta E \rangle_{10\%}$ as a function of the charge (Figure 4.19(a) and (c)), mass over charge ratio (Figure 4.19(b)), and mass (Figure 4.19(d)) for different ions. First we consider the case with $E_{inj} = 1$ keV and ions O^{n+}, with n =1–6 (Figure 4.19(a)). We can see that the energy gain grows with the ion charge. The best fit (black dashed line) shows that the energization linearly depends on the charge state, and the slope was found to be 92 keV/ q with a value of $\chi^2 \sim 0.008$. Figure 4.19(b) displays the same quantity for different ions as a function of the parameter μ. It can be noted that the energy gain is not ordered in a simple way with μ for all ion species. However, from this panel it is clear, once again, how the energization increases with the charge state at a fixed mass (dashed lines). In order to further investigate the role of ion mass and charge, we performed further runs introducing virtual particles that is,

protons with charge larger than one. Testing the model with ad hoc particles is a tool to better investigate the dependence on ion mass and charge. In Figure 4.19(c) we report the simulation results for ions with constant mass $m_i = m_p$ and charge ratio $q_i/q_p = 1;\ 2;\ 3;\ 4$; while in Figure 4.19(d) for the case with constant charge $q_i = q_p$ and different mass ratio $m_i/m_p = 1;\ 2;\ 4;\ 8;\ 16$. We perform the simulations using injection energy equal to $E_{inj} = 1$ keV and $E_{inj} = 0.1$ keV (red and blue symbols, respectively). The lower energy corresponds to the cold ions that are sometimes observed in the magnetotail [51]. The linear fits (dashed lines) in 4.19(c) return a value of $\chi^2 < 0.02$, and the slope is ~ 44 keV/ q for both cases. We stress that this slope is smaller than the one obtained for oxygen ions, showing a dependence on the mass. Altogether, we can conclude that $\langle \Delta E \rangle_{10\%}$ linearly depends on the ion charge. On the other hand, looking at 4.19(d), we can notice that the energy gain has a weaker dependence on the ion mass. In particular, $\langle \Delta E \rangle_{10\%}$ is approximately proportional to $m^{1/5}$ with a $\chi^2 < 0.018$. The best fit analysis (dashed lines), indicates that this dependence is weaker than the square root of the mass $\sqrt{m}$, at variance with what was found in [81]. This is also different from the energy gain expected for nonadiabatic orbits in the dawn-dusk electric field E_{0y}, for which ΔE is mass proportional (see [49] and [54]).

4.5 Conclusions

In summary, in this chapter we performed numerical simulations in order to study the acceleration of protons and heavy ions, due to the interaction of time-dependent electromagnetic fluctuations in the terrestrial magnetotail. First, we find a very weak influence of the particular current sheet configuration on the acceleration mechanism. By varying the fluctuation size ℓ or the initial energy E_{inj}, we observe that there is not a resonant acceleration with ions having their Larmor radius closer to the value of ℓ. The study of the ion dynamics in particular regimes, related to the value of the k parameter, demonstrates that most of the energization occurs during stochastic ($1< k <3$) and quasi-adiabatic regimes ($k <1$). Also, we find that the ions which spend more time in the CS, interacting with the fluctuations, undergo a Fermi-like acceleration mechanism leading to the formation of high-energy tail. The residence time in the current sheet τ_{CS} is well ordered with the ion charge, at a fixed mass, and vice versa. In particular it increases with the ion charge state. Also, we find that the average energy gain for the 10% of the most energetic ions, $\langle \Delta E \rangle_{10\%}$, increases linearly with the ion charge, while it has a weak dependence on the ion mass. Therefore, if ions have larger mass

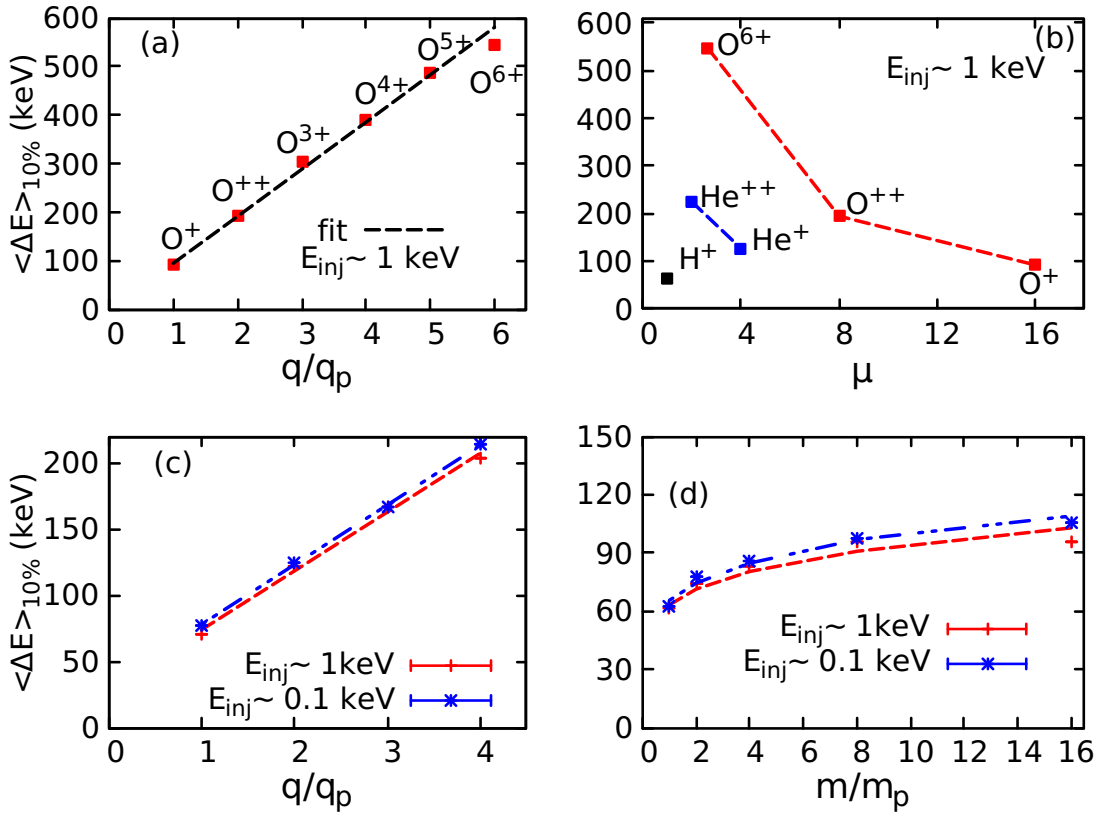

Figure 4.19: Energy gain of the top 10% energetic particles as a function of (a) charge and (b) mass-to-charge ratio for the case with $E_{inj} = 1$ keV. The same quantity is given for ad hoc particles (see text for details) as a function of their charge state (c) and mass (d), respectively. The red (blue) points represent the case with $E_{inj} = 1$ keV (0.1 keV). Dashed lines are used to show the best fit, while the thin dashed lines in (b) connect ions with equal mass.

and larger ion charge state they can reach higher energies. These results are in agreement with spacecraft observations showing that, for energies larger than ~ 150 keV, ions are dominantly heavy multiply-charged species, as reported in [26, 27] and [25]. By observing the values of the spectral indeces γ obtained from our model for different ion species, we observe that they are different from the typical one obtained from spacecraft observations of the ion population in the terrestrial magnetotail [19]. This can be due to the fact that we evaluate the spectral index for each ion species, while from the spacecraft observations it is reported the spectral index for the distribution of all the ions together, and not for the single species. However, our model describes only a small portion of the possible acceleration mechanisms acting in the magnetotail. For a complete description on the acceleration processes we can imagine that a similar stochastic process can be at work jointly with other mechanisms in a multi-step acceleration process. Other examples of acceleration mechanisms are discussed in the following chapters.

Chapter 5

Spacecraft mission and data analysis

The Earth's magnetosphere is the closest natural laboratory where it is possible to study in detail the plasma processes. Numerous spacecraft mission have been devoted to study the environment around our planet by using technological instruments and efficient design. In the last decades the study of plasma phenomena at different scales has became very important, thus multi-spacecraft missions became the most funded by the space agencies. The Magnetospheric MultiScale (MMS) mission by NASA is the most recent.

5.1 The Magnetospheric MultiScale mission

NASA launched the Magnetospheric Multiscale (MMS) mission on March 12, 2015. MMS consists of four identical spacecraft that orbit around the Earth through the dynamic magnetic system surrounding our planet (see illustration in Figure 5.1), to study the mystery of how magnetic fields around Earth connect and disconnect, explosively releasing energy via a process known a magnetic reconnection. Such phenomena occurs when magnetic field lines cross and release a gigantic burst of energy. It is a fundamental process throughout the universe that taps the energy stored in magnetic fields and converts it into heat and energy in the form of charged particle acceleration and large-scale flows of matter. However, magnetic reconnection can only be studied in-situ in our solar system and it is most accessible in near Earth space, where MMS is studying it. Besides MMS, no mission is currently dedicated to the study of this phenomena. By studying reconnection in this local, natural laboratory, MMS helps us understand reconnection elsewhere

as well, such as in the atmosphere of the sun and other stars, in the vicinity of black holes and neutron stars, and at the boundary between our solar system's heliosphere and interstellar space.

The mission objectives are:

- By observing magnetic reconnection in nature, MMS provides access to predictive knowledge of a universal process that is the final governor of space weather, affecting modern technological systems such as communications networks, GPS navigation, and electrical power grids. MMS establishes knowledge, methods and technologies applicable to future space weather missions and the future growth and development of space weather forecasting.

- The four identically instrumented MMS spacecraft fly in an adjustable pyramid-like formation that enables them to observe the three-dimensional structure of magnetic reconnection. This enables them to determine whether reconnection occurs in an isolated spot, everywhere within a larger region at once, or travelling across space. MMS sensors measure charged particle velocities, as well as electric and magnetic fields, with unprecedented (milliseconds) time resolution and accuracy needed to capture the elusively thin and fast-moving electron diffusion region. MMS probes reconnection of solar and terrestrial magnetic fields in the dayside and nightside of Earth's magnetosphere.

5.1.1 Instrumentation used in this study

In this section are briefly described the characteristics of the instruments on board on the MMS spacecraft. For more detail we remand to the dedicated web-page [1]. Figure 5.2 displays a view of all the four spacecraft in the cleanroom. For brevity, in the following we focus only on the instruments used for the analysis of the events studied in this thesis.

FIELDS

The FIELDS (electric and magnetic fields) investigation includes a sensor suite consisting of two axial and four spin-plane double-probe electric-field sensors (ADP and SDP), two flux-gate magnetometers (AFG and DFG), a search-coil magnetometer (SCM), and two electron drift instruments (EDI) per MMS spacecraft. These instruments measure the DC magnetic field with a resolution of 10 ms, the DC electric field with a resolution of 1 ms, electric

[1] https://lasp.colorado.edu/mms/sdc/public/about/

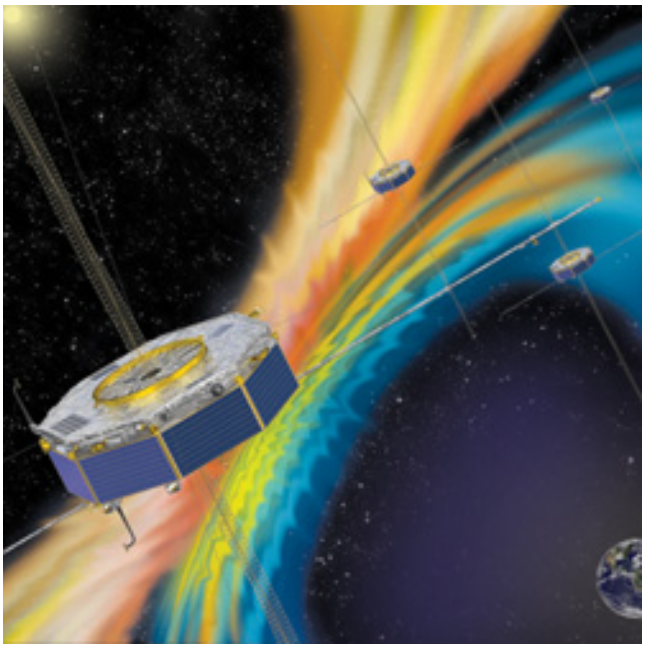

Figure 5.1: Illustration of the four MMS spacecraft in orbit in Earth's magnetic field. Credit: NASA

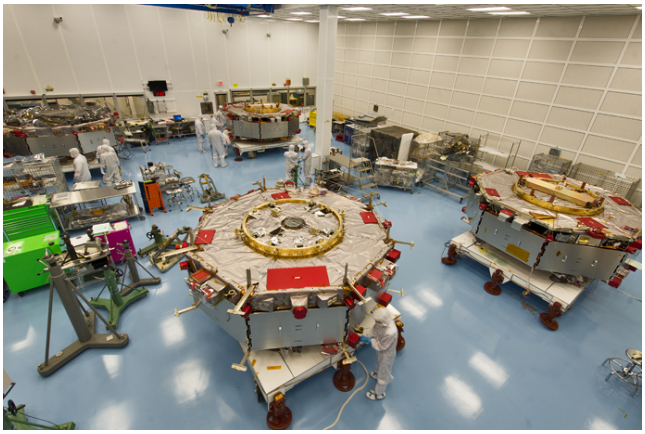

Figure 5.2: MMS four separate-view of all four spacecraft in the MMS Cleanroom getting prepared for stacking operations. Photo credit: NASA/Chris Gunn

.

plasma waves up to 100 kHz, and magnetic plasma waves up to 6 kHz [57]. FIELDS consists of five subsystems: the Fluxgate Magnetometers (FGM), the Axial Double Probes (ADP), the Spin-plane Double Probes (SDP), the Search Coil Magnetometer (SCM), and the Electron Drift Instrument (EDI). We describe more in detail only the instrument used for the data analysis described in the next chapter.

- The fluxgate magnetometer (FGM) instrument on board MMS consists of eight individual magnetometers, two per spacecraft. For each spacecraft one of the magnetometers is known as the Analog Fluxgate (AFG) magnetometer, the other as the Digital Fluxgate (DFG) magnetometer. Flying both the AFG and DFG magnetometers provides redundancy, but, in addition, the overall calibration of the instrument is significantly enhanced by inter-calibrating all eight magnetometers. This is essential for data quantities such as current densities, that require high precision measurements. FGM measures the magnetic field with a sampling of 128 Hz [58].

- The Spin-plane Double Probe (SDP) [59] and Axial Double Probe (ADP) [60] electric field instruments are collectively known as EDP (Electric field Double Probe). EDP measures the 3-D electric field with an accuracy of 0.5 mV/m over the frequency range from DC to 100 kHz. SDP consists of four biased spherical probes extended on 60 m long wire booms 90° apart in the spin plane, giving a 120 m baseline for each of the two spin-plane electric field components. ADP consists of 2 biased cylindrical probes extended on $\sim$ 12 m long stiff booms along the spacecraft axis, giving a 29.2 m baseline for the axial electric field component.

FPI

The Fast Plasma Investigation (FPI) [61] includes four dual electron spectrometers (DES) and four dual ion spectrometers (DIS) per spacecraft. When the data from the two sets of four dual-spectrometers are combined, FPI is able to provide the velocity-space distribution of electrons from 10 eV to 30 keV and ions from 10 eV to 30 keV with a time resolution of 30 ms, and 150 ms, respectively. This high temporal resolution in 3D phase space measurements is unprecedented in the history of scientific space flight and by far the single biggest driver on the design and implementation of the experiment.

EDP

The Energetic Particle Detector (EPD) [24] includes an Energetic Ion Spectrometer (EIS) and two all-sky particle samplers called the Fly's Eye Energetic Particle Sensor (FEEPS) per MMS spacecraft. These instruments measure the energy-angle distribution and composition of ions (20 to 500 keV) at a time resolution of < 30 seconds, the energy-angle distribution of total ions (45 – 500 keV) at a time resolution of < 10 seconds, and the coarse and fine energy-angle distribution of energetic electrons (25 – 500 keV) at time resolutions of < 0.5 and < 10 seconds, respectively.

5.2 Magnetic reconnection

The targets area of the MMS mission are the dayside and nightside region where magnetic reconnection frequently occurs. These regions are highlighted using shadowed areas in Figure 5.3. In the next chapters we will describe two events observed by MMS in the terrestrial magnetotail (or the nightside area), and in the souther magnetospheric flank, which is the region souther (or northern) with respect to the solar wind direction where the plasma from magnetosheath can mix with the plasma from magnetopause due to some instability (see Figure 2.1 for details). We reserve a more specific description of each region for the dedicated chapters. Now we introduce a process that is common not only in these two regions, but in all the plasmas present in the universe, that is magnetic reconnection.

5.2.1 Phenomenological description

Magnetic reconnection is the fundamental mechanism by which magnetic energy is dissipated in the universe. It is a fundamental plasma physics process during which a change of the topology of the magnetic field occurring at small scales leads to energy dissipation and plasma transport, heating and acceleration at large scales [62]. Reconnection takes place at the boundary of different magnetic fields, which is a region of strong current, i.e., a current sheet. The change of the magnetic topology associated with reconnection is related to the violation of the so-called frozen-in condition, or Alfvén theorem [63], in a small region within the current sheet, which is usually referred to as the diffusion region. The theorem states that "in a fluid with infinite electric conductivity, magnetic field lines are frozen into the fluid and have to move along with it". We can summarize the theorem, using the Magne-

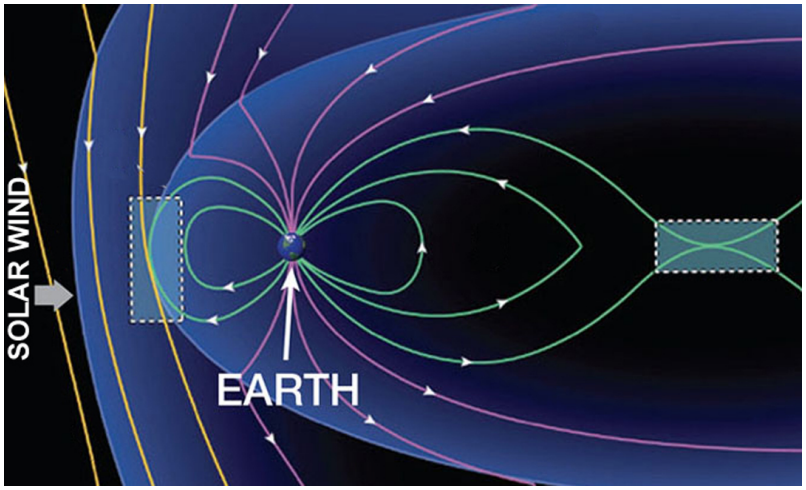

Figure 5.3: Illustration of Earth's magnetic field with the two MMS areas of study outlined. Credit: NASA

.

tohydrodynamic (MHD) theory, with the following equation

$$\frac{d\Phi}{dt} = -\int_S \nabla \times (\mathbf{E} + \mathbf{v} \times \mathbf{B}) \cdot d\mathbf{S} \tag{5.1}$$

where Φ is the magnetic flux through a surface $\mathbf{S}$ changing in time t. The surface moves with a velocity $\mathbf{v}$, while $\mathbf{E}$ and $\mathbf{B}$ are the electric and magnetic fields. From Ohm's law we have $\mathbf{E} + \mathbf{v} \times \mathbf{B} = \eta \mathbf{J}$, where η is the resistivity and $\mathbf{J}$ is the current density. For a perfectly conductive plasma $\eta = 0$, therefore the right hand side of this equation is zero. Under such condition, the magnetic flux is conserved and the magnetic field lines must move with the plasma, meaning that the frozen-in condition holds. Yet, due to microphysical plasma processes, this condition can be locally violated in the diffusion region so that adjacent magnetic field lines can change their connectivity, leading to a re-arrangement of the magnetic field. Such microphysical processes are able to produce a parallel electric field such that $\mathbf{E}+\mathbf{v}\times\mathbf{B} \neq 0$. The violation of the frozen-in condition and the onset of reconnection eventually lead to magnetic energy being dissipated and transferred to energy of charged particles in the form of local heating, bulk acceleration and non-thermal particle acceleration. The rate at which magnetic reconnection occurs is the rate of change of the magnetic field flux. A schematic view of the filed line configuration before and after magnetic reconnection is shown in Figure 5.4. A first model attempting to describe the process of reconnection is the Sweet-Parker model. The main feature of this model is that

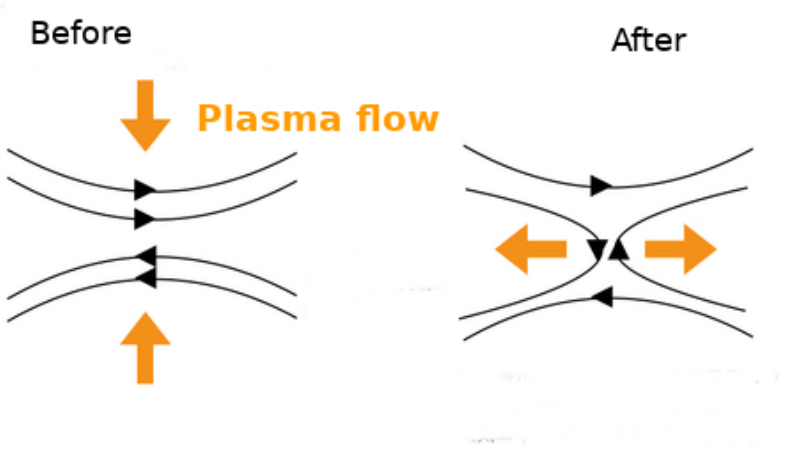

Figure 5.4: Schematic of magnetic field lines before (left) and after (right) magnetic reconnection.

reconnection takes place in a thin diffusion region of thickness 2δ and length $2L$, as shown by the sketch in Figure 5.5. The plasma outflow is along the horizontal x axis. In this configuration, four distinct regions of the plasma are formed: two inflow and two outflow regions (grey arrows in Figure 5.5), separated by the diffusion region (red area in Figure 5.5) which is close to the separatrix. One issue of the Sweet-Parker model is that the reconnection rate is too slow to account, for instance, for the observations of solar flares. Other more sofhisticated models have been developed in time. Here we give only a simple idea of the magnetic reconnection process, a review of some more realistic model and a more detailed presentation of the Sweet-Parker model can be found in [64].

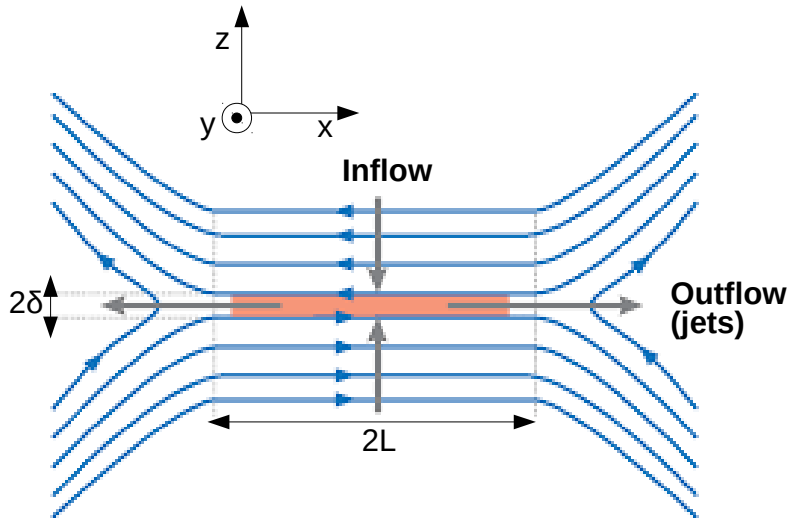

Figure 5.5: Sweet-Parker model of magnetic reconnection in the reconnection plane xz. Reconnection takes place in the red shaded region (diffusion region), where there is a localized resistivity. The reconnecting magnetic field (horizontal axis x) is antiparallel on either side of the current sheet and vanishes in the center. The normal to the current sheet is along the vertical axis z. Grey arrows denote the inflow and outflow of plasma. Credit : [64].

Chapter 6

Observations of ion acceleration in the magnetotail

Understanding the conversion of magnetic energy into accelerated charged particles is a long-standing problem in astrophysics. The fundamental process of magnetic reconnection is known to transfer a significant fraction of the stored magnetic energy into heated plasma and accelerated particles, both electrons and ions. Whatever the geometry, reconnection is a process common to most of the spatial and temporal scales in astrophysics. Both numerical simulations [65, 66, 67] and in situ observations [13, 14, 15] clearly indicate that only a few percent of particles are accelerated in the vicinity of the reconnection site, while most of the acceleration occurs away from the reconnection site through processes induced by reconnection. An important example is the acceleration occurring around reconnection jet fronts.

6.1 Characteristics of the plasma jet fronts

When the magnetic reconnection occurs, magnetic energy is converted into heated plasma which propagates in the outflow regions. The plasma jet fronts, also called reconnection jet fronts or dipolarization fronts, are boundaries separating hot, fast plasma jets, from colder ambient plasma almost at rest. Figure 6.1 shows an example of a plasma jet front observed by the spacecraft of the Time History of Events and Macroscale Interactions during Substorms (THEMIS) mission [75] reported in [74]. There are many features to recognize the passage of a plasma jet front. In correspondence with the second vertical dashed line in Figure 6.1, for example, we observe the strong increase of the normal component of the magnetic field B_z preceded by a magnetic dip, or B_z decrease (between the vertical lines). It is important

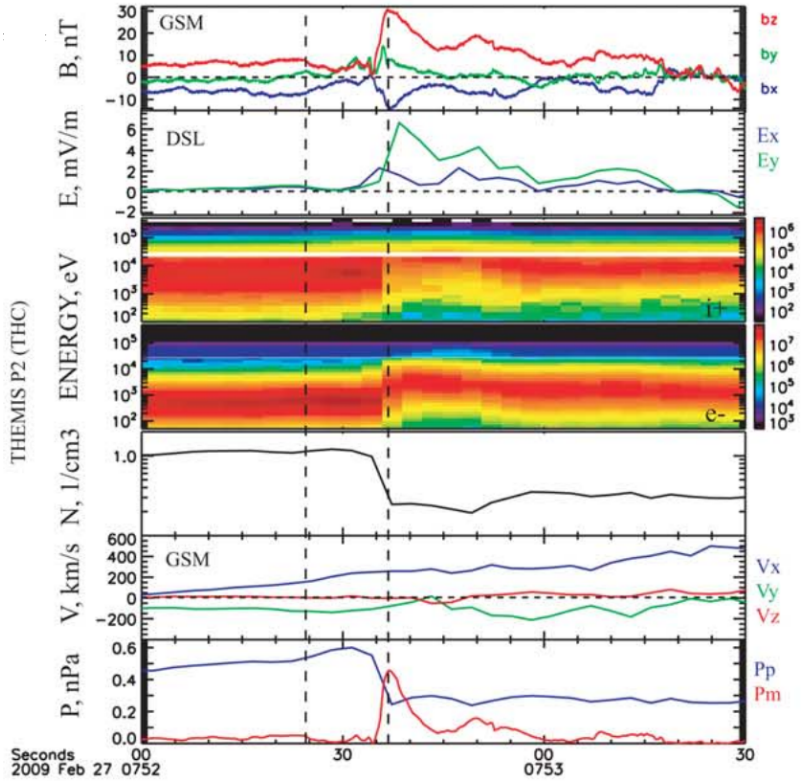

Figure 6.1: Plasma jet front observed by THEMIS on February 29, 2009. Credit:[74].

to note that after tens of second B_z is similar to what observed before the jet arrival. This feature distinguishes between the plasma jet front from the dipolarization events; for the latter the value of B_z remains higher after the strong enhancement. The dipolarization event is a global reconfiguration of the dipole magnetic field while plasma jet fronts are more "transient" events. Other signatures, in correspondence with the B_z ramp, are the increase of the electric field components, energetic ions and electrons together with the density decreases representing the passage from the colder ambient plasma to the hotter, and with lower density, reconnected plasma observed inside the jet. Also, we observe an increase in the ion velocity, and the balance between magnetic and kinetic pressure, indicating that the jet fronts are an example of tangential discontinuities. Observations [15] and simulations [76] suggest that multiple jet fronts are signatures of unsteady reconnection and the mechanism of generation of energetic particles at plasma jets have extensively been studied, (e.g., [77, 78, 66, 79, 80, 81, 82]), although many details are not fully understood. Both Fermi and betatron electron acceleration at

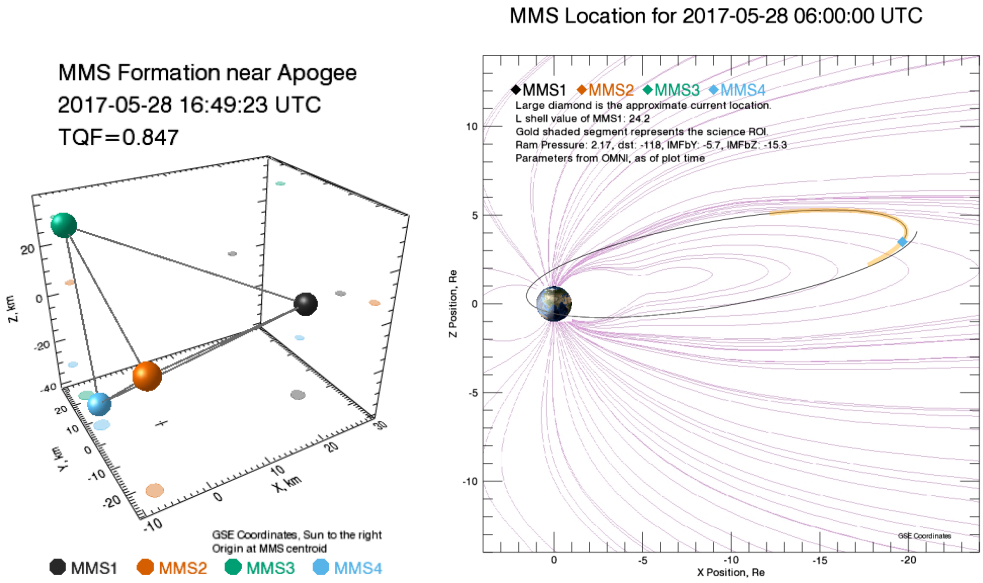

Figure 6.2: Spacecraft configuration (left side) and position (right side) in the (x, z) plane.

jet fronts have been recently shown through in situ measurements in the terrestrial magnetotail [14, 15]. Yet, in situ observations for ion acceleration in such a scenario are still lacking. In this Chapter, by using recent MMS observations, we will study the acceleration of protons and heavy ions due to different mechanism ahead the front, and between two consecutive plasma jet fronts.

6.2 MMS event overview

During the Phase 2b, started in May 2017, the MMS mission explored the Earth's magnetotail, the apogee was of about 25 R_E with the aim to observe the region where magnetic reconnection frequently occurs. During this phase, the four satellites were in a tetrahedron-like formation with an inter-spacecraft separation of 20 km. Here we study an event observed by MMS on 28 May 2017 between 06:44:40 and 06:46:40 UT. The position of the spacecraft at the beginning of the event was (-20, -12, -2) R_E in the Geocentric solar magnetospheric (GSM) coordinate system, a little off from the equatorial plane in the post-midnight region. Figure 6.2 shows the spacecraft configuration (left side) and the spacecraft trajectory in the (x, z) plane (right side), where the magnetic field line (purple lines) are obtained from the Tsyganenko model [83].

Figure 6.3 shows MMS observations averaged among the four spacecraft. It is reasonable to use four-probe averaged data since the separation between the four satellites is much smaller than the typical ion scale in the magnetotail, that is of $\rho_p \sim 500$ km for protons, where ρ_p is the proton gyroradius. All the data shown in this chapter are in burst mode, i.e., with the highest time resolution for each instrument. Figure 6.3 (a) and (b) show the profiles of the three components of the magnetic and electric fields (x, y, and z represented with black, blue, and red lines respectively), measured by the Fluxgate Magnetometers (FGM) [58], with sampling of 128 Hz, and the Electric field Double Probes (EDP) [57, 60, 59], with sampling of 8192 Hz. In panel (a) the total magnetic field is also shown (green line). At around 06:44:40 UT, all the components of the magnetic field are close to zero, suggesting that the spacecraft was in the inner current sheet (CS). At 06:45:19 UT, a strong enhancement in the B_z profile is observed, with the magnetic field increasing from zero to $\sim$16 nT in less then 2.5 seconds, and preceded by a magnetic dip, as is typical for dipolarization fronts [84]. The B_z ramp is accompanied by intense fluctuations of the electric field, in particular E_y reaches $\sim$ 17 mV/m. In the region of strong B_z, the B_x magnetic field component is negative, so the spacecraft are southern of the CS. At 06:45:33 UT both the magnetic and the electric fields start to substantially decrease, and after $\sim$ 20 s the electric field components begin again to fluctuate largely, while the B_x is positive indicating that the spacecraft crossed the CS. Therefore, it is possible to distinguish three regions: the two before 06:45:34 UT and after 06:45:50 UT enhanced by shaded area in Figure 6.3, are characterized by strong E_y fluctuations and large B_z, and the one in between characterized by weaker electric fluctuations. Similar profiles of B_z and E_y fields have been observed in the full-particle simulations with open boundaries by [76] where an unusual type of transient reconnection was investigated and where the dissipation at the jets was dominated by ions. In Figure 6.4 the B_z and E_y profiles from MMS observation (upper panel) and numerical simulation (bottom panel) are shown. Looking at the panel (a) in the bottom side of the Figure 6.4, we can observe that for positive values of x/d_i, that in [76] corresponds to the earthward outflow region, the profile of the magnetic field is similar to the one observed by MMS. In particular there is a typical "V" shape between the region of strong magnetic field. At the same time, by looking at the electric field profiles we see that it follows the magnetic field increasing when B_z is stronger and decreasing in between. The topology observed in [76] suggests that the observed regions of very strong B_z and E_y fields are like sharp fronts propagating with the Alfvén speed. A schematic cartoon of the possible scenario is shown in Figure 6.5. The scenario with two consecutive jets is also in agreement with the other particle data described

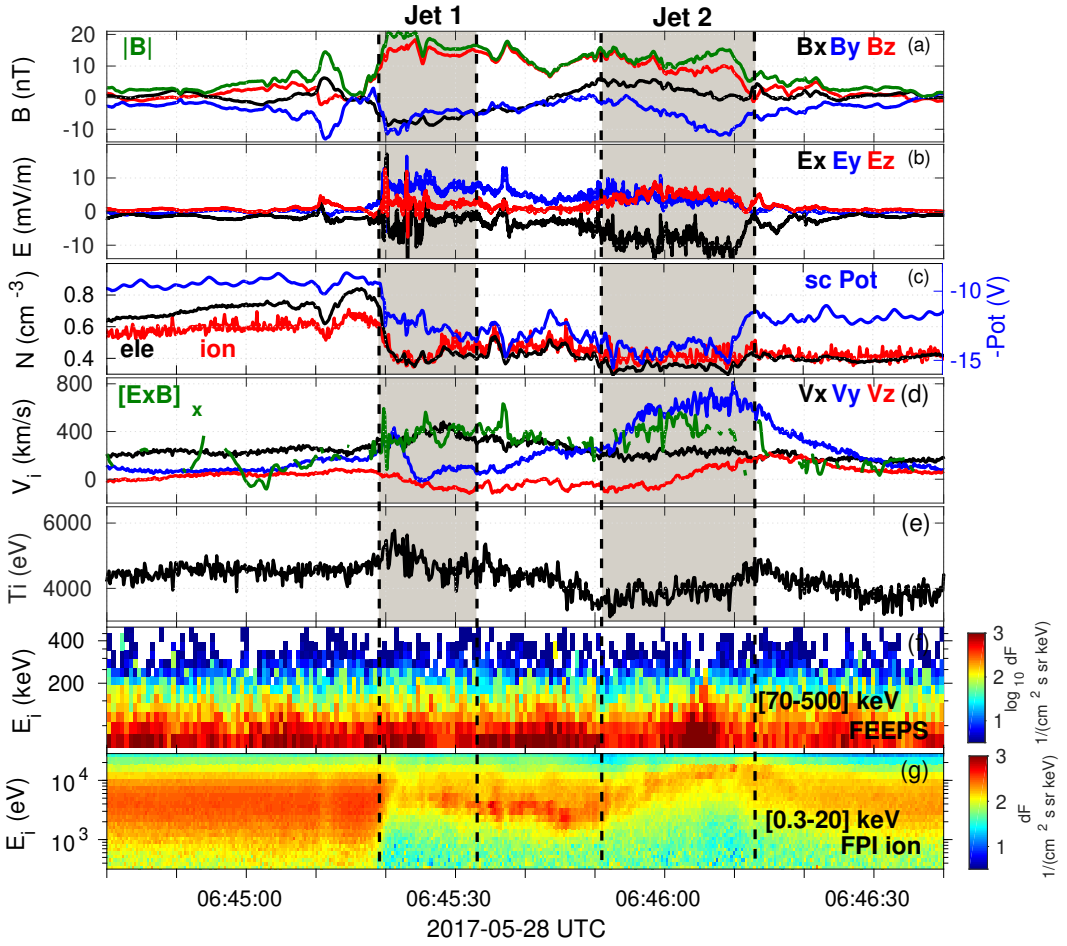

Figure 6.3: MMS observations on 28 May 2017 between 06:44:40 and 06:46:40 UTC. Panels show the profiles of magnetic (a) and electric field (b) components (x, y, and z represented with black, blue and red lines respectively, green line in panel (a) represents the total magnetic field), (c) ion and electron density (red and black lines) together with the spacecraft potential (blue line), (d) ion velocity components together with the $\mathbf{E}\times\mathbf{B}/B^2$ velocity along x direction (green line) smoothed on 0.9 s and computed only for $\mathbf{B} > 0.3nT$, (e) ion temperature, (f) ion energy spectrogram between [70-500] keV and (g) [0.3-20] keV. The two pairs of vertical dashed lines represent the passage of the two consecutive plasma jet fronts. All the data are in the GSM coordinate system and in burst mode.

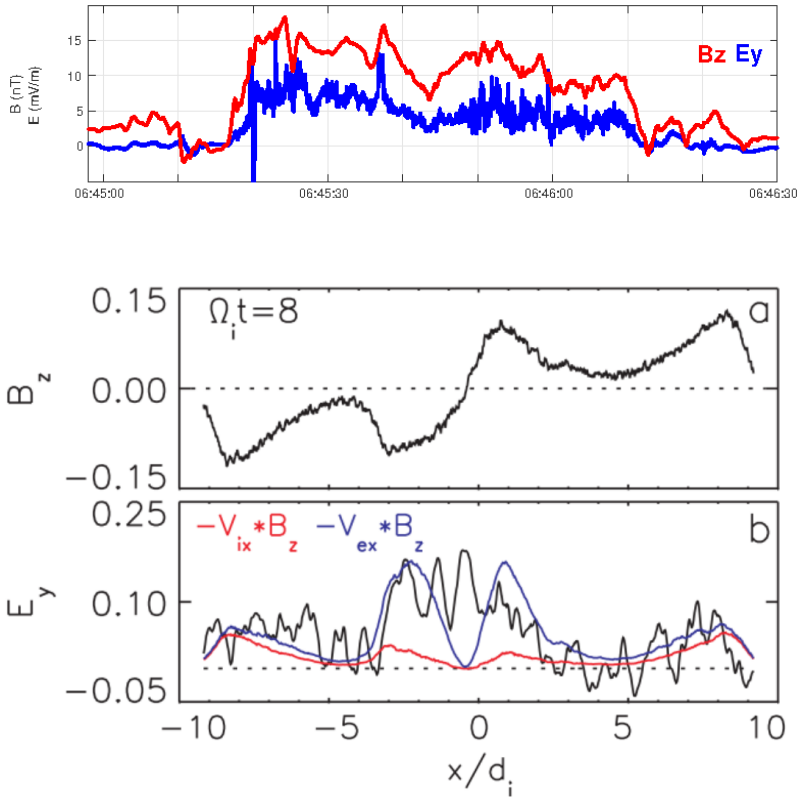

Figure 6.4: Magnetic field B_z and electric field E_y measured by MMS (upper panel), and obtained by numeric simulations in [76] (bottom panel).

in the following.

The shadowed regions in Figure 6.3 represent the first and second jet fronts between 06:45:19-06:45:33 UT and 06:45:51-06:46:13 UT, respectively. The ion moments shown in Figure 6.3 are obtained from the FPI instrument [61], which makes measurements in the energy range [0.01-30] keV with a time resolution of 0.15 s, hence ions with larger energies are not taken into account for the computation of moments. Figure 6.3(c) shows the density profiles for ions and electrons, together with the negative of the spacecraft potential. We observe a density gradient in correspondence of the first and last dashed lines, with a density decrease of about 50% respect to the value observed in the plasma sheet, determining the boundary between the denser ambient plasma and the reconnected plasma inside the jets [85]. Also, we observe a slightly higher density between the shaded regions. Panel (d) shows the x, y, and z components of the ion velocity (black, blue and red lines respectively) and the $\mathbf{E}\times\mathbf{B}/B^2$ velocity along the x direction, evaluated considering $|\mathbf{B}| > 0.3$ nT. The latter, has two peaks in correspondence of the jets. For the first jet, V_x is

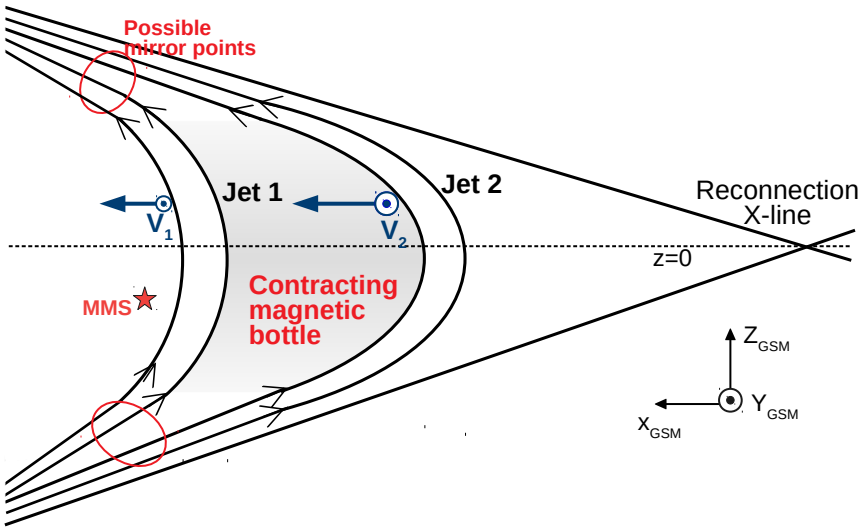

Figure 6.5: Schematic showing the two jets observed by MMS in the terrestrial magnetotail. The jet interaction forms a contracting magnetic bottle with the possible mirror points along the flux-tubes.

larger, while for the second jet the V_y dominates, similarly to what observed by [85] in the case of multiple jet fronts. In a classical scenario we should observe only an earthward plasma flow, i.e., along x, corresponding to the direction of jet propagation [74, 84]. The first jet may represent an obstacle in the reference frame of the second jet, thus the plasma encountering the first jet may be deflected along the y direction, as also suggested by the global simulations by [86]. Furthermore, panel (e) shows a temperature gradient in correspondence of both jets. In panel (f) the ion energy spectrogram between [0.3-20] keV detected by FPI instruments is shown. While panel (g) shows the ion energy spectrograms detected by the Fly's Eye Energetic Particle Spectrometer (FEEPS) [24], which measures energetic ions in the range [70-500] keV with a resolution of 0.3 s. At the beginning of the event we observe the ambient plasma, which is colder with most of the population detected by FPI. In correspondence with the two jets (shaded regions) we observe hotter plasma, which is mainly detected by FEEPS at energies ~ 100 keV, while the count level for FPI is low. For these reasons, the moments from FPI are not always fully representative in jet regions, as suggested also by the discrepancy between the particle density measured by FPI and that obtained from the spacecraft potential, as shown in Figure 6.3(c). In the region between the jets, where $B_z \sim |\mathbf{B}|$ has a local minimum, the plasma is denser in correspondence with lower energies respect to the plasma in the jets and it is more similar to plasmasheet. However, the difference in

density is not large and it cannot be excluded that this plasma is actually a mixture of ambient and reconnected plasma. Furthermore, we consider that the differences between the $\mathbf{E} \times \mathbf{B}/B^2$ velocity and that measured by FPI-DIS in the reconnection jets are due to the fact that part of the thermal plasma in the jets lies beyond the FPI energy range. All these properties support the interpretation that MMS observes a different plasma region in between the jets where $|\mathbf{B}|$ has a local minimum, in agreement with magnetic and electric field observations discussed above. We performed the standard timing analysis (see [87]) in order to evaluate the propagation speed of each front. Performing the analysis at the B_z ramp, at 06:45:17 UT, we obtained a jet's velocity of ~ 330 km/s mainly along the x direction. Considering that the duration of the ramp is $\Delta t \sim 2.5$ s, we can estimate the thickness of the front, that results to be $\delta_{F1} \sim 900$ km (i.e., $\sim 1.8\ \rho_p$). The timing analysis performed at the ending ramp of the second jet, at 06:46:12 UT, returned a propagation speed of ~ 560 km/s mainly along x, that is comparable to the local Alfvén speed $V_A \sim 600$ km/s, in agreement with the numerical results by [76]. The duration of the ramp for the second front is $\Delta t \sim 3$ s, therefore we obtain the front thickness $\delta_{F2} \sim 1600$ km which corresponds to $\sim 3\ \rho_p$.

We note that, a scenario similar to the one suggested in Figure 6.5, has been found in the magnetohydrodynamic (MHD) simulations of magnetic reconnection discussed in [67] and shown in Figure 6.6. We can observe the magnetic field line configurations at different simulation times before, during and after the reconnection. In particular, at time consecutive to the reconnection, as for $t = 132$ in the Figure 6.6, we can notice how the magnetic field lines deform and get closer to each other, suggesting the compression of the plasma in between.

Two consecutive earthward propagating jet fronts were observed by the Cluster mission and reported by [15]. In that work, the energetic electrons were found to be accelerated by the quasi-adiabatic mechanisms of betatron and Fermi acceleration in the outflow jets, while it was not possible to study ion acceleration. Now, using MMS data, we can investigate the mechanisms that accelerate the ions in a similar scenario.

Figure 6.7 reports the ion distribution functions in different regions. Panel (a) shows the profiles of the B_z magnetic field (red line), total magnetic field (green line) and E_y electric field (blue line). We can see that $|\mathbf{B}|$ and B_z almost match each other, showing that the other magnetic field components, reported in panel (b), are smaller than B_z. The dashed vertical lines ($[\beta]$ and $[\delta]$) in Figure 6.7, denote the regions where the ion distribution functions are studied. The cut $[\beta]$ is taken in the plasma sheet before the front passing, where the values of the total magnetic field is $|\mathbf{B}| \sim 3$ nT and $B_x \sim 0$ nT (see Figure 6.7 (a) and (b)). Panels (c) and (d) show FPI ion distribution

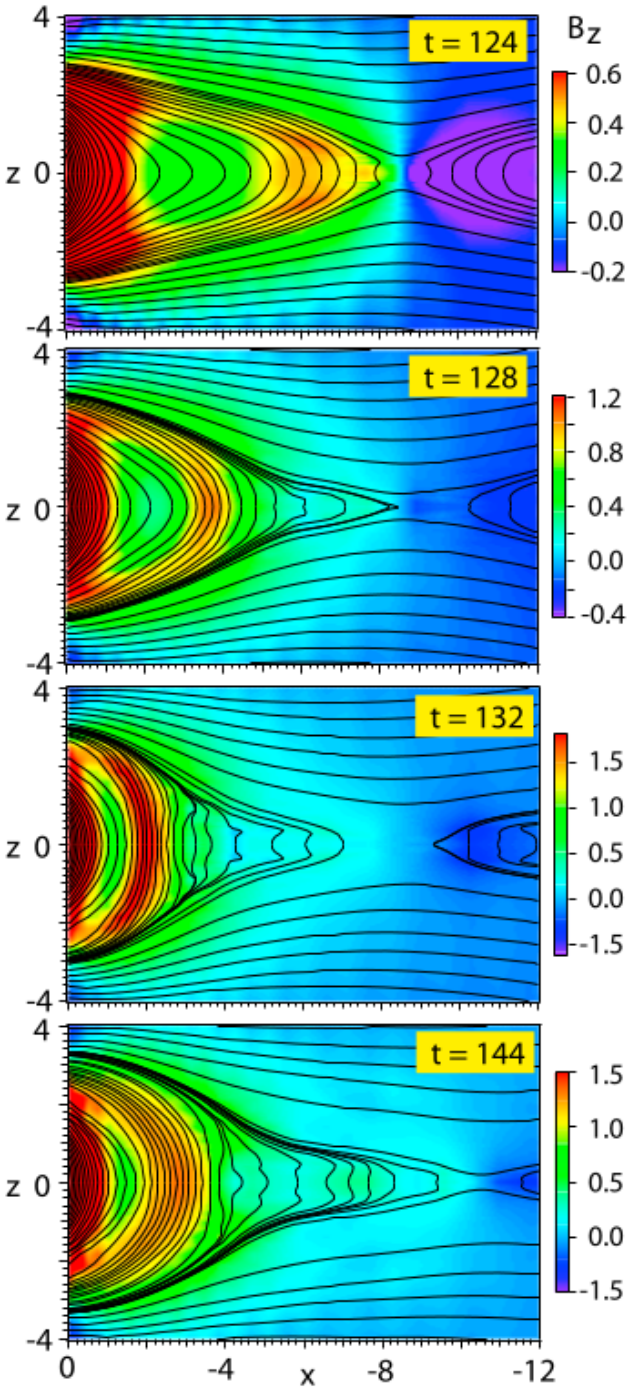

Figure 6.6: Magnetic field component B_z (color) and magnetic field lines in the x, z plane at different times of the MHD simulation. Credit: [67]

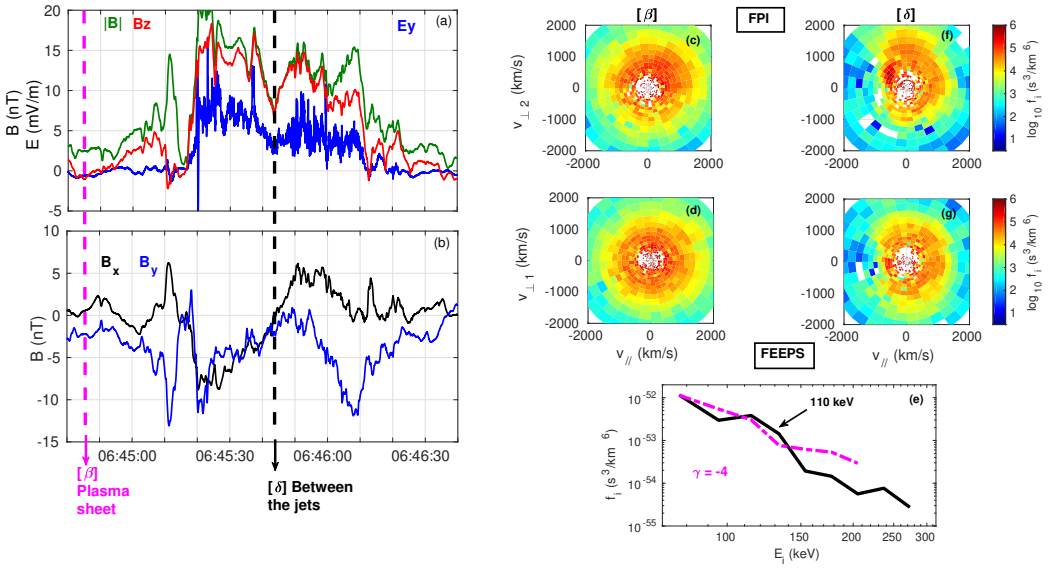

Figure 6.7: Panel (a) reports the profiles of the B_z magnetic field (red line), total magnetic field (green line) and E_y electric field (blue line). Panel (b) shows the profiles of the x and y components of the magnetic field (black and blue lines respectively). Right panels show the ion distribution functions, detected by FPI, in the $(V_{\perp,2}, V_{//})$ plane ((c) and (f)) and $(V_{\perp,1}, V_{//})$ plane ((d) and (g)) at the cut $[\beta]$ (left) and $[\delta]$ (right). Bottom panel shows the ion distribution as a function of energy detected by FEEPS for the cuts $[\beta]$ (magenta line) and $[\delta]$ (black line). Ion distributions are measured by the instruments at the same instants of time.

functions in the $(v_{\perp,2}, v_{//})$ plane, and $(v_{\perp,1}, v_{//})$ plane, where $\mathbf{v}_{//}$ is the ion velocity along the local magnetic field, $\mathbf{v}_{\perp,1} = \mathbf{v} \times \mathbf{b}$, and $\mathbf{v}_{\perp,2} = \mathbf{v} \times \mathbf{v}_{\perp,1}$, and where $\mathbf{v} = \mathbf{V}_i/|\mathbf{V}_i|$ and $\mathbf{b} = \mathbf{B}/|\mathbf{B}|$. We can see that the distribution is almost isotropic. We can compare these distributions with the one obtained in the region [δ] between the two jets. Here we are again in the center of the current sheet since $B_x \sim 0$ nT. We can notice that the ion distribution function detected by FPI is less isotropic (see panels (f) and (g)), with most of the ions distributed along the perpendicular direction. Panel (e) displays the ion spectra as a function of energy detected by FEEPS in the region [β] (magenta line) and [δ] (black line). By fitting the spectra measured in [β] with a power law $f(E_i) \propto E_i^{\gamma}$, we can evaluate the spectral index that results to be γ = - 4, similar to those reported in [19] for ions in the Earth's plasma sheet. It is worth to notice that in [δ] the spectra is steeper than in [β], with a flux enhancement at $\sim$ 110 keV. Also, ions reach larger energies up to 300 keV. Therefore, in the region between the two jets ions are more energetic (black line in Figure 6.7(e)) and anisotropic (Figure 6.7 (f),(g)) respect to the ambient plasma. This suggests that in the region [δ] a process that confines perpendicularly the thermal part of the ion distribution and, at the same time, energizes the ions is ongoing. However, the two profiles in Figure 6.7(e) are similar, indicating that only a small fraction of the ion population is energized at higher energies, in agreement with the results reported for example in [68].

6.3 Ion acceleration in the contracting magnetic bottle

In order to understand what is the acceleration mechanism acting in the region between the two jets, we study the pitch angle distributions (PADs). Figure 6.10 shows the PADs in three energy ranges: [205-500] keV (panel (a)), [70-205] keV (panel (b)), and [10-20] keV (panel (c)). The energy ranges were chosen in order to have a sufficiently high level of counts. Figure 6.10 (d) displays the profiles of the magnetic field B_z and of the electric field E_y. First, we can see that the PADs have different features depending on the energy range. In particular, between the vertical dashed lines, representing the region between the jets, the pitch angle (PA) mainly corresponds to perpendicular velocities for energies of 10-20 keV, while the perpendicular population is almost absent for higher energies. At the same time, the distribution for high and low value of the PAs increases at higher energies.

As discussed in the previous section, the behavior of the magnetic field

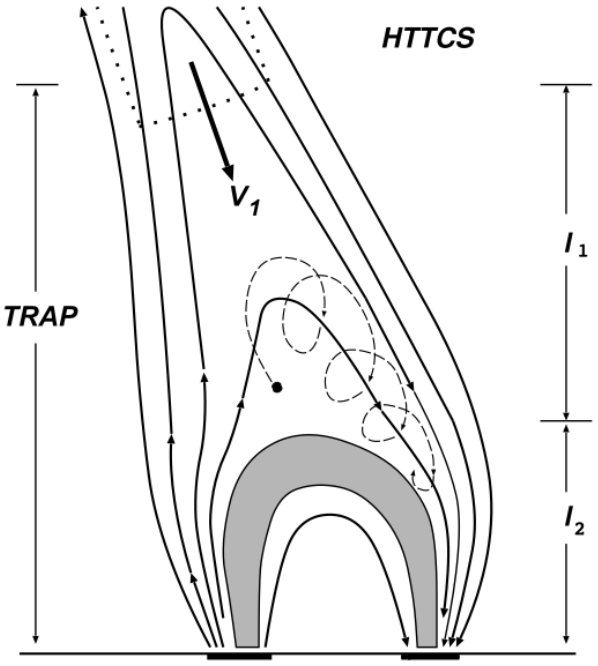

Figure 6.8: Schematic models of collapsing magnetic field lines occurring in models of magnetic reconnection. HTTCS denotes "high temperature turbulent current sheet". Credit: [69]

suggests the formation of a magnetic bottle between the two jet fronts. We can compare this scenario with the one for the solar magnetic trap [69]. In that model, the particles are accelerated at the jets forming in the reconnection outflow region during solar flares. The plasma jet, confined on the newly reconnected field lines, moves downwards until it encounters the underlying magnetic loop [69]. As a result of its motion the length of the magnetic trap decreases accelerating the trapped particles via a first-order Fermi process[70, 71, 72, 73]. The particle kinetic energy increases in the magnetic trap until particles fall into the loss cone. Further, as a result of the jet braking, particles in such magnetic field configurations may be trapped not only between the loop's foot points, but also between secondary mirroring points along the flux tube, as shown by [88]. A scheme of the solar magnetic trap model is shown in Figure 6.8.

Similarly to the model of the solar magnetic trap, we can argue that ions from the plasma distribution between the two jets can be considered to be magnetized, and are trapped inside the bottle; as the bottle contracts due to the different front propagation speeds, the ions are accelerated along the

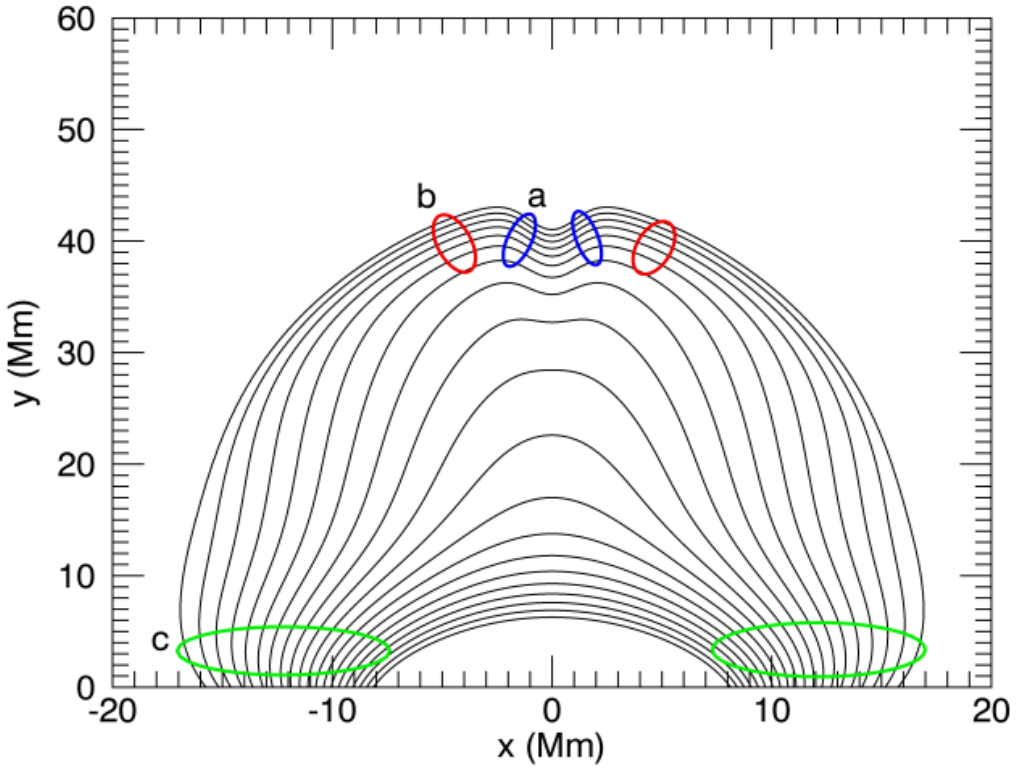

Figure 6.9: Approximate locations of possible mirror points for particles trapped in the model are circled. The test particle orbit initial conditions determine in which region the particle is mirrored. Black lines are magnetic field lines. Regions a and b may contain mirror points because of the higher magnetic field strength associated with the braking jet. Mirror points located in the region c occur due to the stronger magnetic field at the solar surface. Credit:[88].

parallel direction, given that $J = \oint p_{\|} dl = \text{const}$. We also suggest that the bottle has the mirror points along the magnetic flux tube, and not just between the foot points, as also shown by [88]. Possible mirror points are shown in the sketch in Figure 6.5. We also report in Figure 6.9 the possible mirror points as obtained in the numerical simulations by [88].

We can estimate the loss cone angle α as

$$\alpha = \sin^{-1}\left(\sqrt{\frac{\mid B \mid}{B_{max}}}\right) \tag{6.1}$$

where $B_{max} = 21$ nT is the maximum value of the magnetic field magnitude in the whole interval and is comparable to the lobe magnetic field at about

$20R_E$ downtail, therefore it can be considered representative of the magnetic field in the mirror points; and $|\mathbf{B}|$ is value of the local magnetic field magnitude. The solid black lines in Figure 6.10 represent the loss cone angles for α and $180 - \alpha$. The ions having PA between the black lines are locally trapped in the bottle, while if the PA is below and above the black lines the ions are not-trapped. This is in agreement with the observations showing trapped ions with perpendicular PAD for lower energies (see Figure 6.10(c)), while for higher energies ions have "more parallel" PAD and, entering the loss cone, they escape from the bottle (see Figure 6.10 (a) and (b)). Indeed, the contracting magnetic bottle causes an increase in the parallel velocity, similar to the effects of a collapsing magnetic trap, so that very few particles with PA $\sim 90°$ are observed. A similar mechanism was suggested by [89] to explain the observation of energetic electrons in the solar corona. It is possible to estimate the length of the magnetic bottle along z as $L = V_z \times \Delta t$. The velocity of the structure along z is obtained performing the timing analysis for the CS crossing. We obtain $V_z \simeq 350$ km/s. The interval between the two jets is found to be $\Delta t = 20$ s, similarly to [85, 15]. Therefore, we obtain $L \simeq 7000$ km which is comparable with th typical CS thickness [90]. With the increase of energy ions are less magnetized, so that when the ion Larmor radius ρ_i is comparable or larger than L, they can escape the bottle. Using the condition $\rho_i > L$, we can estimate the minimum energy E_{esc} needed to escape from the magnetic bottle. We found that $E_{esc} \sim 108$ keV for protons and alpha particles. This can explain the peak at ~ 110 keV in the ion energy distribution in Figure 6.7 (e). This also agrees with the observations showing parallel PAD for energies above E_{esc}. In particular, in Figure 6.10 (a) and (b), a small portion of ions inside the black lines is still visible. This could be due to the fact that the instruments are measuring not only protons but also heavier ions, that are predominant above 150 keV in multiply charged state (as shown by [26, 27, 25]). For a fixed ion mass E_{esc} is proportional to q_i^2, where q_i is the ion charge. Therefore, the ions inside the black lines in Figure 6.10 (b) and (a) are probably multiply charged heavy ions still trapped inside the magnetic bottle. This event is rather rare, and for the first time we studied observations of PADs of energetic ions in the region between two consecutive jet fronts, with ions going from the thermal energy of about 5 keV to more than 100 keV. The observed jet fronts are reminiscent of the downward-moving reconnected field lines in collapsing magnetic traps during solar flares models, where strong particle acceleration occurs. Our observations in the terrestrial magnetotail provide in situ evidence of strong acceleration when a contracting magnetic bottle forms between consecutive jets produced by unsteady magnetic reconnection. This ion acceleration mechanism can have far-reaching implications for many astrophysical environments such as stel-

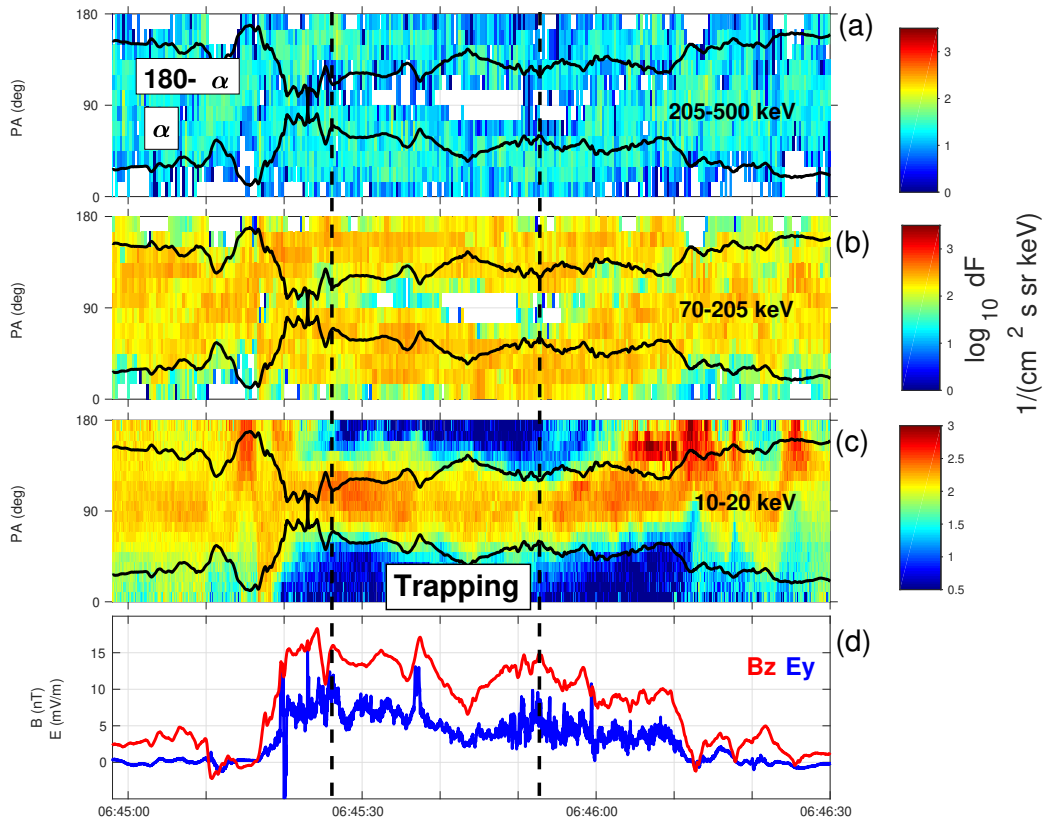

Figure 6.10: Ion pitch angle distributions in the energy range of [205-500] keV (a), [70-205] keV (b) and [10-20] keV (c). Black lines represent the local value of the trapping angles α and $180 - \alpha$. Panel (d) shows the profile of B_z (red line) and E_y (blue line).

lar coronae and winds, planetary magnetospheres, accretion disks and radio galaxies, where reconnection and jets are ubiquitous. These results are also discussed in [98].

6.4 Interaction of ions with the single jet front

Now we focus on the ion interaction with the first jet front boundary. From both observations and simulations, it is well known that plasma jet fronts are one of the main regions where high-energy ions and electrons are observed [91, 92]. For example, jet fronts in the Earth's magnetotail, during their earthward motion can compress the ambient plasma sheet, enhancing plasma pressure ahead of them [93, 94, 95]. In the kinetic framework, the ambient particles encountering and approaching the jet front, can be accelerated by the duskward electric field behind it, and reflected earthward after a half gyration around the enhanced B_z [78, 79, 96, 97, 31]. Some of the ambient ions may even be reflected multiple times at the front [99, 100, 80]. The accelerated and reflected ions could be observed in the upstream (with respect to the front) central plasma sheet as an additional population with earthward velocities superimposed over the ambient plasma. Furthermore, considering the implications of the B_z negative depletion ahead of the front in numerical simulations, [101] and then [102, 103] showed that ions can be stably trapped at the reconnection point, formed ahead of the front, and accelerated by the electric field associated with the front motion, similar to the surfatron acceleration. Moreover, the acceleration mechanism can be different if we consider different ion species. This is a resonant mechanism only qualitatively validated using in-situ observations.

Now we focus on the region of the first jet, between 06:44:40 and 06:45:40 UT. In this case we use one-probe data from MMS3, although observations are consistent among all the spacecraft. Figure 6.11 displays a partial overview of the event (upper side) and a zoom of the region of interest (bottom side). Panel (a) reports the B_z component of the magnetic field together with the y component of the electric field (red and blue lines respectively). We can see that, in correspondence of the magnetic ramp, the fluctuations of the electric field become very strong. Again, panel (b) displays the ion and electron density and the negative of the spacecraft potential. In panel (c) the perpendicular ion velocity (red line) and the $\mathbf{E} \times \mathbf{B}/B^2$ quantity (black line) along the x direction are shown. Both signals are smoothed for clarity. Following the black profile we can notice that the velocity increases in correspondence with the jet front. The same gradient is not clear in the red profile, due to the computation of the velocity moment being done

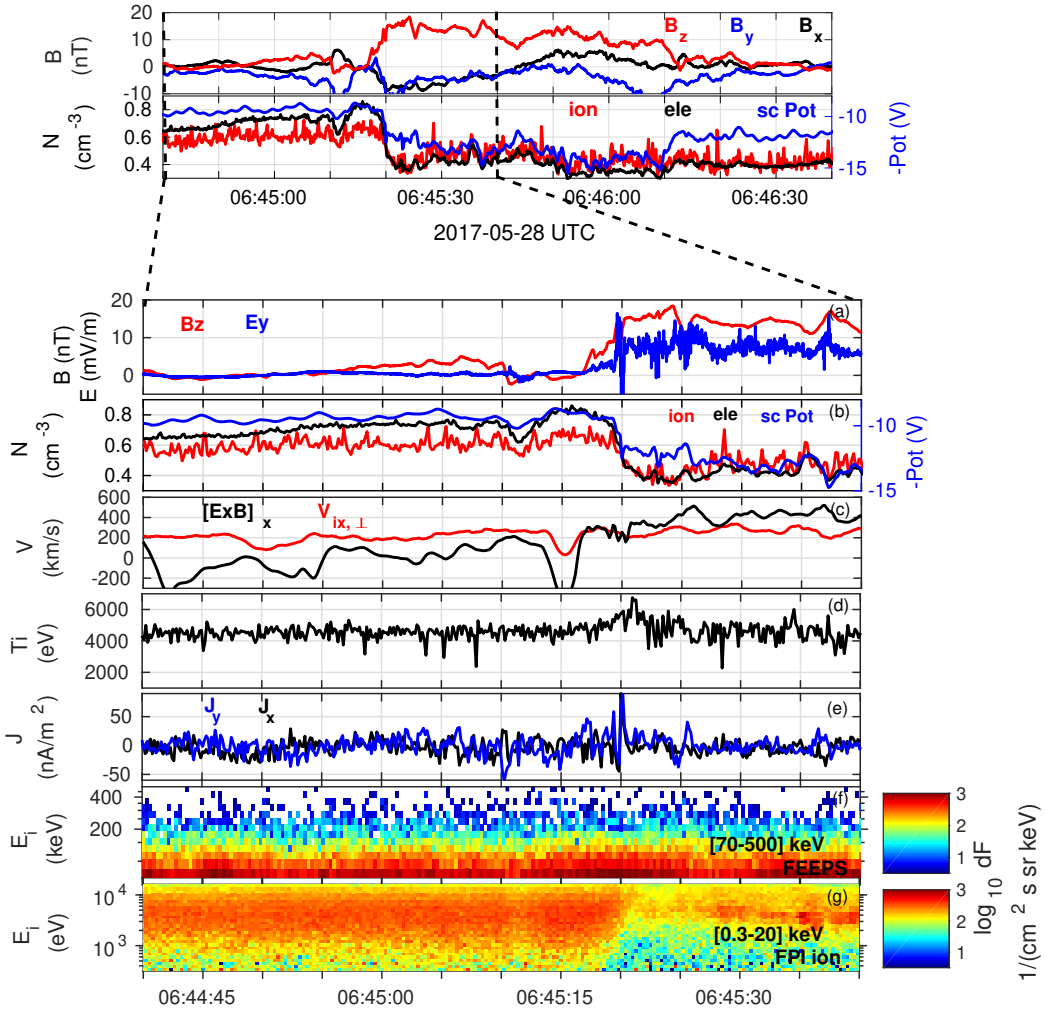

Figure 6.11: Upper panels: MMS3 observations on 28 May 2017 between 06:44:40 and 06:46:40 UT. The first panel shows the three components of the magnetic field B_x, B_y, and B_z (black, blue and red lines respectively). Second panel shows the ion and electron density (red and black lines) together with the spacecraft potential (blue line). Bottom panels: Zoom of the event between 06:44:40 and 06:45:40 UT. Panels show (a) the profiles of the z component of the magnetic field (red line) and the y component of the electric field (blue line), (b) ion and electron density together with the spacecraft potential, (c) perpendicular ion velocity (red line) and $\mathbf{E} \times \mathbf{B}/B^2$ quantity (black line) along the x direction, (d) ion temperature, (e) current density along the x (black line) and y (blue line) directions, (f) ion energy spectrogram between [70-500] keV and (g) [0.3-20] keV.

using only the thermal portion of ion population up to 30 keV. Also, the ion temperature (panel (d)) and current density increase simultaneously at the magnetic ramp. Here the current density is computed by using the FPI plasma moments. Finally, panels (f) and (g) show the energy spectrograms of ions, detected by FEEPS and FPI instruments, in the energy range between $[70-500]$ and $[0.3-20]$ keV, respectively. It is worth noticing the absence of ions in the thermal energy range (panel (g)) in correspondence of the plasma jet, while most of them are observed at higher energies (panel (f)). The low counts of thermal ions in this region are consistent with the small gradient of the ion moments at the same time. Also, we notice the presence of such energetic ions also before the magnetic ramp, in the region of the magnetic dip, suggesting that the ambient plasma can be accelerated in this region.

In Figure 6.12 we report the typical ion distribution functions in the plasma sheet (cut α) and in the region ahead of the front (cut β), where the magnetic dip is observed. The upper panels show (a) the total magnetic field $|\mathbf{B}|$ (black line) and the B_z profile (red line), together with the E_y component of the electric field (blue line). We notice that $|\mathbf{B}|$ and B_z are comparable, suggesting that the variations of the other components of the magnetic field are very small. In panels (b) and (c) the x and y components of the magnetic field and ion velocity (black and blue lines respectively) are shown. Further, the bottom side of Figure 6.12 displays the ion distribution functions measured by FPI in the $(v_{\perp,2}, v_{//})$ plane ((d) and (e)), and $(v_{\perp,1}, v_{//})$ plane ((g) and (f)), where $\mathbf{v}_{//}$ is the ion velocity along the local magnetic field, $\mathbf{v}_{\perp,1} = \mathbf{v} \times \mathbf{b}$, and $\mathbf{v}_{\perp,2} = \mathbf{v} \times \mathbf{v}_{\perp,1}$, with $\mathbf{v} = \mathbf{V}_i/|\mathbf{V}_i|$ and $\mathbf{b} = \mathbf{B}/|\mathbf{B}|$. Finally, panel (h) shows the distribution functions as a function of energy in the plasma sheet (magenta line) and in the region of the magnetic dip (black line). The distribution of the thermal ion population is almost isotropic, as shown in panels (d) and (e). Concerning the supra-thermal population, we estimated the spectral index γ by fitting the profile, represented by the magenta line in panel (h), with a power law $f_i(E_i) \propto E_i^{\gamma}$, and $\gamma = -4$ as discussed in previous section. In the region of the magnetic dip, the spacecraft was again in the plasma sheet since $B_x \simeq 0$ nT (see panel (b)), so that we are basically observing the same plasma of the cut α and we can make a comparison. The thermal distribution in the region β is less isotropic, in particular it is possible to observe larger population along the perpendicular direction $\mathbf{v}_{\perp,2}$, that correspond mainly to the y direction in GSM. This is in agreement with the increase of V_y and V_x observed in that region (panel (c)). If we compare the two profiles for the supra-thermal population in α and β (see panel (h)), we can see that there is a larger portion of ions with energies between [160-200] keV (black line) with respect to the one previously observed (magenta line), therefore there is a mechanism that produce energetic ions in this

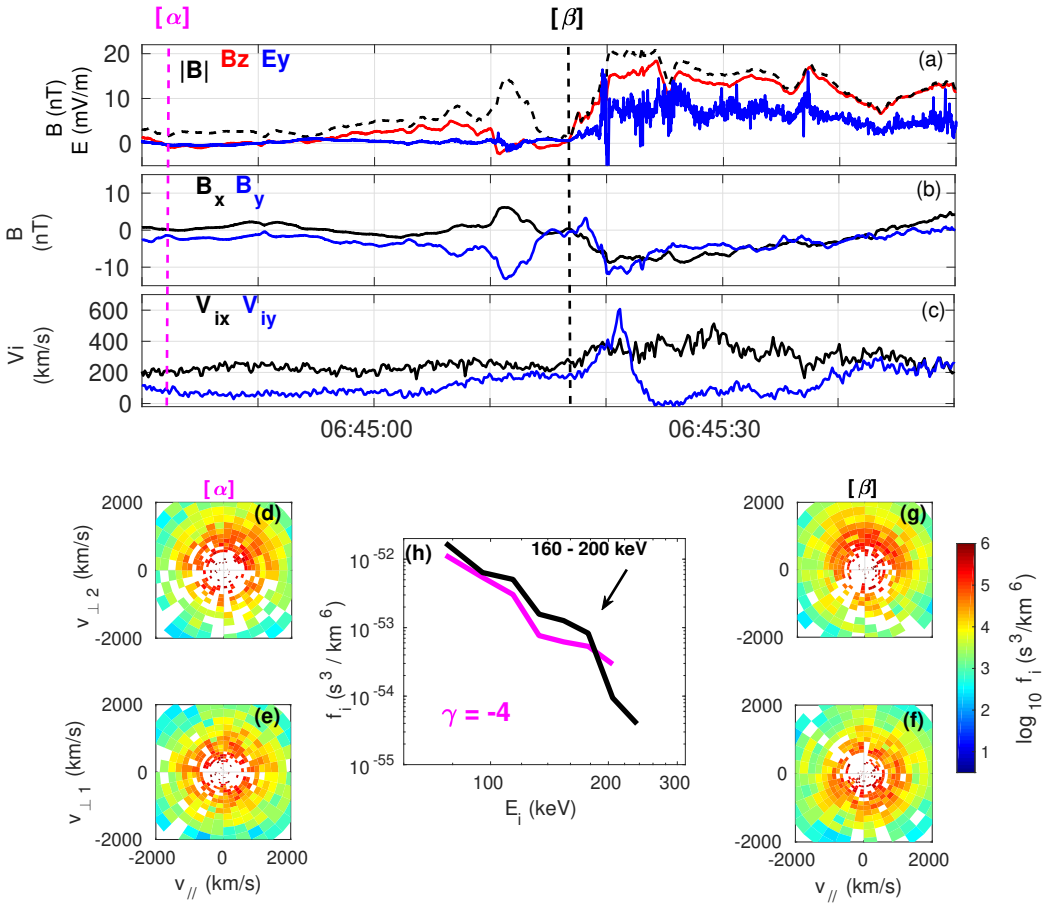

Figure 6.12: Panel (a) reports the profiles of the magnetic field B_z (red line), total magnetic field (black dashed line) and electric field E_y (blue line). Panels (b) and (c) show the profiles of the x and y components of the magnetic field and current density (black and blue lines respectively). Right panels show the ion distribution functions, detected by FPI, in the $(V_{\perp,2}, V_{//})$ plane ((c) and (f)), and $(V_{\perp,1}, V_{//})$ plane ((d) and (g)). Bottom right panels show the ion distribution as a function of energy detected by FEEPS ((e) and (h)). Ion distributions are measured by the instruments at the same instants of time.

region. The presence of the B_z dip before the magnetic ramp, together with the increase in V_x and V_y, are signatures of ion reflection at the plasma jet fronts and acceleration due to the large E_y electric field, as also suggested by both simulations and observations [78, 104, 79, 31, 105, 106, 80]. In the following section we suggest a somewhat different acceleration mechanism, previously observed only in numerical simulation, that possibly may better explain the observations.

6.5 Trapping and squeezing the valley ahead of the jet front

Figure 6.13 shows the energetic spectrograms for protons, helium and oxygen ions between [130-300] keV (panels (a)-(c)), measured by the Energetic Ion Spectrometer (EIS) with a resolution of 0.6 s. Panel (d) displays the spectrogram for the thermal ion population between [0.3-20] keV, while panel (d) shows the profiles of the B_z magnetic field (red line) and E_y electric field (blue line). Data in panels (a)-(c) are at sub-spin resolution so that, during each spin period of 20 s, the spacecraft is looking in the direction of the plasma jet and measuring the energetic ions. The dependence of the measurements on the spin period, corresponding to regions with higher and lower level of counts, is more visible for example in panel (c). Analyzing the spectrograms we can observe that the population inside the jet, around 06:45:30 UT, is hotter than the plasma sheet, observed around 06:44:40 UT. The plasma observed ahead of the jet, in correspondence of the magnetic dip between 06:45:10 and 06:45:15 UT, is similar to the one in the plasma sheet, but with larger population around 160 keV for protons and helium, and 200 keV for oxygen ions. These beams of energetic ions are highlighted using the black circles in Figure 6.13, and are consistent with the black profile observed in Figure 6.12 (h). The proton beam at 06:45:11 UT exactly coincides with the change of the B_z sign, due to the electric current carried by ion beams. The presence of the beams suggests that, in the region ahead of the jet, a mechanism is acting that accelerates to high energies only a part of the ions, and so that it is a resonant acceleration mechanism. Indeed, if the ions were simply reflected at the boundary and then accelerated by the dawn-dusk electric field, we would have observed a larger portion of energetic ions at energies proportional to four times the thermal energy [78, 104].

Recently, a model that support the resonant acceleration at plasma jet fronts, has been developed and numerically investigated by [101, 102, 103]. According to their studies, ions are performing Larmor orbits before the

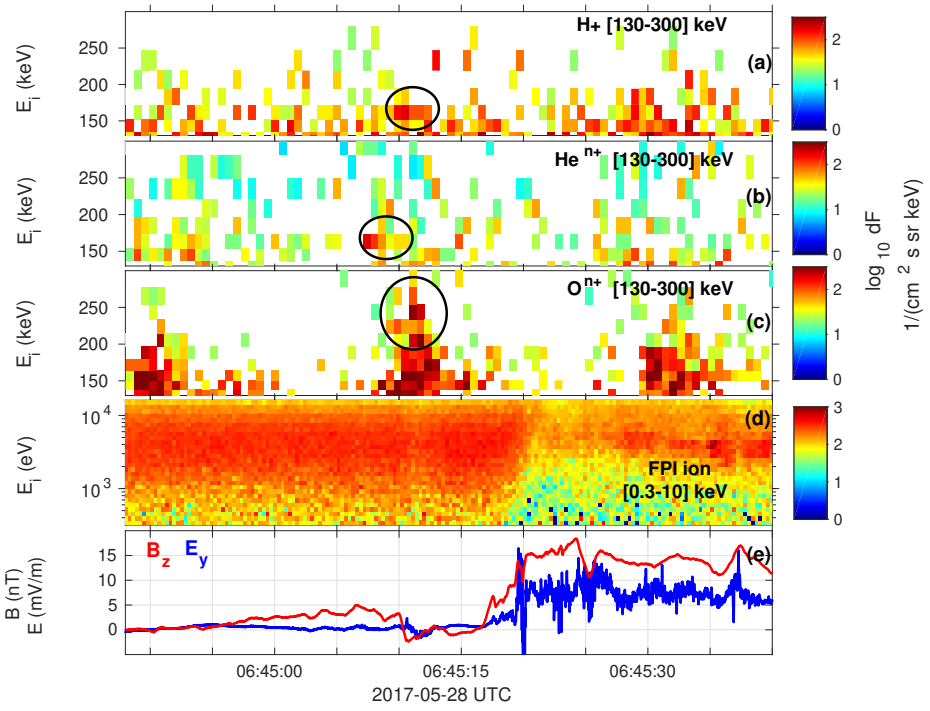

Figure 6.13: Differential energy flux for protons, helium and oxygen ions (panels (a), (b) and (c) respectively) measured by EIS between [130-300] keV. In panel (d) is shown the flux for thermal ion population between [0.3-20] keV. Last panel shows the profiles of the magnetic field B_z (red line) and electric field E_y (blue line).

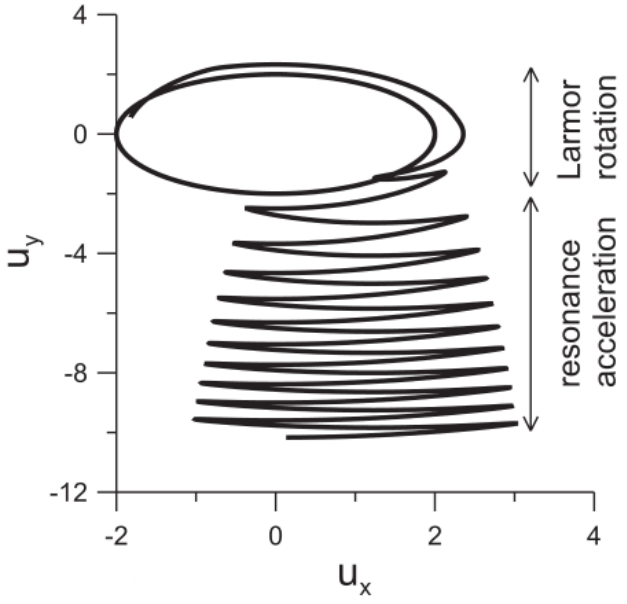

Figure 6.14: Simulated particle trajectory in velocity space. Credit: [101].

jet arrival, then they can interact with the approaching jet in a resonant manner if they satisfy the Cherenkov resonant condition in the velocity space, that is $V_{i,x} = V_\phi$, where $V_{i,x}$ is the ion velocity along x, and V_ϕ is the jet front propagation speed. If the resonant condition is satisfied, then ions are captured along the jet in the y direction and, since the jet propagates, are accelerated by the electric field E_y via the surfatron acceleration mechanism [107, 108, 109].

Figure 6.14 shows the particle trajectory in the velocity space as obtained in two-dimensional numerical simulations by [101]. The trajectory is composed by two different behaviours: initially the particle is performing Larmor orbit, then the jet arrives and the particle starts to be trapped in the region ahead of the front.

In particular, if the magnetic field B_z has a negative depletion ahead of the front and goes through zero in two points, a potential well forms between those two points, and the ions are stably trapped therein [102]. Figure 6.15 shows the effective potential of the particle motion ahead of the front obtained by three-dimensional simulations in [102]. Red vertical lines indicate the region where B_z change sign, i.e., the trapping points. We can observe the formation of a potential well ahead of the front which can easily lead to the particle trapping. The particle trapped in this region are "stably trapped", while without the negative B_z depletion, the ions are quasi-trapped and accelerated behind and ahead of the front by a mechanism more similar

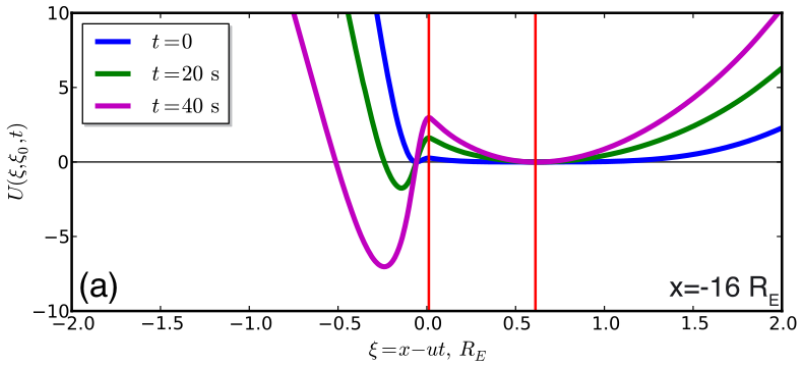

Figure 6.15: Simulated effective potential of particle motion along plasma jet fronts with a negative depletion of B_z, computed at different moments. Red vertical lined indicate the region where B_z change sign. Credit: [102].

to the diffusive shock acceleration [102, 103].

Figure 6.16 shows the mechanism of stable trapping for ions with energies of 280 keV (c), 140 keV (b) and 70 keV (e), as obtained by [103]. The mechanism works for all the energies and ions are well trapped inside the separatrix. Also, in Figure 6.17 is shown the trajectories for protons with initial energy of 50 keV. We can observe that the most of the energetic particles are trapped in the region ahead of the front.

In our observations the magnetic field B_z has a negative depletion ahead of the jet, passing through zero at 06:45:10 and 06:45:17 UT (see Figure 6.12 (a)), so ions are stably trapped in this region.

Figure 6.18 shows the distribution functions for protons, helium and oxygen ions (upper, middle, and bottom panel respectively) in the region of the plasma sheet (magenta lines), B_z dip (black lines), and plasma jet front (blue lines). In this case we used the data at spin resolution, so each line is a 20 s average of the data shown in Figure 6.13. Thus, the magenta profile describes the distributions between 06:44:32 and 06:44:52 UT, the black profile between 06:44:52 and 06:45:12 UT, and the blue profile between 06:45:12 and 06:45:32 UT. By comparing the three profiles it is clear that: the blue profile is strongly different from the magenta profile, while the magenta and black profiles have similar slope. Furthermore, comparing the profiles in the plasma sheet and in the magnetic dip, the formation of the ion beams at energies around 160 keV is visible for protons and helium, and larger than 200 keV, for oxygen ions, consistently with the spectrograms in Figure 6.13. By following the model in [101], we can estimate the size R_y of the jet front

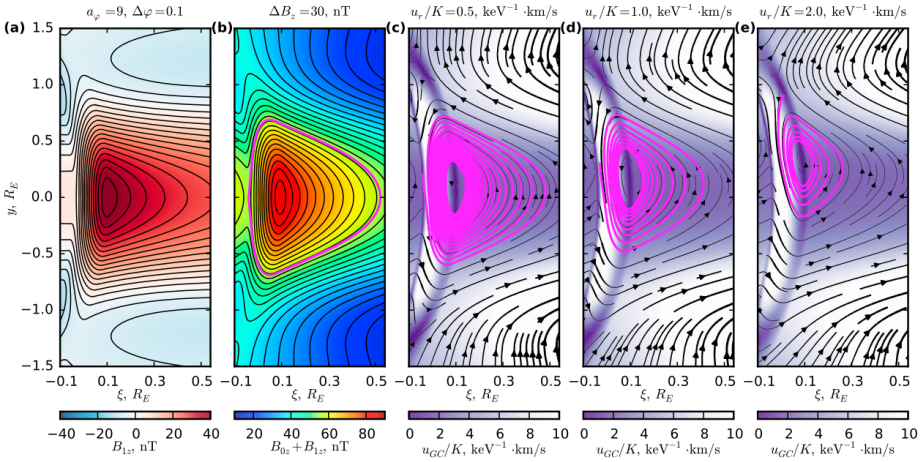

Figure 6.16: The mechanism of stable trapping. (a) The component of the front, without background magnetic field, in the equatorial plane of the coordinate system moving with the front; (b) total B_z, the separatrix between the open and closed $B_z = const$ contours is shown with a magenta line; (c-e) the phase portraits of the equatorial guiding-center motion for various initial energy, sample stably trapped trajectories are shown with magenta lines. The parameter u_r/K represents the ion energy which is of 280 keV (c), 140 keV (b) and 70 keV (e). Credit: [103].

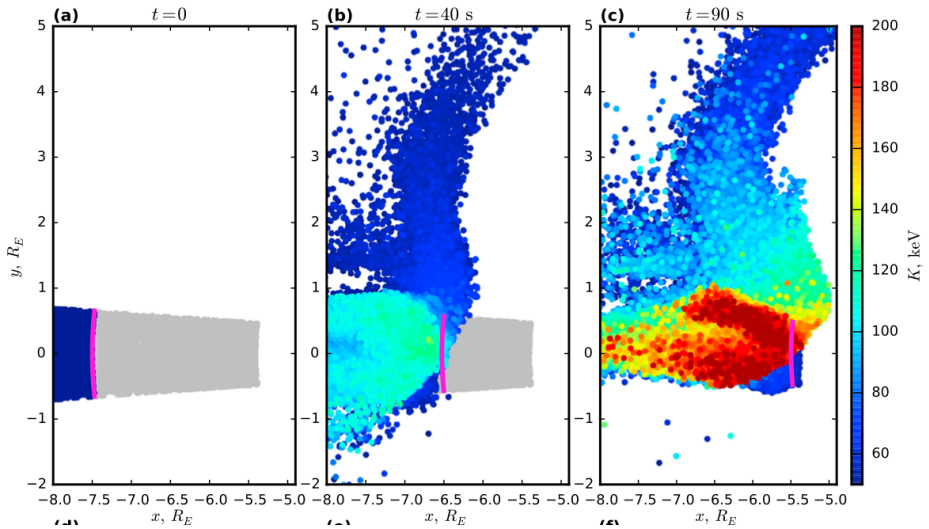

Figure 6.17: Three-dimensional test particle simulations of proton trapping and energization at the jet front. (a-c) The snapshots of the equatorial crossings of protons with the initial energy of 50 keV; particle energy is indicated with color. Credit: [103].

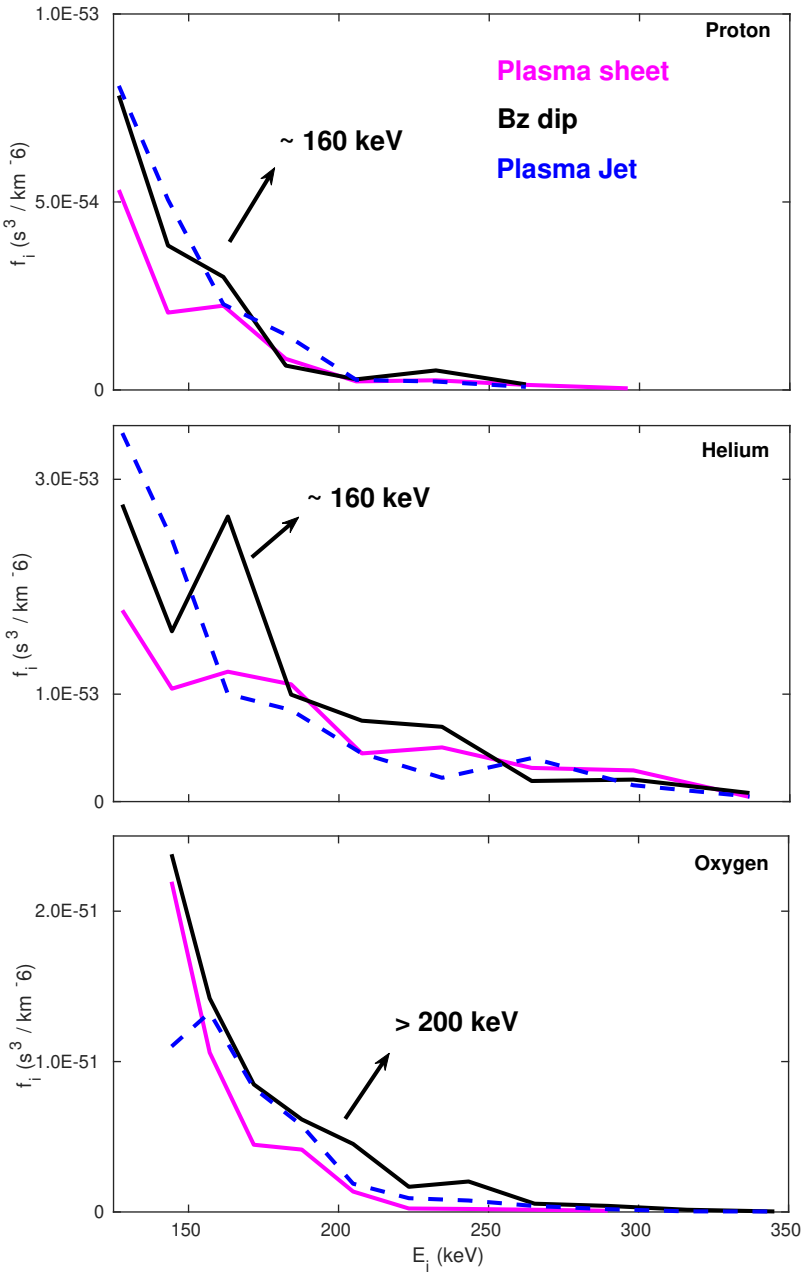

Figure 6.18: Distribution functions as a function of energy for protons, helium and oxygen ions (upper, middle and bottom panels) in the region of the plasma sheet (magenta lines), magnetic dip (black lines), and plasma jet (blue lines).

along the y direction, that is the size of the trapping region, as

$$R_y = \frac{W_i}{|q_i \langle E_y \rangle|} \tag{6.2}$$

where W_i is the energy of the beam, q_i is the ion charge, and $\langle E_y \rangle$ is the average value of the electric field in the region of the magnetic dip. Using the observed value of $\langle E_y \rangle$ ∼4 mV/m, and $q_i = q_p$ for all the protons and helium ions, we obtained a value of $R_y = 5R_E$, that is in agreement with previous studies [110, 111]. To obtain a consistent result also for oxygen ions, we should consider $q_i \geq 2q_p$, since W_i is larger for these ions. This is in agreement with observations reported by [26, 27] and [25], showing the dominance of multiply-charged heavy ions for energies larger than 150 keV in the magnetotail. Furthermore, we notice that, in order to satisfy the resonance condition with $V_\phi = 330$ km/s, ions should have an initial energy of 0.5 keV for protons, 2 keV for helium, and 8 keV for singly charged oxygen ions. The ions gain energy proportionally to the time τ that they spend in the trapping region [101]. We can estimate the efficiency of the acceleration mechanism as $\Delta W = W_i - W_{res}$, where W_i is the energy of the observed beam and W_{res} is the energy which satisfy the resonant condition. We found that ΔW_i is equal to 159.5 keV for protons, it is 156 keV for helium, and of the order of 192 keV for oxygen ions. The resonant acceleration mechanism is more efficient for the ion species which spend more time in the trapping region, as protons and multiply charged oxygen ions. This result is reasonable, since light or heavy multiply charged ions have smaller Larmor radius, and consequently, they can spend more time in the trapping region, as also discussed by [102].

6.5.1 Conclusions

We reported high resolution MMS spacecraft measurements of earthward propagating plasma jet fronts as drivers for suprathermal ion acceleration during unsteady magnetic reconnection. The observed magnetic and electric field profiles as well as plasma measurements are consistent with the formation of a magnetic bottle between the two jets. Since the fronts have different propagation speeds, the second jet being faster, the bottle contracts. We found that the ion pitch angle distributions (PADs) depend on the specific energy range, namely lower energies ions ∼ 10 keV have PA around 90°, while higher energy ions ∼ 100 keV are almost field-aligned. We propose that thermal ions from the ambient plasma population are initially trapped inside the magnetic bottle, and as the bottle contracts ions are energized along the parallel direction through a first-order Fermi mechanism until they

fall into the loss cone. Due to the interaction between the two jets, mirror points are likely formed along the flux tubes closer to the CS rather than at their foot points. We estimate a typical scale of the magnetic field gradient $L \sim 7000$ km, corresponding to an energy threshold ~ 108 keV for protons, above which ions are no more trapped and they can escape from the bottle. The value of E_{esc} increases considering multiply charged heavier ions, in agreement with the distributions reported in Figure 6.10. A similar Fermi-like acceleration mechanism at reconnection jet fronts was observed for electrons [15] but has not been reported for ions. Here, we show for the first time in situ evidence of such mechanism for ions, which are accelerated up to ~ 10 times their thermal energy. The observed jet fronts are reminiscent of the downward-moving reconnected field lines in collapsing magnetic traps during solar flares, where strong particle acceleration occurs. In contrast to the classical scenario of magnetic traps where mirror points are formed at foot points, our observations suggest that mirror points could instead be formed closer to the CS due to the interaction of subsequents jets, as also suggested by [88]. We speculate that during unsteady reconnection many magnetic bottles could form upon interaction of jets, which could lead even to acceleration to high energies.

Furthermore, we study the acceleration occurring ahead of the plasma jet front. We observe that, in the region of the magnetic field depletion where B_z changes sign, a potential well can form and ions can be stably trapped therein. Since the jet propagates along the x direction, this region can be squeezed and the ion can be accelerated via a resonant surfing mechanism. We actually observe the formation of ion beams for the different ion species, suggesting that only a portion of the ion population is energized. This is in agreement with the ion trapping in the magnetic depletion region. Also, the beams are observed at different energies for the different ion species, accordingly to the resonance surfing acceleration mechanism which can preferentially energize one species. We qualitatively compare the MMS observations with the numerical model developed by [101, 102, 103]. We suggest that this mechanism is more efficient for the ion species which spend more time in the trapping region, as protons and multiply charged oxygen ions. This is also in agreement with results reported by [26, 27] and [25], showing observations of multiply-charged heavy ions dominating for energies larger than 150 keV in the magnetotail.

These ion acceleration mechanism can have far-reaching implications for many astrophysical environments, in particular solar and stellar flares where unsteady reconnection and jet fronts are ubiquitous.

Chapter 7

Introduction to Turbulence and Kelvin-Helmholtz instability

In the next two chapters we study the kinetic dissipation in the Kelvin-Helmohtz (KH) instability at the Earth's magnetopause as observed by MMS. In particular we analyse observations showing the formation of ion beam driven by turbulence in the magnetospheric KH instability. Before to present the observations we discuss theoretically the characteristics of the KH instability and of the turbulence in plasmas.

7.1 Basics of the KH instability

A very important problem in space plasma physics is how solar wind interacts with the Earth's magnetosphere after interactions through the Earth's bow shock. Many processes are at play for the mixing of the two plasmas nearby the interface, eventually leading to solar wind plasma entering into the Earth's magnetosphere. The solar wind carries throughout the solar system the Sun's magnetic field, also known as the Inter-planetary Magnetic Field (IMF). Because of the rotation of the Sun, the magnetic field has a spiral shape, known as Parker spiral [112]. According to the frozen-in theorem the plasma and the magnetic field lines are linked one to each other so that, in principle, no mixing between solar wind and magnetospheric plasma should exist. Observations show instead the presence of cold dense solar wind plasma inside the magnetosphere. The IMF component B_z, perpendicular to the ecliptic, has a fundamental role in solar wind plasma transfer into the magnetosphere. Indeed, if $B_{z,IMF}$ is directed southward, it interacts with antiparallel terrestrial field lines making possible reconnection processes at the dayside. This phenomena is at the origin of solar wind plasma enter into mag-

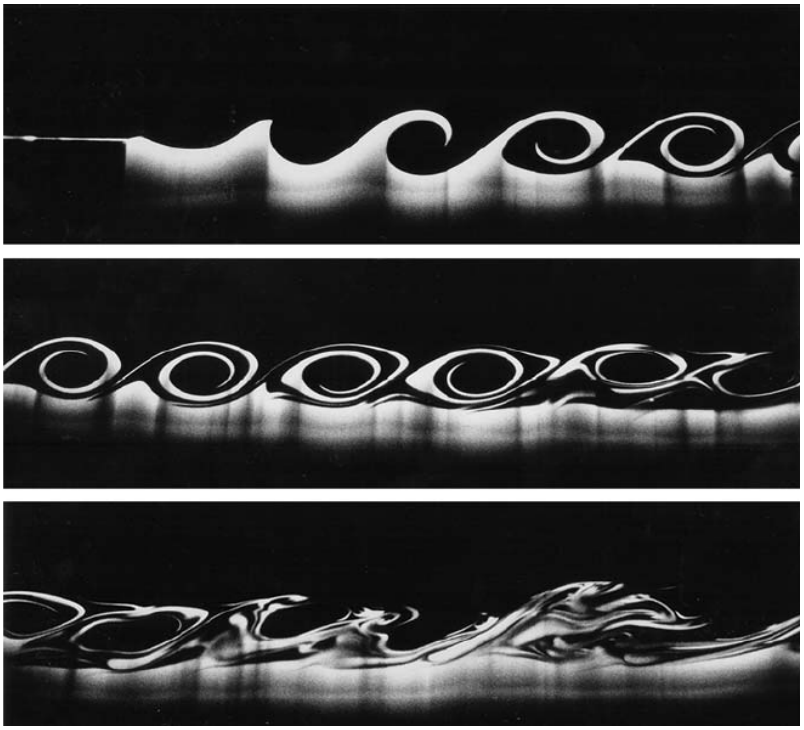

Figure 7.1: Development of a Kelvin-Helmholtz instability in the laboratory. The upper and faster moving layer is slightly less dense than the lower layer. At first, waves form and overturn in a two-dimensional fashion but, eventually, three-dimensional motions appear that lead to turbulence and complete the mixing. Credit: [114].

netopause [113]. The solar wind particles are accelerated and pushed inside the magnetosphere as a consequence of the reconnection process. However satellites observations have revealed that even under northward IMF conditions cold and dense plasma is injected into the magnetosphere, in particular along the flanks of the magnetosphere. Different possible mechanisms have been proposed to explain these observations. One of the most accepted is the Kelvin–Helmholtz instability. The Kelvin–Helmholtz instability can occur when there is a velocity shear in a single continuous fluid, or where there is a velocity difference across the interface between two fluids. An example of KH obtained in laboratory using two fluids with different densities is shown in Figure 7.1.

Kelvin-Helmohtz instability (KHI) can also occur on the equatorial flanks of the magnetopause at Earth [115] and other planets [116]. Global simulations have also shown that the KHI can be generated by jets in the magnetosheath [117]. The development of the KHI begins as an antisunward

propagating surface wave, which "rolls up" into a train of vortices in the wave's non-linear phase. The presence of the KHI can have consequences for the coupling of the magnetosphere to the magnetosheath, leading to magnetic reconnection even for northward interplanetary magnetic field and allowing momentum and mass transport across the magnetopause [118]. KHI simulations show the development of turbulence within the vortices, which is thought to be driven by secondary instabilities that form as the KH vortices roll up [117, 119]. Turbulence provides a pathway for the transfer of energy from the large-scale KH vortices to small scales where collisionless processes can lead to dissipation and particle heating. Simulations show that turbulence aids in plasma mixing within the KHI [120]. The tangling of magnetic fields due to turbulence may also lead to additional reconnection sites in the KHI. While some observational studies suggest the presence of turbulence, extensive observational examination of the properties of KHI related turbulence has been performed in [121].

7.2 On the MHD theory

Very often it is interesting to use a large scale description of the plasmas, neglecting the effect of particle collisions and considering the dynamics of each single kind of particle as a whole. In this case the *fluid* description can be used. In this picture, the plasma can be seen as a superposition of interacting fluids. Still, the fluid equations are quite difficult to use, and further approximation can be made to simplify it. This assumption lead to the *magnetohydrodynamic* (MHD) description of a plasma. The involved particles are electrons and ions with mass m_e and m_i, and eventually heavier ions. Since $m_p \sim 2000 m_e$, terms containing m_e/m_p can be neglected. This correspond to ignoring the inertia of the electrons in the flow. In the MHD theory the plasma can be seen as a proton fluid, described by a fluid-like equations, followed by and electron current obeying to the Ohm's law. In a simplified case, when the flow is incompressible, the mass density $\rho = const$ and we easily obtain the equation for the conservation of the mass which is $\nabla \cdot \mathbf{v} = 0$, where $\mathbf{v} = \mathbf{v}(\mathbf{r}, t)$ is the flow velocity. We introduce a new variable for the magnetic field as

$$\mathbf{b}(\mathbf{r}, t) = \frac{\mathbf{B}}{\sqrt{4\pi\rho}}, \tag{7.1}$$

where $\mathbf{B}$ is the magnetic field. Since in the incompressible case ρ is constant, $\mathbf{b}$ is proportional to $\mathbf{B}$ but has the dimension of a velocity. Introducing the cinematic viscosity ν, the magnetic diffusivity μ, and the kinetic pressure p,

the MHD equations in the incompressible approximation results to be

$$\frac{\partial \mathbf{v}}{\partial t} + (\mathbf{v} \cdot \nabla)\, \mathbf{v} = (\nabla \times \mathbf{b}) \times \mathbf{b} - \nabla p + \nu \nabla^2 \mathbf{v} \tag{7.2}$$

$$\frac{\partial \mathbf{b}}{\partial t} = \nabla \times (\mathbf{v} \times \mathbf{b}) + \mu \nabla^2 \mathbf{b} \tag{7.3}$$

$$\nabla \cdot \mathbf{v} = \nabla \cdot \mathbf{b} = 0. \tag{7.4}$$

The equation systems is composed by the Newton equation (7.2), the induction equation (7.3), both cointaining non-linear terms, and by the conservation equations (7.4). Previous equations can be compacted by using the Elsasser variables [122]:

$$\mathbf{z}^{\pm} = \mathbf{v} \pm \mathbf{b}. \tag{7.5}$$

These variables are useful to study the correlation between the fluctuation of magnetic field and velocity. The MHD equations using the Elsasser variables become

$$\frac{\partial \mathbf{z}^{\pm}}{\partial t} + \left(\mathbf{z}^{\mp} \cdot \nabla\right) \mathbf{z}^{\pm} = -\frac{1}{\rho} \nabla \left(p + \frac{B^2}{8\pi} \right) + \frac{\nu + \mu}{2} \nabla^2 \mathbf{z}^{+} + \frac{\nu - \mu}{2} \nabla^2 \mathbf{z}^{-} \tag{7.6}$$

$$\nabla \cdot \mathbf{z}^{\pm} = 0. \tag{7.7}$$

This is a very compact four-equations system. It is worth to notice that non-linear terms are proportional to both the variables, so non-linearities vanish if one of the Elsasser field is zero $\mathbf{z}^{\pm} = 0$.

7.3 Main properties of the turbulence

The non-linear structure of the MHD equations leads to turbulence. In MHD equations are present both non-linear and dissipative terms. In fluid theory the *Reynolds number* R_e is used to look at the balance between these two terms. Lets set ℓ_0 the typical length of the system, v_0 and B_0 the typical (averaged) velocity and magnetic field. It is also useful to introduce the Alfvén velocity $v_A = B_0/\sqrt{4\pi\rho}$, representing the typical propagation velocity for Alfvén waves. By dimensional analysis, the non-linear term in the MHD equation $(\mathbf{v} \cdot \nabla)\mathbf{v}$ corresponds to v_0^2/ℓ_0. Similarly, the dissipation term $\nu \nabla^2 \mathbf{v}$ corresponds to $\nu v_0/\ell_0^2$. The ratio between the two terms is the *kinematic Reynolds number* $R_v = v_0 \ell_0/\nu$. In analogy we can define the *magnetic Reynolds number* $R_m = v_A \ell_0/\mu$. For low Reynolds number it is clear that the linear dissipative term dominates the dynamics. This regime is called *laminar*. While, if the Reynolds number overcome the unity the non-linear term become important.

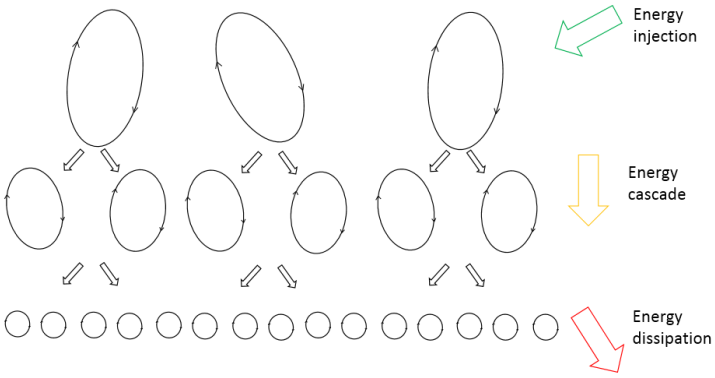

Figure 7.2: Schematic view of the Richardson cascade. The hierarchy of structures represents the non-linear transfer of energy at smaller scales.

One of the feature of the turbulent regime is the presence of singular structures as, for example, vortices. At low Reynolds number large structures are formed at typical scale ℓ_0. As the Reynolds number increases, the energy is transferred from largest vortices to smaller and smaller structures, due to the non-linear interactions. When the Reynolds number exceeds some critical value, the flow is said to be in *fully developed turbulence*. In this regime it is possible to distinguishes three important scales:

- the *integral scale* is the large scale at which the energy is injected in the system from some external force (the dynamics is linear)
- the *inertial scale* correspond to the regime where non-linear interactions transfer the energy at smaller scales (the dynamics is non-linear)
- the *dissipative scale* correspond to the regime where the dissipative terms dominate.

This idea have been visualized as an energy cascade by Richardson in 1922 [123]. In Figure 7.2 is shown a scheme of such cascade. In this framework the energy is injected in the system at the integral scale, due to the non-linear interactions, the energy cascades through the hierarchy at smaller and smaller scales. At dissipation scale the cascade is stopped and the energy is eventually dissipated.

7.4 Introduction to the Yaglom law

The Yaglom law is useful t evaluate the local value of the energy transfer flux. For laboratory plasmas both the dissipative and viscosity coefficients

are known, so it is easily to evaluate the energy transfer flux. While, for spacecraft observations, those parameters are unknown, so that the energy transfer is indirectly measured by using the Yaglom law. This law makes a linear scaling relation between the third-order energy transfer rate and the mean energy dissipation rate. In MHD theory, by using the Elsasser variables, the Yaglom law can be written as

$$Y^{\pm}(\ell) = \langle |\Delta z^{\pm}(\ell)|^2 \Delta z_l^{\mp}(\ell) \rangle = -\frac{4}{3} \langle \varepsilon^{\pm}(\ell) \rangle \ell, \tag{7.8}$$

where $Y^{\pm}(\ell)$ is the third-order mixed moment, $\Delta z^{\pm}$ is the increment of the Elsasser variables at the scale ℓ, $\langle \varepsilon^{\pm} \rangle$ is the average of the energy transfer flux. The sign in the right hand of the Equation (7.4) it is important because it indicates the "direction" of the energy transfer flux, which can be towards smaller scales or in the opposite direction. The Yaglom law have been also derived by [124] by using temporal scales instead of spatial one. The Politano & Pouquet (PP) law for the mixed third-order moment $Y^{\pm}(\Delta t)$ is

$$Y^{\pm}(\Delta t) = \langle |\Delta z^{\pm}(t, \Delta t)|^2 \, \Delta z_l^{\mp}(t, \Delta t) \rangle = -\frac{4}{3} \langle \varepsilon^{\pm} \rangle \Delta t \langle v \rangle \ . \tag{7.9}$$

$\Delta\psi(t, \Delta t) = \psi(t + \Delta t) - \psi(t)$ indicates the increment of a generic field ψ across a temporal scale Δt, and the subscript l indicates the longitudinal component, i.e., parallel to the bulk speed. When considering the total energy flux $Y = (Y^+ + Y^-)/2$, the proportionality factor of the PP law is the mean energy transfer rate $\langle \varepsilon \rangle = (\langle \varepsilon^+ \rangle + \langle \varepsilon^- \rangle)/2$. The PP law has been validated in numerical simulations [125], in the solar wind and in the terrestrial magnetosheath. Based on the PP law (7.9), an heuristic proxy of the local energy transfer rate (LET) at the scale Δt is thus defined by introducing the quantity:

$$\varepsilon^{\pm}(t, \Delta t) = -\frac{|\Delta z^{\pm}(t, \Delta t)|^2 \, \Delta z_L^{\mp}(t, \Delta t)}{\Delta t \langle v \rangle} \ , \tag{7.10}$$

and then computing the average $\varepsilon(t, \Delta t) = (\varepsilon^+(t, \Delta t) + \varepsilon^-(t, \Delta t))/2$. At a given scale, each field increment in the time series can thus be associated with the local value of $\varepsilon(t, \Delta t)$ [126, 127]. Moreover, when written in terms of velocity and magnetic field, the LET can be separated in two additive terms, one associated with the magnetic and kinetic energy advected by the velocity fluctuations, $\varepsilon_e = -3/(4\Delta t \langle v \rangle)[\Delta v_{||}(\Delta v^2 + \Delta b^2)]$, and the other with the cross-helicity coupled to the longitudinal magnetic fluctuations, $\varepsilon_c = -3/(4\Delta t \langle v \rangle)[-2\Delta b_{||}(\Delta \mathbf{v} \cdot \Delta \mathbf{b})]$ [126, 127]. The dominance of one of the last two terms may strongly influence the heating process, and so that the velocity distribution function (VDF) of the particles may present different shapes.

Chapter 8

Observations of turbulence in magnetospheric KH instability

We discuss measurements in the turbulent terrestrial magnetosphere provided by the Magnetospheric MultiScale (MMS) mission [23]. The unprecedented high-cadence for ions [61] and magnetic fields [58] data explore more in depth the link between the MHD energy cascade and the kinetic processes associated with deviation from Maxwellian distribution functions. The Earth's magnetopause flanks constantly experience a variable flow shear between stagnant or weakly drifting plasma in the magnetosphere and a strong and variable antisunward plasma flow in the adjacent magnetosheath due to the shocked solar wind. Certain conditions of plasma flow shear and directions of the ambient magnetic field across the low-latitude magnetopause current sheet (CS) allow the Kelvin-Helmholtz (KH) instability to grow and form magnetopause surface waves that propagate in the antisunward direction of the magnetosheath flow. The wave amplitude is expected to grow and generate rolled-up flow vortices in the nonlinear phase of its evolution along the flank. Here we report MMS observations for the study of turbulence properties in association with a KHI, studying the link between the MHD energy cascade and the kinetic processes associated with deviation from Maxwellian distribution functions.

8.1 Event overview

On 8 September 2015, MMS was located in the dusk-side magnetopause, moving from the low-latitude boundary layer into the magnetosheath, between 10:07:04 UT and 11:25:34 UT, at approximately $(x, y, z)_{GSE} = (4.9, 9.2, 0.1)R_E$ with an interspacecraft tetrahedron separation of $150 - 185$ km. Figure 8.1

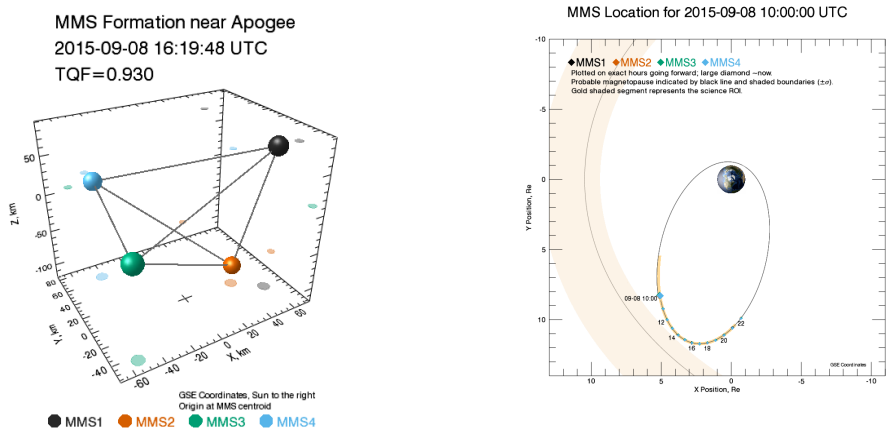

Figure 8.1: Spacecraft configuration (left side) and position (right side) in the (x, y) plane.

shows the spacecraft configuration (left side) and the spacecraft trajectory in the (x, y) plane (right side), where the magnetic field lines (purple lines) are obtained from the Tsyganenko model [83]. Figure 8.2 (left) shows MMS1 fast survey observations between 09:00 and 11:50 UT on 8 September 2015. Energy-time spectrograms of ions and electrons show that MMS was inside the magnetosphere proper until 09:21:24 UT (first vertical dotted line) characterized by a low plasma density and high ion temperature, slow average ion velocity, and a geomagnetic field $\mathbf{B}_{GSE} = (20, 5, 65)$ nT. This was followed by a 2 h long interval of boundary layer plasma. Significant variations were observed in the ion temperature and $\mathbf{B}$ during the last ∼80 min of this period between 10:07:30 UT (second vertical line) and 11:27:40 UT (third vertical line) when MMS exited into the cold, dense magnetosheath plasma.

8.2 Analysis of turbulence in KHI

In the following we focus on the interval shown in the right side of Figure 8.2. During this period the spacecraft orbit experienced multiple crossings of the large-scale vortices generated by Kelvin-Helmholtz (KH) instability. Crossings were revealed by several ion-scale periodic current sheets [128], separating the hotter plasma inside the magnetosphere from the colder, denser magnetosheath. Turbulence in the magnetosphere intervals was studied in depth, showing the presence of a well defined inertial range and intermittency [121], after validating the Taylor hypothesis. In this work, we have selected 53 of the same boundary layer (BL) subintervals, carefully exclud-

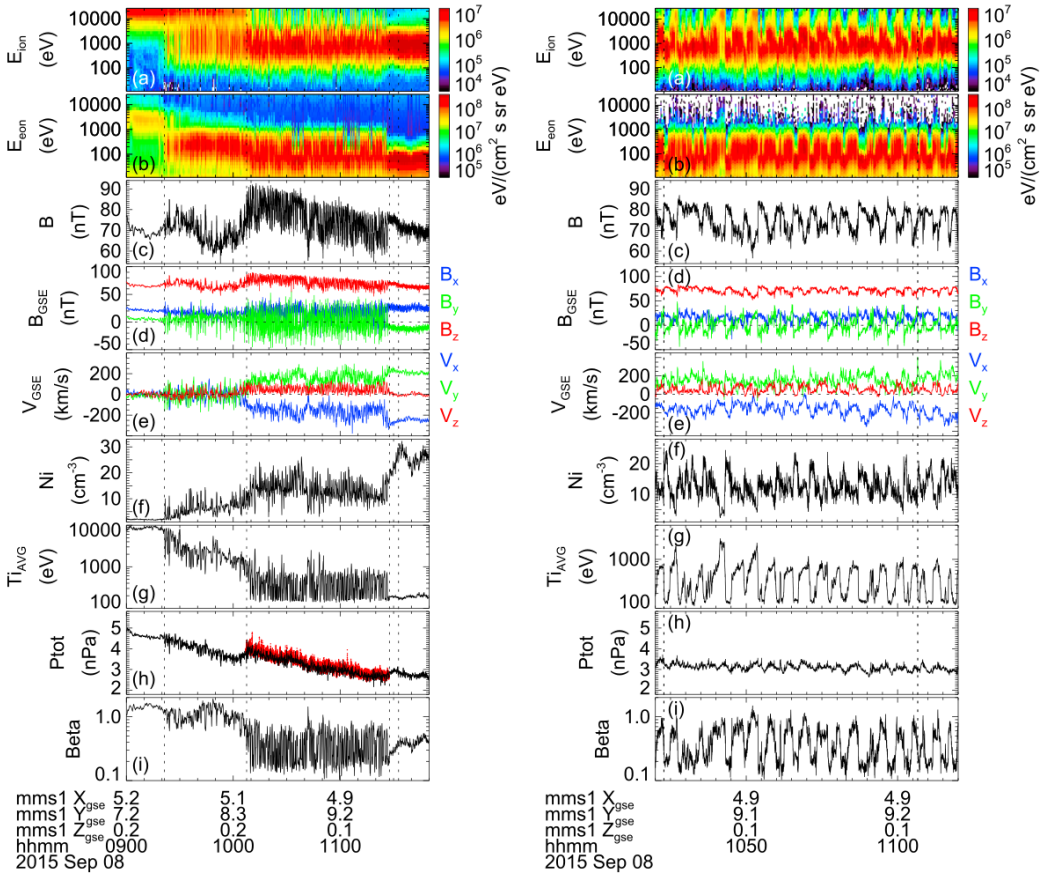

Figure 8.2: MMS1 observations are shown 09:00–11:50 UT (left, fast survey) and 10:44–11:04 UT (right, burst mode) on 8 September 2015. The figure displays omni-directional energy-time spectrograms for (a) ions and (b) electrons, (c) **B** magnitude, (d) GSE components of **B**, (e) GSE components of the ion velocity, (f) ion plasma number density (N_i), (g) average ion temperature ($T_{i,avg}$), (h) sum of the magnetic pressure $P_b = B/2\mu 0$, ion plasma pressure $P_i = N_i k_B T_{i,avg}$, and electron plasma pressure $P_e = N_e k_B T_{e,avg}$ (black: fast survey; red: burst), and (i) total plasma β. Credit: [128].

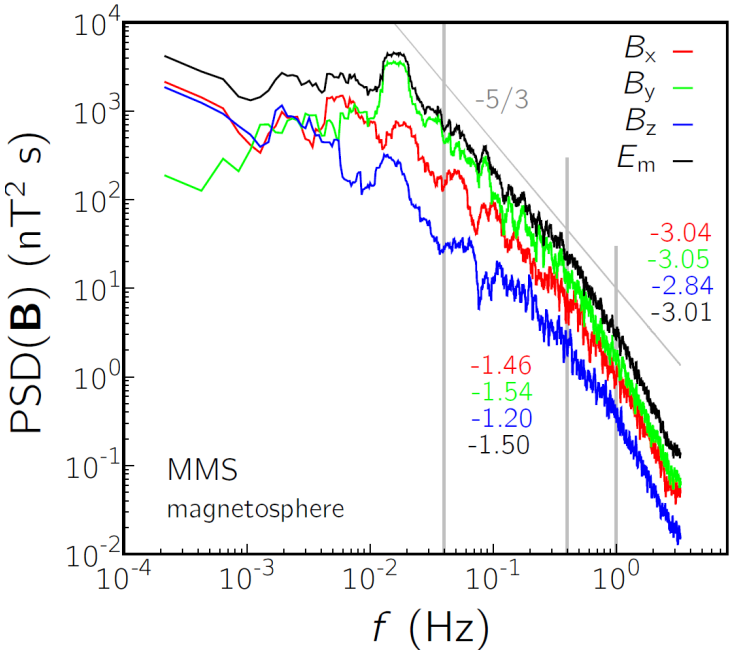

Figure 8.3: Power spectral density (PSD) of the magnetic field from the KHI sequence considering the contribution of the 53 magnetospheric intervals only. Fitted spectral indices are indicated for the magnetic field components B_x, B_y and B_z, and for the trace E_m. The scale used to estimate the LET in this work, Δt= 1.2 s, is indicated by the orange, dashed, vertical line. The rightmost gray line indicates the ion cyclotron frequency f_{ci}, while the other two gray lines delimitate the magnetohydrodynamics inertial range.

ing the current sheets and magnetosheath regions. This provides an ensemble of turbulent plasma [119, 121], with typical ion-cyclotron frequency $f_{ci} \simeq 1$ Hz and magnetic fluctuation level $\delta B_{rms}/B_0 \simeq 0.15$.

In Figure 8.3 we present the magnetic field component power spectral density (PSD), estimated using the *compressed sensing* technique [137, 138], previously developed for Voyager's solar wind gapped dataset [139] and heliosheath and interstellar data [140]. Here the technique allows us to recover the PSD of the KHI sequence considering the contribution of the 53 magnetospheric intervals only. The spectral indices are computed by linear regression in the log-log space in the ranges $f \in [0.04, 0.4]$ Hz and $f \in [1, 3]$ Hz, for each magnetic field component. The presence of a broad Kolmogorov scaling range is evident, between the KH forcing frequency 0.016 Hz (63 s) [128] and the first spectral break. The location of the spectral breaks compares well with spacecraft-frame frequencies of proton cyclotron-scale structures and ion in-

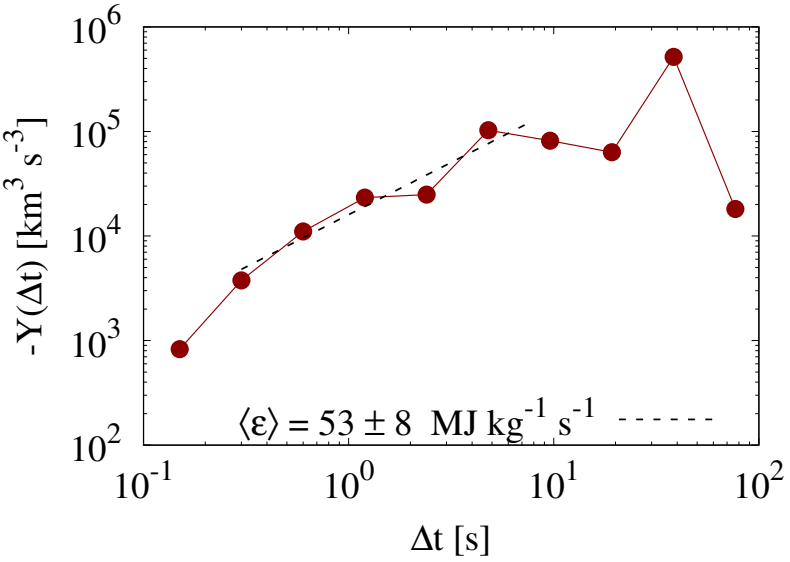

Figure 8.4: The Politano-Poquet law estimated using the MMS1 measurements in the magnetospheric KHI (red symbols and line). A rough linear scaling can be identified in the range 0.3-8 s. The fitted law is shown as dashed line.

ertial structures, respectively ($f_{ci} \approx V/2\pi r_{ci} \approx 1$ Hz and $f_{ci} \approx V/2\pi r_{ci} \approx 0.45$ Hz). The ion plasma $\beta_i = 2v_{th}^2/v_A^2$, with the thermal speed $v_{th} = \sqrt{k_B T_p/m_p}$ and the Alfvén speed $v_A = B/\sqrt{4\pi\rho}$, is around unity, fluctuating in the range 0.5—1.5.

The proxy $\varepsilon(t, \Delta t)$ given in Equation (7.10) was calculated at different scales Δt using the MMS1 spacecraft velocity, magnetic field and density measurements for the turbulent regions of the 53 sub-intervals described above [121].

Upon averaging over the whole ensemble of 53 sub-intervals, the scale-dependent third-order moment (7.9) is approximately in agreement with the linear PP-law prediction (7.9), as evidenced in Figure 8.4. A rough linear fit in a region extending from the MHD inertial range down to ion scales provides a mean energy transfer rate $\langle\varepsilon\rangle \simeq 53 \pm 8$ MJ kg^{-1}s^{-1}. To our knowledge, this is the first observation of the PP law inside the Earth magnetosphere. Such result falls well within the range of values recently found in a survey of the compressible third-order scaling in the magnetosheath, which spanned [1—10^7] J kg^{-1}s^{-1} [141]. Incidentally, it was shown using solar wind data that including compressive effects can result in the increase of mean energy

transfer rate up to one or more order of magnitude. Notice that the standard deviation associated to the mean energy transfer obtained in our sample is $\sigma = 3016$ J kg^{-1}s^{-1}, highlighting the known fact that only a small fraction (1.8% in this case) of the turbulent energy exchange across scales accounts for the neat energy cascade.

Measurements of ion distribution functions and moments are provided by the Fast Plasma Investigation (FPI) instrument, covering an energy range of [0.1—30] keV, with cadence of 150 ms. Magnetic field were measured by the Flux-Gate Magnetometers (FGM) [58], with a cadence of 128 Hz, and were carefully synchronized to the plasma data. The local longitudinal direction was determined as the average speed evaluated over 30 s running windows, of the order of the velocity correlation scale [121]. In the following, we will focus on the scale $\Delta t = 1.2$ s, which corresponds to a scale of transition between the MHD inertial range and the ion kinetic scales [121]. At such scale, the PP law is still valid, so that the local proxy LET gives a reasonable description of the rate at which energy is locally transferred, being available to excite smaller scales processes. Therefore, it represents the cross-scale connection between the fluid and kinetic plasma regimes. In order to simplify the notation, the LET explicit t and Δt dependency will be dropped in the following.

Panels (A)–(D) of Figure 8.2 show MMS measurements of several quantities in one of the 53 selected BL subintervals. Panel (E) illustrates the bursty, intermittent nature of ε. A representation of the energy flow across scales is provided by the scalogram of the LET [129], shown in panel (F). The energy path across scales is clearly visible, as well as the small-scale intermittent structures (the bright regions at small scales) that contain a large fraction of energy. Intense, small-scale LET events often present a double channel of positive-negative energy flux (see *e.g.* around t=36:01), revealing the complexity of the energy transport mechanism [130].

In order to investigate in detail the possible correlations between the turbulent energy being transferred towards small scales and the deformation of the proton VDF at smaller scales, we identified 94 positive and 94 negative peaks of LET by setting the two thresholds $\varepsilon > \theta_+\sigma$ and $\varepsilon < \theta_-\sigma$. Here $\theta_+ = 1.3$ and $\theta_- = -1.2$ are the threshold values in units of the LET standard deviation, the subscripts indicating the positive or negative LET ensemble. At the time of each peak, the ion VDF was smoothed over 0.45 s (i.e. 3 VFDs) in order to reduce the measurement noise, and then normalized to the local thermal speed v_{th}. We have checked that smoothing over larger intervals, up to 1.2 s, does not modify our results. Two-dimensional cuts of each VDF were visually examined in order to identify possible features and deviation from Maxwellian. All selected VDFs were then classified according to the following categories: (a) quasi-Maxwellian; (b) presence of broad particle

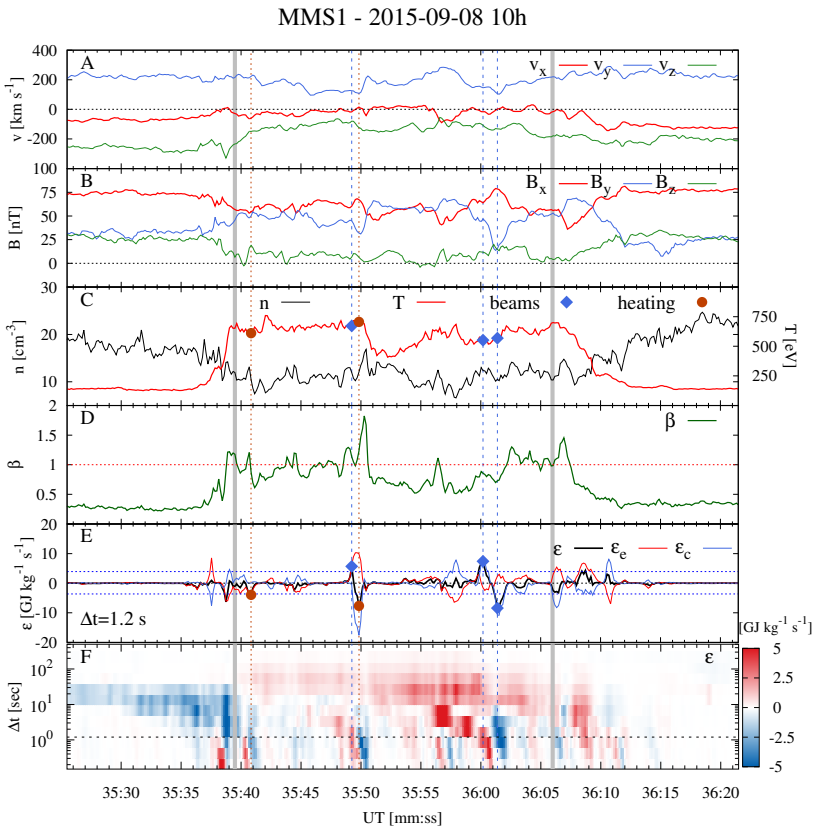

Figure 8.5: A one-minute subsample from the MMS1 data interval, starting at 10:35:21.359 UT on 2015-09-08. Thick vertical gray lines enclose one of the subintervals used for the analysis. Panel A: velocity components (in GSM); B: magnetic field components (in GSM); C: ion density and temperature; D: ion plasma β_i; E: ε, ε_e and ε_c at $\Delta t = 1.2$ s, with the indication of the two thresholds $\theta_+\sigma$ and $\theta_-\sigma$ as blue horizontal dotted lines; F: the scalogram of ε, the horizontal dashed lines indicating the scale $\Delta t = 1.2$ s. The dashed or dotted vertical lines in all panels and the markers in panels C and E indicate the VDFs observed for this subinterval, separately for beams (blue diamonds and dashed line) and heating (dark-orange circles and dotted line).

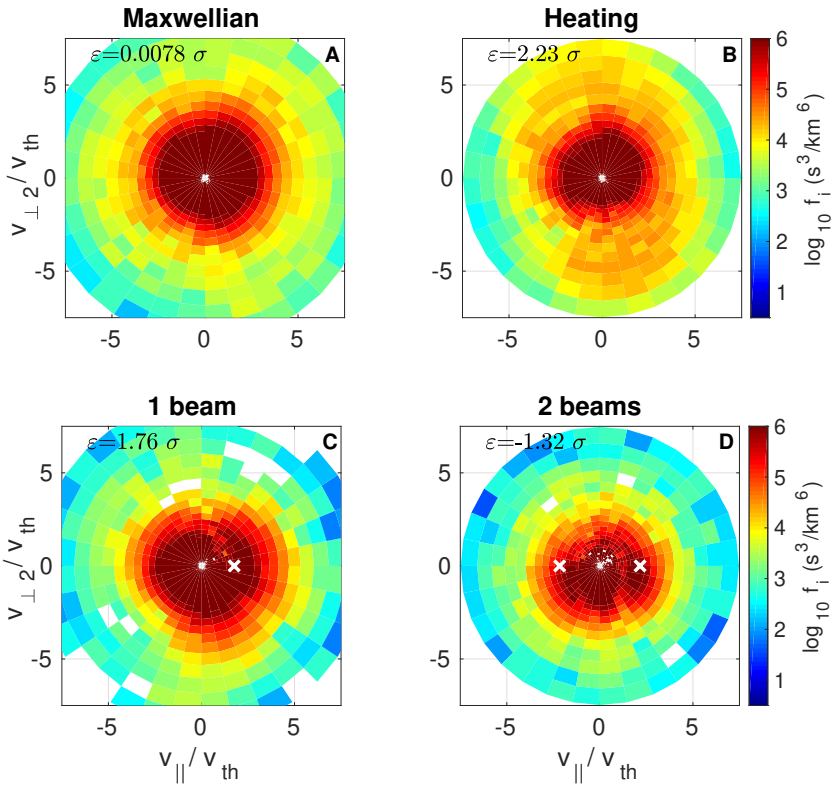

Figure 8.6: Examples of two-dimensional cuts of the 3D proton VDF, measured at LET peaks (panels B—D) or at small LET (panel A). In each panel, the type of VDF is indicated, along with the LET value in standard deviation units. Axes are normalized to the thermal velocity V_{th}. The white crosses in panels C and D represent the local value of the normalized Alfvén velocity.

energization (here labeled as "heating"); (c) presence of one or two beams; (d) other uncategorised features.

Examples of classes (a)—(c) are shown in Figure 8.6. Each panel shows a two-dimensional cut in the $(v_{\perp 2}, v_{\parallel})$ plane, so that the magnetic field direction is along the positive x-axis. Here $v_{\parallel}$ is along the local magnetic field and $v_{\perp,2} = \hat{\mathbf{v}} \times (\hat{\mathbf{v}} \times \hat{\mathbf{b}})$, where $\hat{\mathbf{v}} = \mathbf{v}/|\mathbf{v}|$ and $\hat{\mathbf{b}} = \mathbf{B}/|\mathbf{B}|$. None of the events above the threshold presents Maxwellian VDF (panel A). Broad particle energization (panel B) is the most common feature (more than two-thirds of the cases), while beams (panels C, D) are clearly visible in about 27% of the cases. Note that beams are more likely generated by a positive local energy transfer. In order to compare the statistics with occurrence rates corresponding to small LET values, we have randomly selected 188 VDFs with $|\varepsilon| < 10^{-3}\sigma$.

Table 8.1: Occurrence rate of each class of VDF measured at positive and negative LET peaks and at small LET $|\varepsilon| < 10^{-3}\sigma$.

Classes	$\|\varepsilon\| \sim 0$	$\varepsilon > \theta_+\sigma$	$\varepsilon < \theta_-\sigma$
q-Maxwellian	0.57	0.00	0.00
Heating	0.26	0.63	0.76
Beams	0.17	0.33	0.21
Other	0.00	0.04	0.03

More than half of these are roughly quasi-Maxwellian, confirming that lower energy transfer results in weaker deviation form Maxwellian; heating is seen for about one fourth of the cases, and only one sixth show presence of beams. Results shown in Figure 8.6 and collected in Table 8.1 demonstrate that the particle VDFs are characterized by more evident non-Maxwellian features in the proximity of larger turbulent energy transfer.

The ratio $\varepsilon_{e/c} = \varepsilon_e/\varepsilon_c$ allows to establish whether the cascading energy driving the kinetic processes is dominated by strong gradients, such as current sheets and vorticity filaments ($|\varepsilon_{e/c}| > 1$, found in about two thirds of the cases), or rather by Alfvénic-like, aligned fluctuations ($|\varepsilon_{e/c}| < 1$, as in one third of the cases). Figure 8.7 shows the distribution of VDFs with beams or heating as a function of the total (ε) and partial (ε_c or $\varepsilon_{e/c}$) energy transfer rates. VDFs with heating (70%) are marked with orange symbols, while beams (27%) are in blue. The cases with beams identified for the small LET random cases (17%) are also plotted for reference (light blue circles).

In the top panel of Figure 8.7, the first thing to notice is that heating is increasingly dominating for larger, positive energy transfer, while most of the beams are approximately limited to $1\sigma \leq |\varepsilon| \leq 3\sigma$. This seems to indicate that particularly intense energy transfer may prevent the generation of ordered particle energization, such as beams. A closer look reveals that the large majority of beams are observed for positive cross-helicity contribution $\varepsilon_c > 0$ (overall $\sim 73\%$, including $\sim 80\%$ positive and $\sim 60\%$ negative LET peaks). Looking at the ratio between the energy and cross-helicity terms (bottom panel), in the cases with positive energy transfer the beams are predominantly seen for $|\varepsilon_{e/c}| < 1$ (i.e., within the two horizontal dotted lines). Therefore, while highly energetic, uncorrelated current and vorticity structures produce mostly disordered particle energization, the generation of beams seems to be mainly associated with the presence of Alfvénic velocity and magnetic fluctuations carrying energy towards smaller scales. Note that all beams were observed to be magnetic-field aligned (92% of the cases),

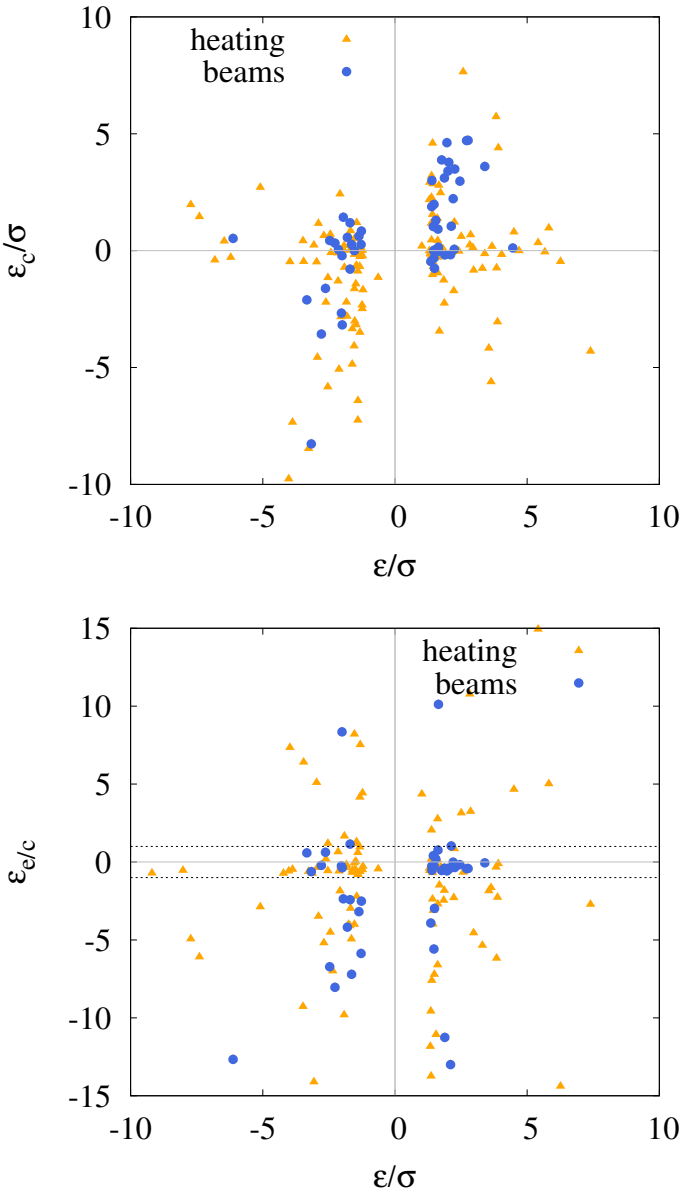

Figure 8.7: Top: distribution of VDFs in the ε–ε_c (top) and in the ε–$\varepsilon_{e/c}$ (bottom) planes, highlighting the majority of beams for dominating, positive ε_c (blue circles) as opposed to the more spread heating (orange triangles).

and are robustly located at $v_{beam} \simeq \pm v_A$, the mean ratio being $V_{beam}/V_A = 0.98 \pm 0.09$, where the error is the standard deviation.

As shown in Figure 8.8, strikingly similar results were observed in a preliminary study of Hybrid Vlasov-Maxwell numerical simulations in two spatial (1024^2 grid points) and three velocity (51^3 grid points) dimensions [136]. In the top panel we show the local energy transfer rate, as well as its energy and cross-helicity components, in a one-dimensional cut of one time snapshot of the simulation, taken at the maximum of the turbulent activity. In the bottom panel, we plot an example of a two-dimensional cut of the full three-dimensional proton VDF, selected at the LET peak dominated by the cross-helicity term and marked by the vertical grey line in the upper panel. An evident ion beam parallel to the ambient magnetic field is located near the Alfvén speed ($v_{th} \simeq 0.7 v_A$) for this simulation.

Figure 8.9 provides indication of localized wave activity in the proximity of the selected events, for the same sub-interval shown in Figure 8.2. The magnetic field components for this interval are shown in the panel (a). This Figure displays the wavelet coerence (panel b), suggesting the presence of some phase relation between two magnetic components perpendicular to the mean field direction. Coherent parallel propagating wave activity manifests itself between this pair of components as narrow regions of high coherency in frequency (typically near the spectral break) and extended in time[143]. Panel (c) of the same Figure shows the corresponding phase difference between the above components, showing regions of left and right circular polarization, with a phase difference close to $\pm 90°$ [143] near the selected events. Furthermore, panel (d) suggests the presence of some phase coherence between two different magnetic field components (the parallel component and one perpendicular component), where coherent structures can be identified as regions of high coherency extended in frequency. Again, this is visible near the identified events (although not exclusively). Panel (e) shows the local intermittency measure (LIM) [144] of the perpendicular fluctuations, and panel (f) the LIM of the parallel fluctuations, evidencing the localization of magnetic spectral power in the time series. The correlation with the selected events is only partial, showing some substantial difference with respect to the LET, which additionally includes a cross-helicity component.

Figure 8.10 provides an example of an Alfvénic vortex-like structure observed around the location of one of the VDFs with beams. The graph shows the components of the magnetic field fluctuations in the minimum variance reference frame estimated within the structure timescale. The magnetic field fluctuations have been defined in the timescale range between 0.04 s and 1.2 s, *i.e.* from the scale of the fluid transition towards ion kinetic scales, by using a bandpass filter based on the wavelet transform [145, 146]. Minimum

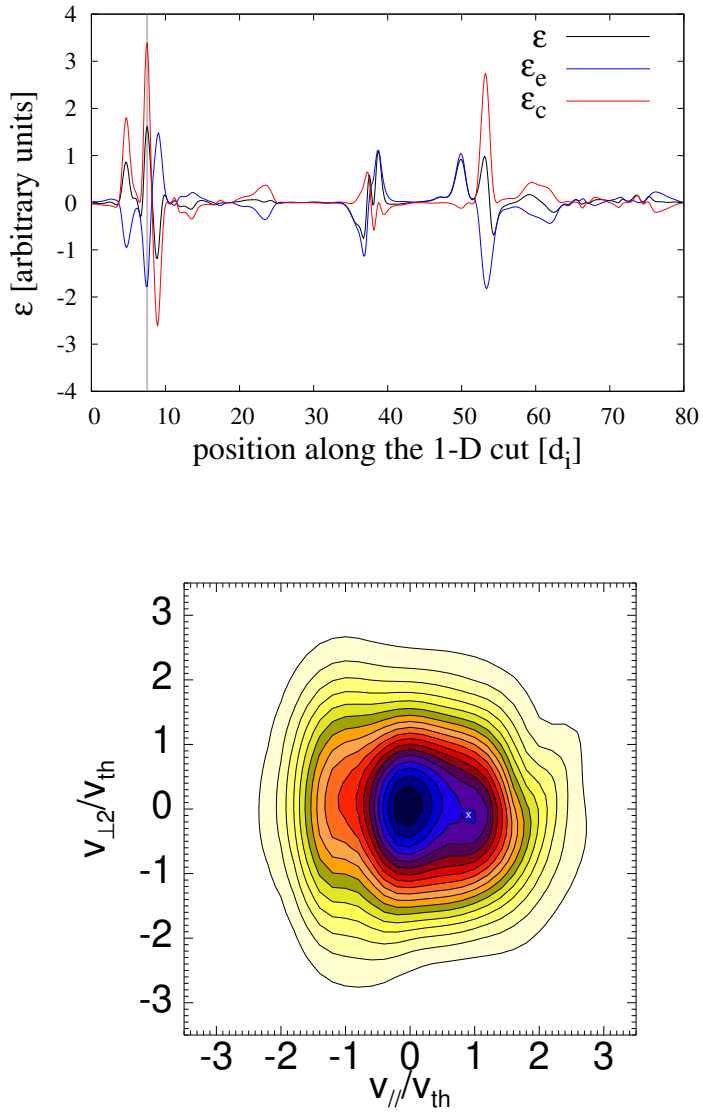

Figure 8.8: Top panel: the local energy transfer rate (black line) and its energy (blue line) and cross-helicity (red line) components, from a one-dimensional cut of a high resolution numerical simulation of the Hybrid Vlasov-Maxwell system. The x-axis is in units of the ion inertial length d_i. Details on the simulation can be found in [136]. Bottom panel: one example of a two-dimensional cut of the proton VDF, selected at the LET peak dominated by the cross-helicity term and marked by the vertical gray line in the upper panel. The small white cross marks the position of a parallel ion beam located near the Alfvén speed $v_{th} \simeq 0.7 v_A$. Courtesy of D.Perrone.

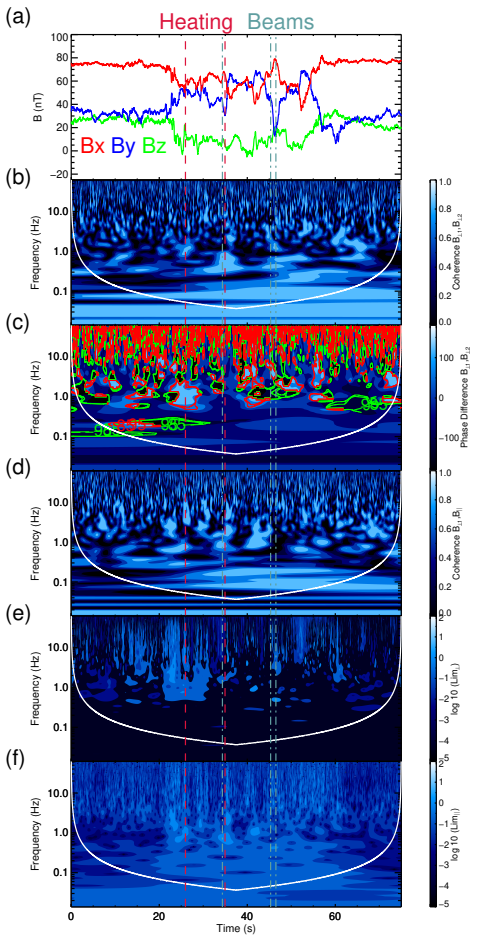

Figure 8.9: Panel (a): the magnetic field components in the GSM reference frame for the interval of Figure 8.2 of the main Letter, starting on 8 September 2015 at 10:35:21.359 UT. Panel (b): the wavelet coherence [142] between the two components of the magnetic field perpendicular to the mean field direction. Panel (c): the corresponding phase difference between these two components. Green and red contours denote regions of left and right circular polarization respectively [143]. Panel (d): the coherence between the parallel and one perpendicular magnetic field components. Panel (e): the local intermittency measure (LIM) [144] of the perpendicular fluctuations. Panel (f): the LIM of the parallel fluctuations. In all panels, the white line denotes the cone of influence region [145] below which the contour plots are unreliable, while the red and pale blue lines denote sites where heating and beams are seen in the VDFs. Heating can be seen to be located near regions of strong LIM in panels (e,f) and coherence in panel (d) while two beams are located near coherent circularly polarized fluctuations in panels (b,c). Courtesy of O. W. Roberts.

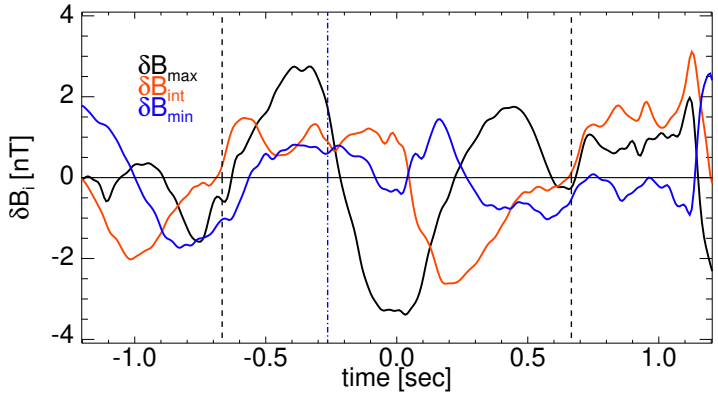

Figure 8.10: Magnetic components fluctuations δB_i in the minimum variance reference frame, estimated within the structure timescale ~ 1.5 s (enclosed between the two vertical black dashed lines) for the first of the three events with beams ($\sim$ 10:35:49 UT in Figure 8.2), indicated here by a blue vertical dot-dashed line. Courtesy of D. Perrone.

variance analysis indicates that the intermediate component is not negligible (the eigenvalues ratios being $\lambda_{int}/\lambda_{max} = 0.47$), *i.e.* it is a bi-dimensional structure, while the directions of variance, with respect to the local mean magnetic field (computed in the same interval as the minimum variance system), are $\theta_{max} = 85.4°$, $\theta_{int} = 54.5°$, $\theta_{min} = 35.9°$, respectively.

In Figure 8.11, we show the conditional power spectral density of the parallel electric field, estimated using 2-second intervals centered at the time of VDFs characterized by beams, heating or quasi-Maxwellian, and then averaged over 10 events each. Peaks indicating persistent wave activity are evident near 100 Hz and 1 kHz [133] only for the VDFs with beams.

All these observations point to the possible interpretation in terms of beams being generated by resonant interaction of protons with Alfvénic-like fluctuations. From quasi-linear theory [134], the resonance condition can be written in the form $\omega - k_{\|} v_{\|} = n\Omega_c$, where ω represents the wave frequency, Doppler-shifted to the plasma rest frame of the particle motion along the magnetic field, $k_{\|}$ and $v_{\|}$ the longitudinal wavenumber and velocity, $n = 0, 1, 2, 3 \cdots$, and Ω_c the proton gyrofrequency. In particular, for $n = 0$ one gets the Landau resonance involving only the parallel velocity component $v_{\|}$; in this case, as proved in [134], a diffusive plateau in the longitudinal proton velocity distribution is generated as the result of resonant wave-particle interaction. For large amplitude fluctuations, the plateau is replaced by a bump [135] in the direction parallel to the magnetic field.

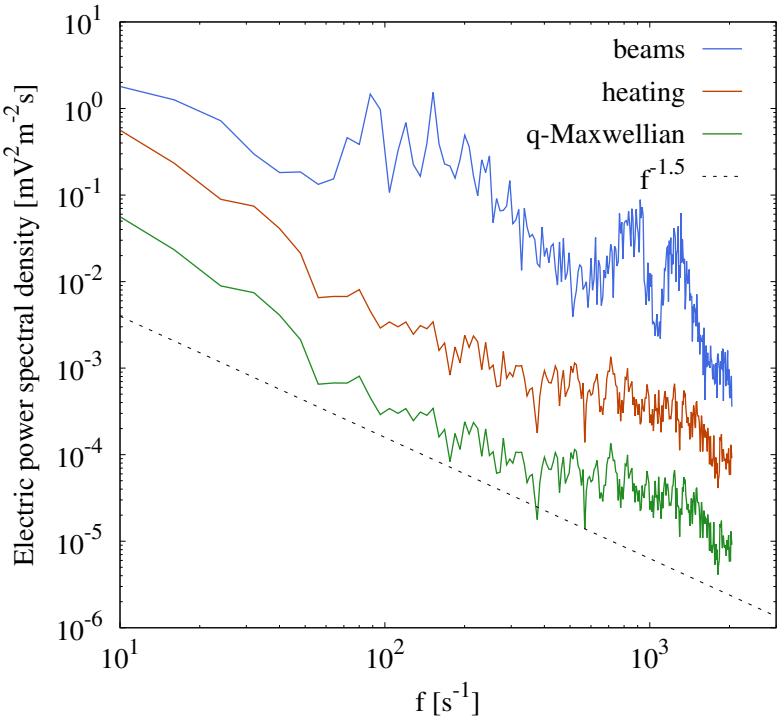

Figure 8.11: Conditional power spectral density of the parallel electric field for VDFs with beams (violet), heating (green), or quasi-Maxwellian (blue). The gray line represents a power law with exponent -1.5, and is only shown for reference.

Moreover, if particles interact with fluctuations of the ion-cyclotron branch, whose phase speed is $v_\phi \leq V_A$, this beam is located at $v_\parallel \simeq V_A$ [131, 132], as observed in the MMS data discussed here.

8.2.1 Conclusions

The cross-scale coupling between fluid turbulence and kinetic processes has been studied though the high-resolution plasma measurements recorded by the MMS spacecraft during one Kelvin-Helmholtz event at the Earth magnetopause. Inspired by the PP law, a heuristic proxy has been used to identify regions of large energy transfer in the time series, where the specific features of the ion VDFs have been examined. Despite the many underlying approximations, the simplified descriptor used here is able to successfully localize regions of magnetospheric plasma with ion VDFs that have more pronounced non-Maxwellian features, corresponding to larger energy transfer. More in particular, field-aligned beams at V_A are more likely generated when such energy is predominantly carried by Alfvénic, aligned velocity and magnetic fluctuations, suggesting the possible role of turbulence-driven Landau resonance in the energy dissipation processes. The results presented here thus expose the strong connection between the local details of the inertial-range turbulent energy transfer and its transformation through small-scale kinetic processes in non-collisional space plasmas. Additionally, they provide part of the answer to one of the major open questions in space plasma physics, namely what are the mechanisms responsible for the dissipation of turbulent energy.

The simple MHD-scale proxy used here could also be considered as a estimator of likelihood for the localization of VDFs with the presence of parallel beams. Indeed, when both conditions of a positive peak in the local energy transfer rate ($\varepsilon > \theta_+$), and a dominating cross-helicity term ($\varepsilon_{e/c} < 1$) are satisfied, then there is a robust 53% probability of having one or two parallel beams in the ion VDFs. These results may thus be relevant for current and future space plasma missions such as MMS, Parker Solar Probe and Solar Orbiter, both for the interpretation of the observations, and as a possible trigger for plasma distributions burst mode and telemetry.

The path towards future steps to improve the proposed diagnostics include: the use of high-resolution Vlasov numerical simulations; the extension of the PP law to small-scale dynamics (Hall-MHD and Vlasov); the inclusion of compressive and anisotropy effects; the study of turbulence in the open solar wind (as soon as MMS data are available) and in other space plasma systems; and the definition of automated, quantitative techniques to determine the VDF type. These results are also discussed in [147].

Chapter 9

Final remarks

In this thesis the ion heating and ion acceleration mechanisms have been investigated by using both numerical simulations and in situ spacecraft observations.

First, we numerically investigated the acceleration of protons and heavy ions, due to the interaction with three-dimensional time-dependent electromagnetic fluctuations in the terrestrial magnetotail. The ions interact with the electromagnetic fluctuations leading to a Fermi-like acceleration mechanism. Studying the dependence of the model on the different free parameters, we found that it is weakly influenced by the particular current sheet configuration. Also, by varying the fluctuation size or the initial ion energy, we observed that there is not a resonant acceleration with ions having their Larmor radius closer to the fluctuation size. The analysis of the ion dynamics demonstrated that most of the energization occurs during stochastic and quasi-adiabatic regimes, having the adiabatic parameter k <3. We evaluated the ion residence time in the current sheet finding that the ions which spend more time in the CS, have the chance to interact numerous time with the fluctuations leading to the formation of high-energy tail. Furthermore, we showed that the average energy gain for the 10% of the most energetic ions, $\langle \Delta E \rangle_{10\%}$, increases linearly with the ion charge, while it has a weak dependence on the ion mass. Therefore, if ions have larger mass and larger ion charge state they can reach higher energies. These results are in agreement with spacecraft observations showing that, for energies larger than $\sim$ 150 keV, ions are dominantly heavy multiply-charged species, as reported in [26, 27] and [25]. This model describes only a small portion of the possible acceleration mechanisms acting in the magnetotail and we can imagine that a similar stochastic process can jointly work with other mechanisms in a multi-step acceleration process.

About the possible acceleration processes in the terrestrial magnetotail,

we reported high resolution MMS spacecraft measurements of earthward propagating plasma jet fronts as drivers for suprathermal ion acceleration during unsteady magnetic reconnection. The observed magnetic and electric field profiles as well as plasma measurements are consistent with the formation of a magnetic bottle between the two jets.

We suggested that, since the fronts have different propagation speeds, the second jet being faster, the bottle contracts. We found that the ion pitch angle distributions (PADs) depend on the specific energy range, namely lower energies ions $\sim$ 10 keV have PA around 90°, while higher energy ions $\sim$ 100 keV are almost field-aligned. We proposed that thermal ions from the ambient plasma population are initially trapped inside the magnetic bottle, and as the bottle contracts ions are energized along the parallel direction through a first-order Fermi mechanism until they fall into the loss cone. The observed jet fronts are reminiscent of the downward-moving reconnected field lines in collapsing magnetic traps during solar flares, where strong particle acceleration occurs [69]. In contrast to the classical scenario of magnetic traps where mirror points are formed at foot points, our observations suggest that mirror points could be formed closer to the CS possibly due to the interaction of subsequents jets, as also suggested by [88]. Here, we showed for the first time in situ evidence of such mechanism for ions, which are accelerated up to $\sim$ 10 times their thermal energy.

Furthermore, we studyed the acceleration occurring ahead of the first plasma jet front. In the region of the magnetic field depletion, a potential well can form and ions can be stably trapped therein. Since the jet propagates along the x direction, this region can be squeezed and the ion can be accelerated via a resonant surfing mechanism. Ion beams are observed for the different ion species, suggesting that only a portion of the ion population is energized. These beams are observed at different energies for the different ion species, accordingly to the resonance surfing acceleration mechanism which can preferentially energize one species. We qualitatively compare the observations with the numerical models developed by [101, 102, 103].

Both these two ion acceleration mechanism can have far-reaching implications for many astrophysical environments, in particular solar and stellar flares where unsteady reconnection and jet fronts are ubiquitous.

Finally, we studied the cross-scale coupling between fluid turbulence and kinetic processes by using the plasma measurements recorded by the MMS spacecraft during one Kelvin-Helmholtz event at the Earth magnetopause. A heuristic proxy has been used to identify regions of large energy transfer in the time series, where the specific features of the ion velocity distribution functions have been examined. We found that the simplified descriptor used here is able to successfully localize regions of magnetospheric plasma with ion

velocity distribution functions that have more pronounced non-Maxwellian features, corresponding to larger energy transfer. Field-aligned beams at V_A are more likely generated when such energy is predominantly carried by Alfvénic, aligned velocity and magnetic fluctuations, suggesting the possible role of turbulence-driven Landau resonance in the energy dissipation processes.

The presented results suggest a strong connection between the local details of the inertial-range turbulent energy transfer and its transformation through small-scale kinetic processes in non-collisional space plasmas.

Bibliography

[1] V. Petrosian, and W. E. East (2008), Heating and acceleration of intracluster medium electrons by turbulence, *The Astrophysical Journal*, 682:175-185.

[2] V.L. Ginzburg, and S.I. Syrovatsky (1961), Origin of cosmic rays, *Progress of Theoretical Physics Supplement*, 20:1, DOI 10.1143/PTPS.20.1.

[3] M.B. Kallenrode (2003), Current views on impulsive and gradual solar energetic particle events, J*ournal of Physics G: Nuclear and Particle Physics*, 29, 5, 965-981.

[4] Krupp N., *Energetic-particle environments in the solar system*, Heliophysics vol. IV, Chapter 12, Cambridge University Press (2010).

[5] L. A. McFadden, P.R. Weissman, T. V, Johonson, *Encyclopedia of the Solar System*, (Academic Press, MA, 2007).

[6] I. B. Bernstein, J. M. Greene and M. D. Kruskal (1957), Exact Nonlinear Plasma Oscillations, *Phys. Rev.* 108 , 546, doi: 10.1103/PhysRev.108.546.

[7] E. Fermi (1949), An hypothesis on the origin of cosmic radiation, *Nuovo Cimento*, 6 , n.3, Suppl, 317-326.

[8] E. Fermi (1949), On the origin of cosmic radiation, *Phys. Rev.* 75 , 8, doi: 10.1103/PhysRev.75.1169.

[9] P. A. Sturrock (1966), Stochastic Acceleration, *Phys. Rev.*, 141, 186, doi:https://doi.org/10.1103/PhysRev.141.186.

[10] Fisk, L. A. (1971), Solar modulation of galactic cosmic rays, 2, *J. Geophys. Res.*, 76(1), 221–226, doi: 10.1029/JA076i001p00221

[11] Bell, A. R. (1978), The acceleration of cosmic rays in shock fronts. I, *MNRAS*, 182, 147, doi:10.1093/mnras/182.2.147.

[12] Perri, S. and Zimbardo, G., (2015), Short acceleration times from superdiffusive shock acceleration in the heliosphere, *The Astrophysical Journal*, 815:75 (7pp), doi:10.1088/0004-637X/815/1/75.

[13] Retinó, A., Nakamura, R., Vaivads, A. et al., (2008), Cluster observations of energetic electrons and electromagnetic fields within a reconnecting thin current sheet in the Earth's magnetotail, *Journal of Geophysical Research*,10.1029/2008JA013511.

[14] Fu, H. S., Cao, J. B., Khotyaintsev, Y. V. et al., (2013),Dipolarization fronts as a consequence of transient reconnection: In situ evidence, *Geophysical Research Letters*, 40, 6023.

[15] Fu, H. S., Khotyaintsev, Y. V., Vaivads, A. et al., (2013), Energetic electron acceleration by unsteady magnetic reconnection, *Nature Physics*, 9, 426.

[16] C. P. Escoubet, M. Fehringer and M. Goldstein (2001), The Cluster mission, *Ann. Geophys.* 19, 1197–1200, doi:10.5194/angeo-19-1197-2001.

[17] V. Angelopoulos, The THEMIS mission (2009), *Space Science Reviews*, 141, 1-4, 5-34, DOI:10.1007/s11214-008-9336-1.

[18] C.P. Wang, M. Gkioulidou, L. R. Lyons, and V. Angelopoulos (2012), Spatial distributions of the ion to electron temperature ratio in the magnetosheath and plasma sheet, *J. Geophys. Res.*, 117, A08215, doi:10.1029/2012JA017658.

[19] S. Haaland, E. A. Kronberg, P. W. Daly, M. Franz, L. Degener, E. Georgescu, and I. Dandouras (2010), Spectral characteristics of protons in the Earth's plasmasheet: statistical results from Cluster CIS and RAPID, *Ann. Geophys.* 28, 1483–1498, doi:10.5194/angeo-28-1483-2010.

[20] Burton, R. K., McPherron, R. L., and Russell, C. T. (1975), An empirical relationship between interplanetary conditions and Dst, *J. Geophys. Res.*, 80, 4204–4214, https://doi.org/10.1029/JA080i031p04204.

[21] G. Livadiotis, and D.J. McComas (2013), Understanding Kappa Distributions: A Toolbox for Space Science and Astrophysics, *Space Sci Rev.* 175: 183, https://doi.org/10.1007/s11214-013-9982-9.

[22] S. P. Christon, D. J. Williams, D. G. Mitchell, L. A. Frank, and C. Y. Huang (1989), Spectral Characteristics of Plasma Sheet Ion and Electron Populations During Undisturbed Geomagnetic Conditions, *J. Geophys. Res.* 94, 13409–13424.

[23] J. L. Burch, T. E. Moore, R. B. Torbert, B. Giles, L. (2016),Spectral Magnetospheric Multiscale Overview and Science Objectives, *Space Sci Rev.* 199, 1,5–21, doi:10.1007/s11214-015-0164-9.

[24] B. H. Mauk, J. B. Blake, D. N. Baker, J. H. Clemmons, et al., (2016), The Energetic Particle Detector (EPD) Investigation and the Energetic Ion Spectrometer (EIS) for the Magnetospheric Multiscale (MMS) Mission, *Space Sci Rev.* 199, 1,471–514, doi:10.1007/s11214-014-0055-5.

[25] I. J. Cohen, D. G. Mitchell, L. M. Kistler, B. H. Mauk, et al., (2017), Dominance of high-energy (¿ 150 keV) heavy ion intensities in Earth's middle to outer magnetosphere, *J. Geophys. Res. Space Physics*, 122, 9282–9293, doi:10.1002/2017JA024351.

[26] R. C. Allen, S. A. Livi, J. Goldstein (2016), Variations of oxygen charge state abundances in the global magnetosphere, as observed by Polar, *J. Geophys. Res. Space Physics*, 121, 1091–1113,doi:10.1002/2015JA021765.

[27] R. C. Allen, S. A. Livi, S. K. Vines, J. Goldstein (2016), Magnetic latitude dependence of oxygen charge states in the global magnetosphere: Insights into solar wind-originating ion injection, *J. Geophys. Res. Space Physics*, 121, 9888–9912, doi:10.1002/2016JA022925.

[28] F. Catapano, A. V. Artemyev, G. Zimbardo, and I. Y. Vasko (2015), Current sheets with inhomogeneous plasma temperature: Effects of polarization electric field and 2D solutions, *Physics of Plasmas*, 22, 092905 (2015); doi: 10.1063/1.4931736.

[29] E. G. Harris (1962), On a Plasma Sheath Separating Regions of Oppositely Directed Magnetic Field, *Nuovo Cimento*, 23, 1, 115–121.

[30] Yamauchi, M., et al., (2012), EGU (European Geophysical Union) presentation, EGU2012-353.

[31] Eastwood, J. P., M. V. Goldman, H. Hietala, et al., (2015), Ion reflection and acceleration near magnetotail dipolarization fronts associated with magnetic reconnection, *J. Geophys. Res. Space Physics*, 120, 511–525, doi:10.1002/2014JA020516.

[32] M. S. Longair (2011), High Energy Astrophysics, *Cambridge University Press*, ISBN 978-0-521-75618-1.

[33] Voelk, H. J., Morfill, G. E., Forman, M. A. (1981),The effect of losses on acceleration of energetic particles by diffusive scattering through shock waves, *Astrophysical Journal*, doi:10.1086/159272.

[34] S. Perri, G. Zimbardo, and A. Greco, (2011), On the energization of protons interacting with 3-D time-dependent electromagnetic fields in the Earth's magnetotail, *J. Geophys. Res.*, 116, A05221, doi:10.1029/2010JA016328, 2011.

[35] A. V. Artemyev, A. A. Petrukovich, L. M. Zelenyi, R. Nakamura, H. V. Malova, and V. Y. Popov, (2009), Thin embedded current sheets: Cluster observations of ion kinetic structure and analytical models, *Ann. Geophys.*, 27, 4075–4087, www.ann-geophys.net/27/4075/2009/.

[36] P. H. Yoon and A. T. Y. Lui,(2004), Model of ion- or electron- dominated current sheet, *J. Geophys. Res.*, 109, A11, doi:10.1029/2004JA010555.

[37] W. Baumjohann, G. Paschmann, and C. A. Cattel,(1989), Average Plasma Properties in the Central Plasma Sheet, *J. Geophys. Res.*, 94, 6597–6606, doi:10.1029/JA094iA06p06597, 1989.

[38] A. Runov, V. A. Sergeev, R. Nakamura, W. Baumjohann, et al., (2006), Local structure of the magnetotail current sheet: 2001 Cluster observations, *Ann. Geophys.*, 24, 247–262, doi:10.5194/angeo-24-247-2006.

[39] A.V Artemyev, A.A Petrukovich, R. Nakamura, and L. M. Zelenyi, (2011), Cluster statistics of thin current sheets in the Earth magnetotail: Specifics of the dawn flank, proton temperature profiles and electrostatic effects, *J. Geophys. Res.*, 116, A09233, doi:10.1029/2011JA016801.

[40] S. Perri, F. Lepreti, V. Carbone, and A. Vulpiani, (2007), Position and velocity space diffusion of test particles in stochastic electromagnetic fields, *Europhys. Lett.*, 78, 40003, doi:10.1209/0295-5075/78/40003.

[41] J. E. Borovsky, R. C. Elphic, H. O. Funsten, and M. F. Thomsen, (1997), The Earth's plasma sheet as a laboratory for flow turbulence in high-β MHD, *J. Plasma Phys.*, 57, 1–34, 1997.

[42] M. Hoshino, A. Nishida, T. Yamamoto and S. Kokubun (1994), Turbulent magnetic field in the distant magnetotail: Buttom-up process of plasmoid formation?, *Geophys. Res. Lett.*, 21, 2935–2938.

[43] R. Nakamura, W. Baumjohann, C. Mouikis, L.M. Kistler, et al., (2004), Spatial scale of high-speed flows in the plasma sheet observed by Cluster, *Geophys. Res. Lett.*, 31, L09804, doi:10.1029/2004GL019558, 2004.

[44] Z. Vörös,, W. Baumjohann, R. Nakamura, A. Runov, et al., (2007), Spectral scaling in the turbulent Earth's plasma sheet revisited, *Nonlin. Processes Geophys.*, 14, 535–541, doi:10.5194/npg-14-535-2007.

[45] A. Greco, S. Perri, and G. Zimbardo (2010), Stochastic Fermi acceleration in the magnetotail current sheet: a numerical study, *J. Geophys. Res.*, 115, A02203, doi:10.1029/2009JA014690.

[46] V. Sergeev, A. Runov, W. Baumjohann, R. Nakamura, T. et al., (2003), Current sheet flapping motion and structure observed by Cluster, *Geophys. Res. Lett.*, 30, 1327.

[47] S. Perri, A. Greco, and G. Zimbardo, (2009), Stochastic and direct acceleration mechanisms in the Earth's magnetotail, *Geophys. Res. Lett.*, 36, L04103, doi:10.1029/2008GL036619.

[48] Dobrowolny, M. (1968), Instability of a neutral sheet, *Il Nuovo Cimento*, B Series, 55(2), 427-442.

[49] Kronberg, E. A., Ashour-Abdalla, M., Dandouras, I., Delcourt, D. C., et al., (2014), Circulation of heavy ions and their dynamical effects in the magnetosphere: Recent observations and models, *GSpace Science Reviews*, 184, 173-235. https://doi.org/10.1007/s11214-014-0104-0.

[50] Catapano, F., Zimbardo, G., Perri, S., Greco, A., and Artemyev, A. V. (2016), Proton and heavy ion acceleration by stochastic fluctuations in the Earth's magnetotail, *Ann. Geophys.*, 34, 917–926. https://doi.org/10.5194/angeo-34-917-2016.

[51] Seki, K., Hirahara, M., Hoshino, M., Terasawa, T., et al., (2003), Cold ions in the hot plasma sheet of Earth's magnetotail, *Nature*, 422, 589-592.

[52] Hoshino, M., Nishida, A., Yamamoto T., and Kokubun, S., (1994), Turbulent magnetic field in the distant magnetotail: Buttom-up process of plasmoid formation?, *Geophys. Res. Lett.*, 21, 2935–2938.

[53] Greco, A., Artemyev, A., and Zimbardo, G. (2015), Heavy ion acceleration at dipolarization fronts in planetary magnetotails, *Geophysical Research Letters*, 42, 8280-8287. https://doi.org/10.1002/2015GL066167.

[54] Zelenyi, L. M., Dolgonosov, M. S., Grigorenko, E. E., and Sauvaud, J.A. (2007), Universal properties of the nonadiabatic acceleration of ions in current sheets, *JETP Letters*, 85, 187-193. https://doi.org/10.1134/S0021364007040017.

[55] Büchner, J., and L. M. Zelenyi (1989), Regular and chaotic charged particle motion in magnetotaillike field reversals: 1. Basic theory of trapped motion, J. *Geophys. Res.*, 94(A9), 11821–11842, doi: 10.1029/JA094iA09p11821.

[56] Artemyev, A. V., Petrukovich, A. A., Zelenyi, L. M., et al., (2008), Comparison of multi-point measurements of current sheet structure and analytical models, *Ann. Geophys.*, 26, 2749-2758, https://doi.org/10.5194/angeo-26-2749-2008.

[57] Torbert, R.B., Russell, C.T., Magnes, W. et al, (2016), The FIELDS Instrument Suite on MMS: Scientific Objectives, Measurements, and Data Products, *Space Sci Rev*, 199: 105, https://doi.org/10.1007/s11214-014-0109-8.

[58] Russell, C.T., Anderson, B.J., Baumjohann, W. et al., (2016), The Magnetospheric Multiscale Magnetometers, *Space Sci Rev*, 199: 189, https://doi.org/10.1007/s11214-014-0057-3.

[59] Lindqvist, PA., Olsson, G., Torbert, R.B. et al.,(2016), The Spin-Plane Double Probe Electric Field Instrument for MMS, *Space Sci Rev*, 199: 137, https://doi.org/10.1007/s11214-014-0116-9.

[60] Ergun, R.E., Tucker, S., Westfall, J. et al., (2016), The Axial Double Probe and Fields Signal Processing for the MMS Mission, *Space Sci Rev*, 199: 167, https://doi.org/10.1007/s11214-014-0115-x.

[61] Pollock, C., Moore, T., Jacques, A. et al., (2016), Fast Plasma Investigation for Magnetospheric Multiscale, *Space Sci Rev*, 199: 331, https://doi.org/10.1007/s11214-016-0245-4.

[62] Priest, E. and Forbes, T., (2000), Magnetic reconnection : MHD theory and applications, *New York : Cambridge University Press*.

[63] Alfvén, H., (1942), Existence of Electromagnetic-Hydrodynamic Waves, *Nature*, 150, pages 405-406, https://doi.org/10.1038/150405d0.

[64] Zweibel, E. G., (2009), Magnetic Reconnection in Astrophysical and Laboratory Plasmas,*Annual Review of Astronomy and Astrophysics*, 47: 291-332, doi: 10.1146/annurevastro-082708-101726.

[65] Pritchett, P. L., (2006), Relativistic electron production during guide field magnetic reconnection, *Journal of Geophysical Research*, Space Physics 111, 10.1029/2006JA011793.

[66] Ashour-Abdalla,M., El-Alaoui, M., Goldstein, M. L. et al., (2011), Observations and simulations of non-local acceleration of electrons in magnetotail magnetic reconnection events, *Nature Physics*, 10.1038/nphys1903.

[67] Birn, J., Artemyev, A. V., Baker, D. N. et al., (2012), Particle Acceleration in the Magnetotail and Aurora, *Space Science Reviews*, 173, 49.

[68] Emslie, A. G., et al. (2004), Energy partition in two solar flare/CME events, *J. Geophys. Res.*, 109, A10104, doi:10.1029/2004JA010571.

[69] Somov, B.V. and T. Kosugi, (1997),Flares in accretion disk coronae, *Astrophys. J.*, 485, 859.

[70] Giuliani, P. and Neukirch, T. and Wood, P., (2005), Particle motion in collapsing magnetic traps in solar flares. I. Kinematic theory of collapsing magnetic traps, *The Astrophysical Journal*, 635, 636.

[71] Zharkova,V. V., K. Arzner, A. O. Benz, et al., (2011), Recent advances in understanding particle acceleration processes in solar flares, *Space Science Reviews*, 159, 357.

[72] Somov, B. V. , (2013), "Collapsing magnetic traps in solar flares," in Plasma Astrophysics, Part II: Reconnection and Flares (Springer New York, New York, NY, 2013) pp. 213–274.

[73] Birn,J., M. Battaglia, L. Fletcher, et al., (2017), Can Substorm Particle Acceleration Be Applied to Solar Flares?, *The Astrophysical Journal*, 848, 116.

[74] Runov, A., V. Angelopoulos, M. I. Sitnov, et al.,(2009), THEMIS observations of an earthward-propagating dipolarization front, *Geophys. Res. Lett.*, 36, L14106, doi:10.1029/2009GL038980.

[75] Angelopoulos, V. (2008), The THEMIS mission, *Space Science Reviews*, 10.1007/s11214-008-9336-1.

[76] Sitnov, M. I., M. Swisdak, and A. V. Divin (2009), Dipolarization fronts as a signature of transient reconnection in the magnetotail, *J. Geophys. Res.*, 114, A04202, doi:10.1029/2008JA013980.

[77] Sergeev, V., V. Angelopoulos, S. Apatenkov, et al., (2009), Kinetic structure of the sharp injection/dipolarization front in the flow-braking region, *Geophys. Res. Lett.*, 36, L21105, doi:10.1029/2009GL040658.

[78] Zhou, X.Z., V. Angelopoulos, V. A. Sergeev, and A. Runov (2010),Accelerated ions ahead of earthward propagating dipolarization fronts, *J. Geophys. Res.*, 115, A00I03, doi:10.1029/2010JA015481.

[79] Wu, P., and M. A. Shay (2012), Magnetotail dipolarization front and associated ion reflection: Particle-in-cell simulations, *Geophys. Res. Lett.*, 39, L08107, doi:10.1029/2012GL051486.

[80] Birn, J., A. Runov, and M. Hesse (2015), Energetic ions in dipolarization events, *J. Geophys. Res. Space Physics*, 120, 7698–7717, doi:10.1002/2015JA021372.

[81] Greco, A., A. Artemyev, and G. Zimbardo (2015), Heavy ion acceleration at dipolarization fronts in planetary magnetotails, *Geophys. Res. Lett.*, 42, 8280–8287, doi:10.1002/2015GL066167.

[82] Catapano, F., Zimbardo, G., Perri, S.,et al., (2017), Charge Proportional and Weakly Mass-Dependent Acceleration of Different Ion Species in the Earth's Magnetotail, *Geophysical Research Letters*, 44, https://doi.org/10.1002/2017GL075092

[83] Tsyganenko, N. A. (1987), Determination of the Magnetospheric Current System Parameters and Development of Experimental Geomagnetic Field Models Based on Data from IMP and HEOS Satellites, *Planet. Space Sci.*, 35, 1347-1358.

[84] Runov, A., V. Angelopoulos, X.Z. Zhou, et al., (2011), A THEMIS multicase study of dipolarization fronts in the magnetotail plasma sheet, *J. Geophys. Res.*, 116, A05216, doi:10.1029/2010JA016316.

[85] Zhou, M., M. Ashour-Abdalla, X. Deng, et al., (2009), THEMIS observation of multiple dipolarization fronts and associated wave characteristics in the near-Earth magnetotail, *Geophys. Res. Lett.*, 36, L20107, doi:10.1029/2009GL040663.

[86] Ge, Y. S., J. Raeder, V. Angelopoulos, et al., (2011), Interaction of dipolarization fronts within multiple bursty bulk flows in global MHD simulations of a substorm on 27 February 2009, *J. Geophys. Res.*, 116, A00I23, doi:10.1029/2010JA015758.

[87] Paschmann, G. and Daly, P. W., (1998), Analysis methods for multispacecraft data, Vol. 1, *ISSI Scientific Report*.

[88] Borissov A., Neukirch T., and Threlfall J., (2016), Particle Acceleration in Collapsing Magnetic Traps with a Braking Plasma Jet,*Solar Physics*, 291, 1385.

[89] Drake J.F., M. Swisdak, H. Che, and M. A. Shay, (2006), Electron acceleration from contracting magnetic islands during reconnection, *Nature*, 443-5, doi:10.1038/nature05116

[90] Runov, A., A.V. Sergeev, R. Nakamura, et al., (2006), Local structure of the magnetotail current sheet: 2001 Cluster observations, *Annales Geophysicae*, 24, 247-262, SRef-ID: 1432-0576/ag/2006-24-247.

[91] Zhao, D., et al., (2016), Electromagnetic disturbances observed near the dip region ahead of dipolarization front, *Geophys. Res. Lett.*, 43, 3026–3034, doi:10.1002/2016GL068033.

[92] Khotyaintsev,Yu. V., Cully, C. M., Vaivads, A., et al., (2011), Plasma Jet Braking: Energy Dissipation and Nonadiabatic Electrons, *Physical Review Letters*, 106, 165001, doi: 10.1103/PhysRevLett.106.165001.

[93] Li, S., V. Angelopoulos, A. Runov, et al., (2011), On the force balance around dipolarization fronts within bursty bulk flows, *Journal of Geophysical Research: Space Physics*, 116 (A5), doi:10.1029/2010JA015884.

[94] Xing, X., L. R. Lyons, X. Zhou, et al., (2012), On the formation of pre-onset azimuthal pressure gradient in the near-Earth plasma sheet, *Journal of Geophysical Research: Space Physics*, 117 (A8), doi:10.1029/2012JA017840.

[95] Liu, J., V. Angelopoulos, X. Zhou, et al., (2013), On the role of pressure and flow perturbations around dipolarizing flux bundles, *Journal of Geophysical Research: Space Physics*, 118 (11), 7104–7118, doi:10.1002/2013JA019256.

[96] Zhou, X., V. Angelopoulos, J. Liu, et al., (2014), On the origin of pressure and magnetic perturbations ahead of dipolarization fronts, *Journal of Geophysical Research: Space Physics*, 119 (1), 211-220, doi:10.1002/2013JA019394.

[97] Drake, J., M. Swisdak, P. Cassak, and T. Phan (2014), On the 3-D structure and dissipation of reconnection-driven flow bursts, *Geophysical Research Letters*, 41 (11), 3710-3716, doi:10.1002/2014GL060249.

[98] Catapano, F., Retinò, A., Zimbardo, G., et al., (2018), submitted to *Physical Review Letters*.

[99] Greco, A., A. Artemyev, and G. Zimbardo (2014), Proton acceleration at two-dimensional dipolarization fronts in the magnetotail,*Journal of Geophysical Research: Space Physics*, 119 (11), 8929-8941, doi:10.1002/2014JA020421.

[100] Artemyev, A. V., G. Zimbardo, A. Y. Ukhorskiy, and M. Fujimoto (2014), Preferential acceleration of heavy ions in the reconnection outflow region Drift and surfatron ion acceleration, *Astronomy and Astrophysics*, 562, A58, doi:10.1051/0004-6361/201322462.

[101] Artemyev, A. V., V. N. Lutsenko, and A. A. Petrukovich (2012), Ion resonance acceleration by dipolarization fronts: analytic theory and spacecraft observation, *Annales Geophysicae*, 30 (2), 317–324, doi:10.5194/angeo-30-317-2012.

[102] Ukhorskiy, A. Y., M. I. Sitnov, V. G. Merkin, and A. V. Artemyev (2013), Rapid acceleration of protons upstream of earthward propagating dipolarization fronts, *Journal of Geophysical Research: Space Physics*, 118 (8), 4952–4962, doi:10.1002/jgra.50452.

[103] Ukhorskiy, A. Y., M. I. Sitnov, V. G. Merkin, et al., (2017), Ion acceleration at dipolarization fronts in the inner magnetosphere, *Journal of Geophysical Research: Space Physics*, 122 (3), 3040-3054, doi:10.1002/2016JA023304.

[104] Zhou, X., V. Angelopoulos, V. A. Sergeev, and A. Runov (2011), On the nature of precursor flows upstream of advancing dipolarization fronts, *Journal of Geophysical Research: Space Physics*, 116 (A3), doi:10.1029/2010JA016165.

[105] Zhou, X., D. Pan, V. Angelopoulos, et al., (2015), Ion acceleration and reflection on magnetotail antidipolarization fronts, *Geophysical Research Letters*, 42 (21), 9166–9175, doi:10.1002/2015GL065865.

[106] Pan, D., X. Zhou, Q. Shi,et al., (2015),On the generation of magnetic dips ahead of advancing dipolarization fronts, *Geophysical Research Letters*, 42 (11), 4256–4262, doi:10.1002/2015GL064369.

[107] Katsouleas, T., and J. M. Dawson (1983), Unlimited electron acceleration in laser-driven plasma waves, *Phys. Rev. Lett.*, 51, 392–395, doi:10.1103/PhysRevLett.51.392.

[108] Hoshino, M. (2005), Electron surfing acceleration in magnetic reconnection, *Journal of Geophysical Research: Space Physics*, 110 (A10), doi:10.1029/2005JA011229.

[109] Neishtadt, A. I., A. V. Artemyev, L. M. Zelenyi, and D. L. Vainshtein (2009), *JETP Letters*, 89 (9), 441–447, doi:10.1134/S0021364009090045.

[110] Angelopoulos, V., T. D. Phan, D. E. Larson, et al., (1997), Magnetotail flow bursts: Association to global magnetospheric circulation, relationship to ionospheric activity and direct evidence for localization, *Geophysical Research Letters*, 24 (18), 2271–2274, doi:10.1029/97GL02355.

[111] Nakamura, R., W. Baumjohann, C. Mouikis, et al., (2004), Spatial scale of high-speed flows in the plasma sheet observed by Cluster, *Geophysical Research Letters*, 31 (9), doi:10.1029/2004GL019558.

[112] Parker, E.N., (1958), Dynamics of the interplanetary gas and magnetic field, *Astrophysical Journal*, 128:664–676, doi:10.1086/146579.

[113] Dungey, J. W., (1961), The interplanetary magnetic field and the auroral zones, *Physical Review Letters*, 6(2):47-48, doi:10.1103/PhysRevLett.6.47.

[114] Cushman-Roisin,B., and Beckers, J., (2009), Introduction to Geophysical Fluid Dynamics - Physical and Numerical Aspects, *Academic Press*, 393-401.

[115] Hasegawa, H., M. Fujimoto, T.-D. Phan, et al., (2004), Transport of solar wind into Earth's magnetosphere through rolled-up Kelvin-Helmholtz vortices, *Nature*, 430, 755–758, doi:10.1038/nature02799.

[116] Delamere, P. A., R. J. Wilson, S. Eriksson, and F. Bagenal, (2013), Magnetic signatures of Kelvin-Helmholtz vortices on Saturn's magnetopause: Global survey, *J. Geophys. Res. Space Physics*, 118, 393–404, doi:10.1029/2012JA018197.

[117] Karimabadi, H., et al. (2014), The link between shocks, turbulence, and magnetic reconnection in collisionless plasmas, *Phys. Plasmas*, 21(6), 62308, doi:10.1063/1.4882875.

[118] Nykyri, K., and A. Otto, (2001), Plasma transport at the magnetospheric boundary due to reconnection in Kelvin-Helmholtz vortices, *Geophys. Res. Lett.*, 28, 3565–3568, doi:10.1029/2001GL013239.

[119] Rossi, C., F. Califano, A. Retinó, et al.,(2015), Two-fluid numerical simulations of turbulence inside Kelvin-Helmholtz vortices: Intermittency and reconnecting current sheets, *Phys. Plasmas*, 22(12), 122303, doi:10.1063/1.4936795.

[120] Servidio, S., W. H. Matthaeus, M. A. Shay, et al., (2010), Statistics of magnetic reconnection in two-dimensional magnetohydrodynamic turbulence, *Phys. Plasmas*, 17(3), 32315, doi:10.1063/1.3368798.

[121] Stawarz, J. E., et al. (2016), Observations of turbulence in a Kelvin-Helmholtz event on 8 September 2015 by the Magnetospheric Multiscale mission, *J. Geophys. Res. Space Physics*, 121, 11,021–11,034, doi:10.1002/2016JA023458.

[122] Elsasser, W. M., (1950), The Hydromagnetic Equations, *Phys. Rev.*, 79, 183, doi:10.1103/PhysRev.79.183.

[123] Richardson, L.F. (1922), Weather prediction by numerical process, *Cambridge University Press*, OCLC 3494280.

[124] Politano, H., and Pouquet, A., (1998), Dynamic length scales for turbulent magnetized flows, *Geophys. Res. Lett.* 25, 273–6.

[125] Sorriso-Valvo, L., Carbone, V., Noullez, et al., (2002), Analysis of cancellation in two-dimensional magnetohydrodynamic turbulence, *Phys. Plasmas*, 9, 89, doi: 10.1063/1.1420738.

[126] Sorriso-Valvo, L., Marino, R., Lijoi, L., et al., (2015), Self-consistent Castaing Distribution of Solar Wind Turbulent Fluctuations, *The Astrophysical Journal*, 807, 1, 86, http://stacks.iop.org/0004-637X/807/i=1/a=86.

[127] Sorriso-Valvo, L., Carbone, V., Perri, S., et al., (2018),On the Statistical Properties of Turbulent Energy Transfer Rate in the Inner Heliosphere, *Solar Physics*, 293, DOI: 10.1007/s11207-017-1229-6.

[128] Eriksson, S., Lavraud, B., Wilder, F.D., et al., (2016), Magnetospheric Multiscale observations of magnetic reconnection associated with Kelvin-Helmholtz waves, *Geophys. Res. Lett.*, 43, 5606–5615, doi:10.1002/2016GL068783.

[129] Greco, A., W. H. Matthaeus, S. Servidio, and P. Dmitruk, (2009), Waiting-time distributions of magnetic discontinuities: Clustering or Poisson process?, *Phys. Rev. E*, 80, 046401, https://doi.org/10.1103/PhysRevE.80.046401.

[130] Camporeale, E., L. Sorriso-Valvo, F. Califano, and A. Retinó, (2018), Coherent Structures and Spectral Energy Transfer in Turbulent Plasma: A Space-Filter Approach, *Phys. Rev. Lett.*, 120, 125101, https://doi.org/10.1103/PhysRevLett.120.125101.

[131] Valentini, F., and P., Veltri, (2009), Electrostatic Short-Scale Termination of Solar-Wind Turbulence, *Phys. Rev. Lett.*, 102, 225001, DOI:10.1103/PhysRevLett.102.225001.

[132] Valentini, F., D., Perrone, P., Veltri, (2011), Short-wavelength Electrostatic Fluctuations in the Solar Wind, *Astrophys. J.*, 739, 54, http://stacks.iop.org/0004-637X/739/i=1/a=54.

[133] Wilder, F. D., R. E., Ergun, S. J., Schwartz, et al., (2016), Observations of large-amplitude, parallel, electrostatic waves associated with the Kelvin-Helmholtz instability by the magnetospheric multiscale mission, *Geophys. Res. Lett.*, 43, 8859, https://doi.org/10.1002/2016GL070404.

[134] Kennel, C. F., and Engelmann, F., (1966), Velocity Space Diffusion from Weak Plasma Turbulence in a Magnetic Field, *Phys. Fluids*, 9, 2377,https://doi.org/10.1063/1.1761629.

[135] Valentini, F., P. Veltri, F. Califano, A. Mangeney, (2008), Cross-Scale Effects in Solar-Wind Turbulence, *Phys. Rev. Lett.*, 101, 025006, DOI:https://doi.org/10.1103/PhysRevLett.101.025006.

[136] Perrone D., Passot T., Laveder D., et al., (2018), Fluid simulations of plasma turbulence at ion scales: Comparison with Vlasov-Maxwell simulations,, *Physics of Plasmas*, 25, 052302, DOI:10.1063/1.5026656.

[137] Donoho D.L., (2006), Compressed sensing, *IEEE Transactions on Information Theory*, 52, 4, 1289-1306, doi: 10.1109/TIT.2006.871582.

[138] Candès, E. J., Romberg, J. K. and Tao, T. (2006), Stable signal recovery from incomplete and inaccurate measurements, *Comm. Pure Appl. Math.*, 59: 1207-1223. doi:10.1002/cpa.20124.

[139] Gallana, L., F. Fraternale, M. Iovieno, et al., (2016), Voyager 2 solar plasma and magnetic field spectral analysis for intermediate data sparsity, *J. Geophys. Res. Space Physics*, 121, 3905-3919, doi:10.1002/2015JA021830.

[140] Fraternale,F., N. V. Pogorelov, J. D. Richardson, and D. Tordella, submitted to *J. Geophys. Res.*, (2018).

[141] Hadid, L. Z. and Sahraoui, F. and Galtier, S. and Huang, S. Y (2018), Compressible Magnetohydrodynamic Turbulence in the Earth's Magnetosheath: Estimation of the Energy Cascade Rate Using in situ Spacecraft Data, *Phys. Rev. Lett.*, 120, 5, 055102, doi:10.1103/PhysRevLett.120.055102.

[142] Grinsted, A., Moore, J. C., and Jevrejeva, S. (2004), Application of the cross wavelet transform and wavelet coherence to geophysical time series, *Nonlin. Processes Geophys.*, 11, 561-566, https://doi.org/10.5194/npg-11-561-2004, 2004.

[143] Lion, S.and Alexandrova, O., and Zaslavsky, A. (2016), Coherent Events and Spectral Shape at Ion Kinetic Scales in the Fast Solar Wind Turbulence, *The Astrop. Jour.*, 824,1, 47, http://stacks.iop.org/0004-637X/824/i=1/a=47.

[144] Farge, M. (1992), Wavelet transforms and their applications to turbulence, *Annu. Rev. Fluid Mech.*, 24, 395.

[145] Torrence, C. and Compo, G. P., (1998), A pratical guide to wavelet analysis, *BAMS*, 79, 61

[146] Perrone D., and O. Alexandrova, and O. W. Roberts, et al., (2017), Coherent Structures at Ion Scales in Fast Solar Wind: Cluster Observations, *The Astrophysical Journal*, 849, 1, 49, http://stacks.iop.org/0004-637X/849/i=1/a=49.

[147] Sorriso-Valvo, L., Catapano, F., Retinò, A., et al., (2018), submitted to *Physical Review Letters*.

Acknowledgements

First of all, I would like to thank my supervisors Gaetano Zimbardo, Alessandro Retinò, and Dominique Delcourt for their guidance and support and patience. I learned from them a lot both from a human and scientific point of view.

I am grateful to Silvia Perri, Antonella Greco, Luca Sorriso-Valvo, Leonardo Primavera, and all the plasma team at the Universty of Calabria for the useful and interesting discussions and improvements on this thesis. Also, I would like to thank Giulia Cozzani, Alexandra Alexandrova, Olivier Le Contel, Hugo Breuillard and all the LPP team, for their active collaboration and for welcoming me in Paris. Special thanks go to Giulia Cozzani, Sae Aizawa, Alexandra Alexandrova, Roberto Manuzzo, Oreste Pezzi, Alexa Guglielmelli, Jacopo Settino, and many others for their friendship, for the nice time together and good wines.

I must thank my family and my sisters for their support and love. Also, thank to my second family, for their welcome, affection, and happiness.

Finally, I would like to thank Sonse, for being always by my side.